# THIN FILM STUDY OF TOPOLOGICAL MATERIALS VIA ATOMIC SCALE ENGINEERING

By

JISOO MOON

A dissertation submitted to the

School of Graduate Studies

Rutgers, the State University of New Jersey

In partial fulfillment of the requirements

For the degree of

Doctor of Philosophy

Graduate Program in Physics and Astronomy

Written under the direction of

Seongshik Oh

And approved by

_____

_____

_____

_____

_____

New Brunswick, New Jersey

May, 2019

# ABSTRACT OF THE DISSERTATION

# THIN FILM STUDY OF TOPOLOGICAL MATERIALS VIA ATOMIC SCALE ENGINEERING

By JISOO MOON

Dissertation Director: Seongshik Oh

This dissertation seeks to deepen our understanding of the novel physical properties in a class of topological materials named topological insulators (TIs). In particular, electrical transport properties in $Bi_2Se_3$ TI thin films grown by the molecular beam epitaxy (MBE) technique are mainly investigated through an experimental standpoint. It first begins by reviewing the topological phases from the quantum Hall effect (QHE) to the TIs in a conceptual point of view, which will lead to what the TIs are. This is followed by a comprehensive introduction to the thin film growth using the MBE as atomically precise technique in consideration of atomic scale engineering for various defects. This is then follow by an approach to discern unknown physical properties via electrical transport measurements, which is the main experimental technique used in this work. Throughout the following chapters these techniques are applied to manipulate the topological properties of the TIs and explained in details.

For the experimental results, we first discuss the hole doping problem in $Bi_2Se_3$ thin films and its solution. This study shows that the main culprit resides in the high density of interfacial defects on the substrates, and how a solution is achieved by a properly designed buffer layer engineering. Subsequently, we show the method of implementing the ferromagnetic (FM) anomalous Hall effect (AHE) to the $Bi_2Se_3$ thin films. While the Cr-doped $Bi_2Se_3$, among the three dimensional TI families, was predicted to be the most promising candidate to exhibit the quantum

anomalous Hall effect (QAHE), the observation was quite the contrary. It has failed to exhibit even the FM AHE, which is an expected predecessor to the QAHE in comparison to the Cr- or V-doped $(Sb,Bi)_2Te_3$ showing the quantum anomalous Hall effect (QAHE) and V-doped $Bi_2Se_3$ exhibiting the AHE. In great succession via utilizing a surface state engineering scheme, we show the achievement of the FM AHE in Cr-doped $Bi_2Se_3$ thin films, and consequently emerging positive anomalous Hall conductivity. We explain the sign problem by analyzing the mass-gap susceptibility based on a tight binding model and first-principles study.

# Acknowledgements

My life as a graduate student could be described as a series of challenges. Looking back, however, whenever I ran against a stump, there was always people who have magically replaced it with something wonderful and helped me navigate out of it. These people are my family, fellow students, postdocs and professors, with whom, I was able to overcome the inevitable adversities and move forward with a positive energy.

First and foremost, I would like to thank my academic advisor Professor Seongshik Oh for his friendly leadership, limitless patience and considerate support. He has always respected and trusted his students and postdocs, and credited them in every work. Throughout my Ph.D. years, his dedication and commitment to his students has been an inspiration to everyone around him.

I would like to thank my committee members; Professors Piers Coleman, Mark Croft, Eric Gawiser, and Martha Greenblatt for their time and insight, both of which I have immensely benefited from.

I would like to specifically thank Professor Weida Wu for helpful discussions and advices given throughout various scientific collaboration, which has deepened my understanding of the fundamental physics of topological insulators as well as scientific instruments. I would also like to express my gratitude to Professor David Vanderbilt for in-depth discussions and collaborations that further deepened my understanding of topological materials itself as well as the concept behind it.

I would like to thank my current lab mates Deepti Jain, Gaurab Rimal and Xiong (Simon) Yao for creating a fun ambiance and being flexible with scheduling growth and measurement times. I would also like to thank Maryam Salehi with whom the trips to the NHMFL were rewarding. I am thankful to Kathy for insightful discussions on machining and lending a helpful hand in the lab. I would also like to thank my former lab mates and friends, Nikesh Koirala and Matthew J. Brahlek, with whom my early years of graduate school were joyful. I also want to thank my former lab mates Bharath Kannan, Asad Asif and Namrata Bansal.

I would like thank to my former roommate and friend Juho Lee with whom I have had numerous precious memories in my Ph.D. years at Rutgers as well as Johnson, Parktowne and Orchard Gardens apartments. I also want to thank my friends Drs. Eunkyung Lee and Haewon Yoon, whose kindness and friendship have always been a joy.

I would like to thank my long-time friends Drs. Seyoung Park and Doohee Cho, whose discussions and advices were always worthwhile. I would also like to thank Drs. Jaewook Kim and Jinwoong Kim for helpful collaborations and discussions, which have deepened my understanding in physics. I also want to remember my friends Drs. Heetaek Yi, Hyun-Ho Choi, Seongjoon Lim, Heung-sik Kim, Sungkyun Choi, Min Gyu Kim, Changjong Kang and Minjae Kim.

I would like to thank Jerrell Spotwood for his kindness and deft handling of documents, through which, my research progress has been accelerated. I would also like to thank Bill Schneider and Eric Paduch from the machine shop for their kindness and guidance, which have made all my research eventually possible.

I would like to thank Natasha Meek et al., all the group fitness instructors, whose energetic group fitness classes have created unforgettable memories and kept me healthy both physically and mentally.

Last but not least, I am deeply indebted to my family for their continuous and unparalleled love. I want to especially thank my beautiful wife Joanna for her support, wisdom and love, with which I have been able to complete my Ph.D. program. To my parents and sister, whose limitless encouragement have filled me with positive energy and made me who I am at this point. To my parents-in-law for their unfailing support. Lastly, to my little princess Mayrin, who gives me unending joy.

This dissertation covers works published or pending publication. The work in CHAPTER 4 was published [Moon *et al.*, *Nano Letters*, **18**(2), 820–826, 2018]. CHAPTER 5 is a work pending publication that has been done in intimate collaboration with Dr. Jinwoong Kim and Professor David Vanderbilt.

# Dedication

*Thanks to the boundless encouragement from my Dad, Mom and Sister, and especially my wife Joanna and my adorable daughter Mayrin, with whom I have been able to persevere until now. Therefore, this work is wholly dedicated to my family.*

# TABLE OF CONTENTS

# LIST OF TABLES

# LIST OF FIGURES

# CHAPTER 1. PROLOGUE: Introduction to topological insulators

The core of condensed matter physics is concerned with understanding the collective behavior of particles in solids. The nascent study of condensed matter physics dates back to the early 1900s when the electron theory in metals was established by Paul Drude. The idea of a free electron "gas" in periodic arrays of atoms proposed by P. Drude was the first collective consideration of electrons in macroscopic solids. ([1]Drude, 1900) Since then, research in condensed matter physics has been boosted with the development of quantum mechanics. The impact of quantum theory in solids is indeed astonishing. The adoption of quantum mechanical concepts in solids has helped develop capabilities of analyzing a variety of phenomena in materials such as classification of insulators, semiconductors, conductors, magnetism, superconductivity, and the quantum Hall effect. Above all, the advancement of the physics of semiconductors, in particular, is intimately related to the forefront of material research today. The fundamental properties of semiconductor materials can be explained by the concept of electronic energy band structure, which is underpinned by quantum mechanics. The special class of materials which this work mainly deals with is deeply associated with electronic energy band structure, and the physics behind the materials will be described using quantum mechanical concepts.

This chapter will lead into a special class of materials, called *topological insulators* (TIs) ([2]Moore and Balents, 2007), starting from fundamental band theory. TIs, as the name indicates, are insulating materials, but have novel properties originating from their special characters, so-called topology. We will review the fundamental and special properties of TIs using quantum theories in solids, which will be followed by experimental realizations of TIs, and their potential applications. Lastly, we will briefly outline the contents and the target of this work.

## 1.1 From band to quantum Hall insulators

The Nobel prize in physics 2016 was awarded to David J. Thouless (one half), F. Duncan M. Haldane and J. Michael Kosterlitz (the other half jointly) for theoretical discoveries of topological phase transitions and topological phases of matter. The Laureates have adopted an advanced mathematical concept, *topology*, to explain exotic quantum phenomena, especially in low dimensions at low temperature. The term "topology" originates from mathematics or even more fundamental consideration about properties of geometric forms that remain invariant under continuous deformation.

It had been believed that any order cannot remain in two dimensions (2D) with thermal fluctuation, even at absolute zero temperature. To be more specific, people had thought that the exotic phases such as superfluid, superconductor, or ordered magnetism cannot exist in 2D. However, D. Thouless and M. Kosterlitz challenged that, and successfully explained the phase transitions using vortex–antivortex pairs, the so-called KT (Kosterlitz–Thouless) transition. They were able to explain why superfluidity and superconductivity occur at low temperature and vanish above a critical temperature with the vortex pair formation at low temperature. It turns out that the transitions were not only quantum mechanical but also topological, and different from the usual phase transition such as the ice–water transition. Moreover, their explanation was universally applicable to other materials.

At the beginning of the 1980s, Klaus von Klitzing, Nobel prizewinner in physics 1985, and his colleagues observed stepwise Hall conductance with surprising accuracy in a 2D electron gas (2DEG). D. Thouless *et al*. showed that the discreteness of the Hall conductance originates from the topological nature. On the other hand, D. Haldane predicted new material classes using topological concepts in 2D small magnet chains ([3]Haldane, 1988).

Band theory is a good starting point for the topological phase of matter because we can easily imagine winding energy bands.

### 1.1.1 Band theory

Quantum mechanics (QM) tells us that the energy levels are allowed in a discrete fashion in the microscopic world. When a negatively charged particle is moving around a fixed and positively charged point, the energy of the particle is allowed to have only specific values. For example, the (nonrelativistic) energy levels of the hydrogen atom are $-\frac{1}{n^2}\text{Ry} = -\frac{13.6}{n^2}\text{eV}$, where $n$ is a positive integer. If there are two hydrogen atoms, and they are close enough to each other, the energy levels are not the same as those of the individual atoms. The previous energy levels split into two different levels, forming bonding (lower energy) and antibonding (higher energy) states. In a similar way, when there are three or four atoms, the energies form multiple levels as shown in Figure 1-1. In a crystal, there are numerous, almost infinite number of atoms periodically, then all the ground states of each atom establish a certain, approximately continuous, range of allowed energies, called an "energy band."

Let us imagine electrons are independently moving in free space. In classical mechanics, the moving particles have kinetic energy, $\frac{p^2}{2m}$, where $p$ is the momentum and $m$ is the mass of the particle. The energy is a quadratic function of momentum, therefore, the relation is parabolic as shown in Figure 1-2(a). Considering an electron's wave properties, the momentum can be expressed using $k$, the wave number, where $p = \hbar k$ ($\hbar$ is the reduced Planck constant, $\frac{h}{2\pi}$). The energy can be any positive value because the momentum is a continuous observable in the classical regime. However, if we assume periodicity in free space, the energy–momentum relation is modified. When the electrons are going through a weak periodic potential such as a one-dimensional (1D) lattice as shown in Figure 1-2(b), they become "nearly free electrons," not completely free electrons. The energy structure, energy vs momentum, is defined in the reciprocal space ($k$-space) based on the translational invariance and also becomes periodic. The $\boldsymbol{k}$ is called crystal momentum to differentiate it from the regular classical momentum $\boldsymbol{p}$. The smallest Bravais

lattice in the *k*-space is called the first Brillouin zone (BZ) as indicated in the black box in Figure 1-2(b). Because of the periodicity, the electrons undergo Bragg reflection, which is described by the Bloch wave function, and a gap opens near the zone corner (or boundary). None of the electrons can exist inside the gap because it is not quantum mechanically allowed. In this way, two different kinds of energy bands are formed, and the relation between the energy and crystal momentum with the energy bands is called energy band structure. The development of the electronic energy band theory in solids is one of the big successes of QM.

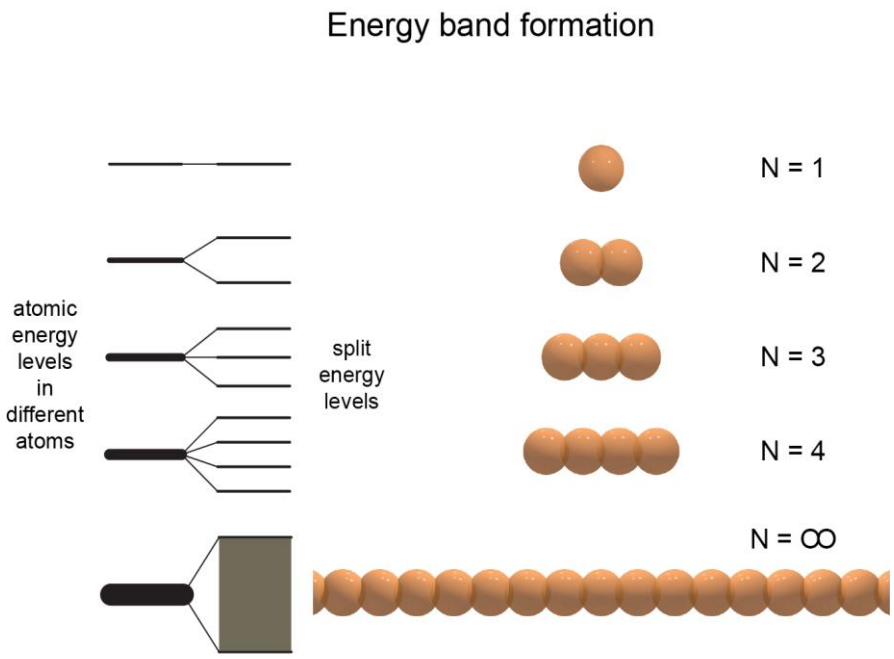


Figure 1-1. Description of energy band's formation. Atomic energy levels in different atoms split into the number of the atoms when they get close to each other. In solids, the number of atoms is infinitely large, and the atoms are close enough to form bonding. Then, the energy levels form continuous "bands" as in the case of the $N = \infty$.

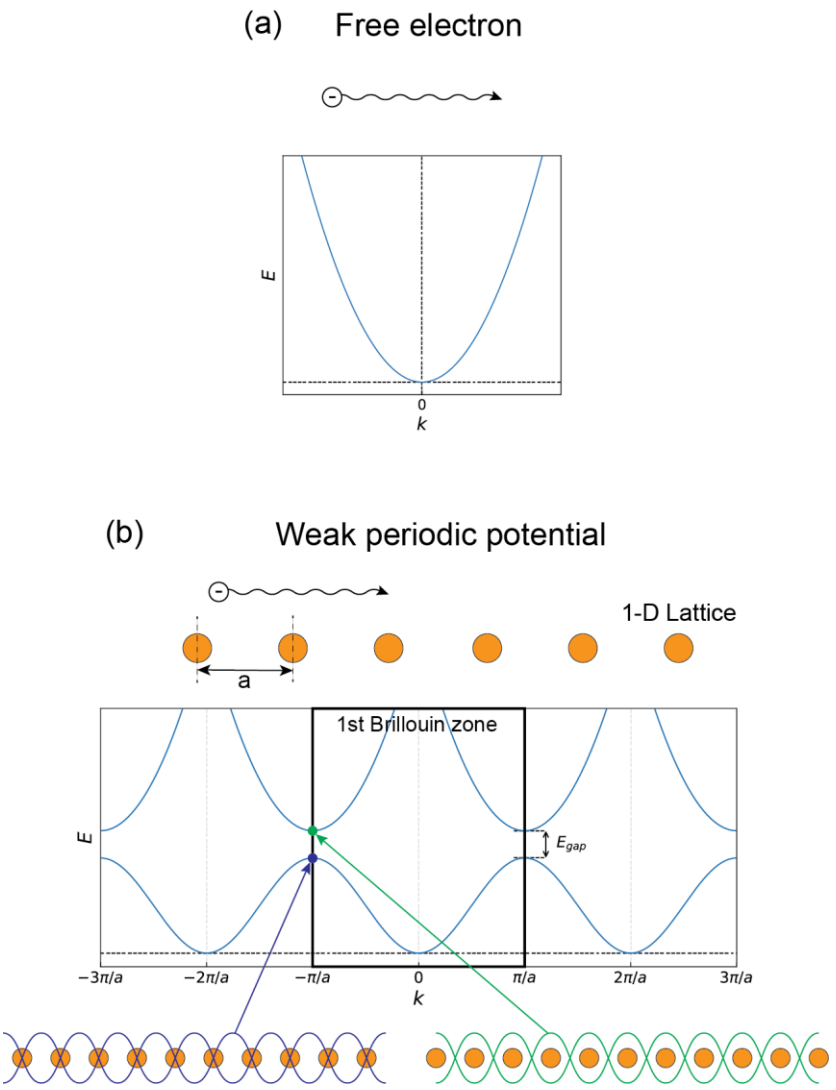


Figure 1-2. Free electron vs electrons in a weak periodic potential. (a) Free electrons have kinetic energy only, $E = \boldsymbol{p}^2/2m$ where $\boldsymbol{p}$ is the momentum and $m$ is the electron's mass. The energy structure $E(k)$ of the free electrons is parabolic. (b) When an electron is moving, it experiences Bragg scattering due to the periodicity, the $E(k)$ becomes periodic and the gap opens at the first BZ boundaries. The lower energy state at the gap is the bonding state colored by blue. The higher energy state is the antibonding state colored by green.

### 1.1.2 Insulator, semiconductor, and conductor from band theory

Materials can be primarily categorized into two groups: insulators and conductors. Insulators are materials that cannot conduct electric current. This is caused by the absence of movable electrons, which means that all of the electrons are bound to some quantum states. In conductors, in contrast, there are unbound electrons which can move along an electric field. This simple classification can be explained by the energy band theory. The existence of conduction electrons is determined by the energy band structure and the location of the Fermi energy (or level, $E_F$), the highest energy of the occupied states. If the $E_F$ is located in a large band gap, typically above 3–4 eV, all of the bands below $E_F$ are fully filled, and the rest of them are completely empty. With an external electric field, the electrons occupying the fully filled bands tend to be shifted along the direction of the field in $k$-space, but they cannot move. This is because there is no additional empty state near the $E_F$, therefore they cannot take new states unless the electric field is extremely strong. They fail to break the charge imbalance along the field direction in usual insulating materials as shown in Figure 1-3(a). In contrast to the insulators, if $E_F$ is found in energy bands rather in a gap, partially filling the bands, thus the electrons can be shifted along an electric field, pushing down one side and up the other side in conductors as shown in Figure 1-3(b). In this way, electrons can be transported through the conductors. There exists an intermediate category with respect to the electrical conduction: semiconductors. As indicated from the name, “semiconductors,” they are conducting or insulating depending on the conditions, usually temperature. Semiconductors have relatively small band gaps and can be conducting at room temperature due to thermal excitation. This property is useful for controlling electrical properties in devices, therefore, semiconductors have been very important materials in scientific study as well as industry.

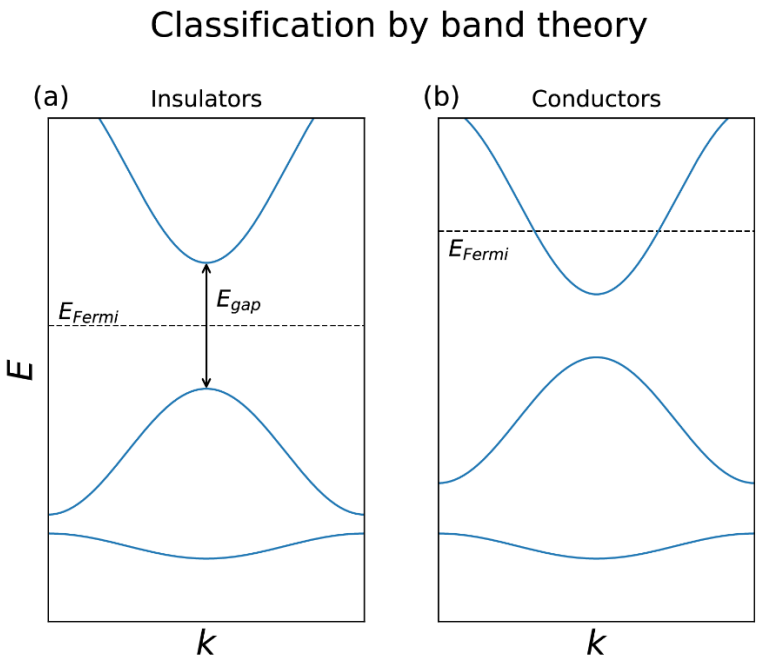


Figure 1-3. Schematic band structures for insulators and conductors. (a) Insulators. The $E_F$ is in the middle of a large band gap, typically above 3–4 eV. (b) Conductors. The $E_F$ crosses some of the bands regardless of the presence of a band gap.

### 1.1.3 Quantum Hall state

Experimental observation of the quantum Hall effect (QHE) ignited research on topological phases and materials in condensed matter physics. A review of the QHE is a good starting point to dive into the TIs as well as other topological phases because other topological phases can be understood with the base of the quantum Hall (QH) phase. In this section, we will introduce the QH phase as a building block of other more complicated topological phases.

Before moving onto the QHE, let us take a moment to briefly look at the ordinary (or classical) Hall effect (OHE). When an external and uniform magnetic field is applied perpendicular to an electric current, the moving electrons are deviated by the Lorentz force, developing a transverse electrical potential difference as shown in Figure 1-4(a) and (b), which is called the "Hall voltage." The Hall voltage divided by the current is defined as the "Hall resistance" which is

proportional to the external magnetic field as in Figure 1-4(c). The emergence of the nonzero Hall voltage is called the OHE. Details of the OHE will be introduced in CHAPTER 3 as a semiclassical theory for film characterization.

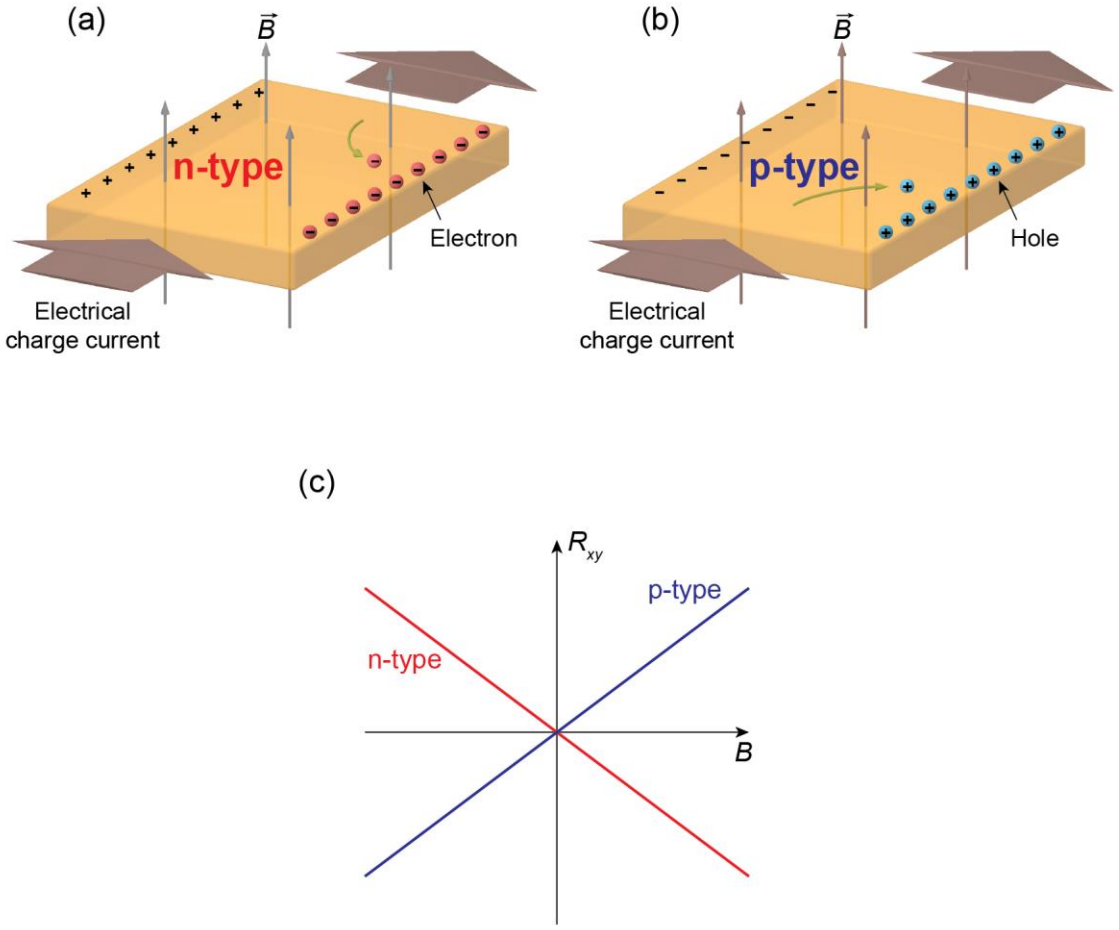


Figure 1-4. Schematics of the OHE and the Hall resistance measurement. Formation of the Hall voltage by the Lorentz force due to an external magnetic field $B$ in (a) electron and (b) hole systems. (c) Typical Hall resistance vs $B$ curves in an n-type system (red) and a p-type system (blue). In the OHE, the Hall resistance is proportional to the $B$ with a negative (n-type) or positive (p-type) slope.

One of the great successes in condensed matter physics is the discovery of the QHE. In 1980, Klaus von Klitzing and his colleagues reported the historic observation of the quantized Hall conductance in a 2D semiconductor material ([4]Klitzing, et al., 1980). Schematics of the QHE and its measurement setup are shown in Figure 1-5(a) and (b). Klitzing *et al*. showed the quantized Hall voltage, shown by multiple plateaus, depending on gate voltage under a strong magnetic field, 18 T, at low temperature, 1.5 K, as shown in the first QHE data in Figure 1-5(c). Looking at the QHE from a different angle, the Hall and longitudinal magnetoresistance can be tracked with the magnetic field. Figure 1-5(d) shows typical Hall and magnetoresistance curves measured on a two-dimensional electron system. The Hall resistance curve shows a typical staircase series of plateaus, constant values in some ranges of the magnetic field. The quantized Hall conductance is integer multiples of fundamental constants in physics with extremely high accuracy as follows:

$$\sigma_H = R_H^{-1} = N\frac{e^2}{h} = \frac{N}{25\,812.807\,572}\ \Omega^{-1}. \tag{1-1}$$

The $N$ are positive integers, $e$ is the fundamental charge, and $h$ is the Planck constant. Surprisingly, the Hall resistance value, 25 812.807 572 Ω ($h/e^2$), the "Klitzing constant" named after the observation, is independent of materials, different geometries, or different sheet carrier densities. In virtue of the form of the Klitzing constant, the QHE can be a good alternative to determining the fine structure constant $\alpha$, $\frac{e^2}{4\pi\epsilon_0\hbar c} = \frac{1}{137.035\,963}$, using the relation $R_H^{-1} = N\frac{e^2}{h} = N\frac{2\alpha}{\mu_0 c}$. Measurement of the electron's anomalous magnetic moment also gives $\alpha$, but it requires a huge calculation effort.

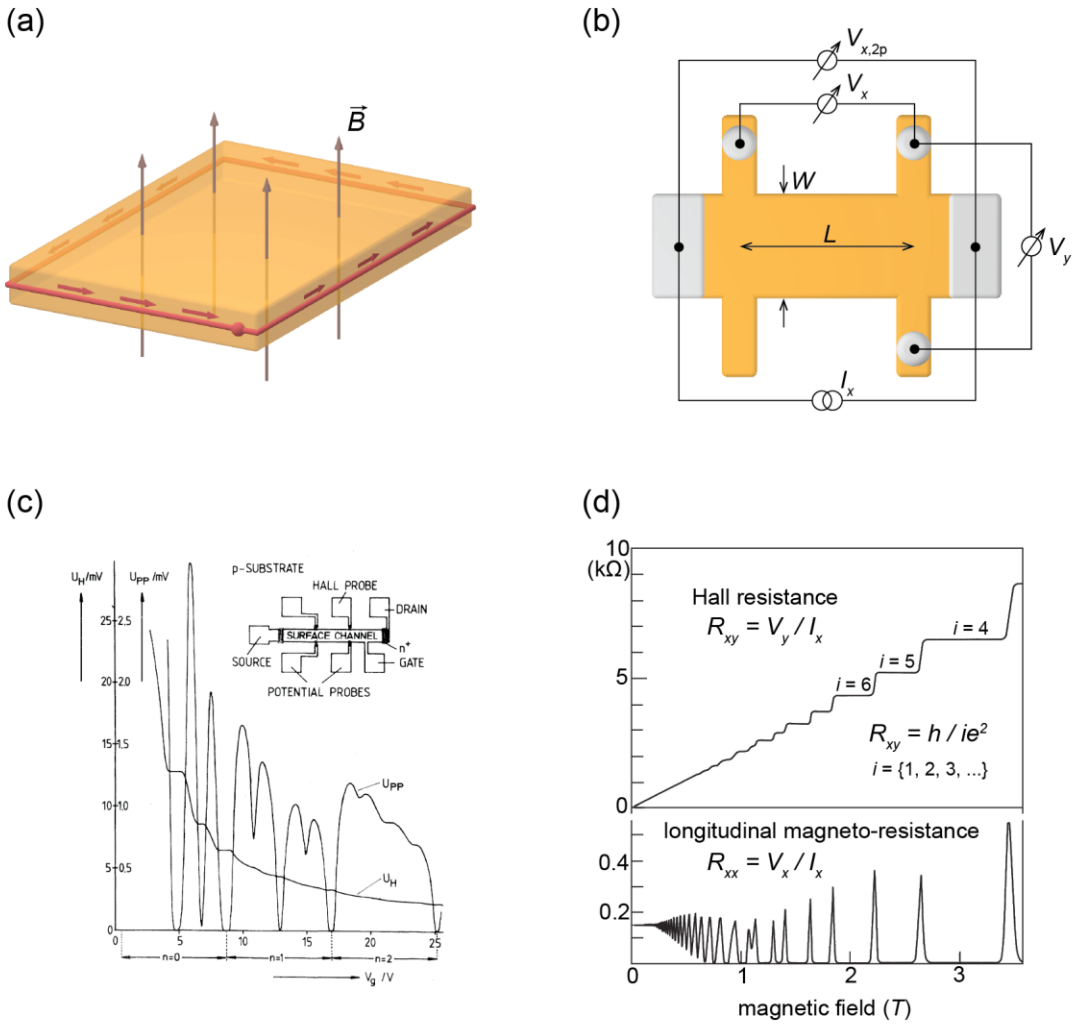


Figure 1-5. The QHE. (a) A schematic of the QH phase. (b) A schematic of the Hall measurement setup. (c) The first QHE data ([4]Klitzing, et al., 1980). (d) Typical Hall resistance and magnetoresistance curves in the QHE. (Redrawn from [5]Weis and Klitzing, 2011).

The quantization of the Hall conductance is intimately related to energy quantization by an external magnetic field, called *Landau quantization* ([6]Landau, 1930). The simple approach to the QHE can start from a general interacting Hamiltonian.

$$H = \frac{1}{2}\left(\vec{p} - q\vec{A}\right)^2 + V(\vec{r}) \tag{1-2}$$

$\vec{p}$ is momentum, $q$ is electrical charge of the electrons, $\vec{A}$ is vector potential, and $V(\vec{r})$ is the scalar potential at $\vec{r}$. The potential $V(\vec{r})$ is ignored for free electrons. For the vector potential in the presence of a magnetic field, we need to choose a proper gauge to deal with the corresponding Schrödinger equation (SE, $H\psi(\vec{r}) = E\psi(\vec{r})$). Let us take $\vec{A} = (0, Bx, 0)$, the Landau gauge, where $B$ is the external magnetic field perpendicular to a 2DEG, and $q = -e$ where $e$ is the elementary charge. With this gauge, we can factorize the wave function as $\psi(\vec{r}) = \psi(x, y) = u(x)\exp(iky)$ because the Hamiltonian does not depend on $y$. Then, the simplified SE only in $x$ can be obtained as

$$\left[-\frac{\hbar^2}{2m}\frac{d^2}{dx^2} + \frac{1}{2}m\omega_c\left(x + \frac{\hbar k}{eB}\right)^2\right]u(x) = Eu(x) \tag{1-3}$$

Now, we can consider the SE as a one-dimensional harmonic oscillator with the center displaced by $x_k = -\frac{\hbar k}{eB}$. Therefore, we can simply write down the energy levels:

$$E_{nk} = \left(n - \frac{1}{2}\right)\hbar\omega_c \tag{1-4}$$

The energy levels, $E_{nk}$, are called *Landau levels* (LLs). The LLs are evenly spaced in nonrelativistic systems, which is similar to simple harmonic oscillators (SHOs) with $\omega_c = \frac{eB}{m}$, the cyclotron frequency as shown in Figure 1-6(a). The number of states in an LL can be counted by consideration of $x_k = -\frac{\hbar k}{eB} < L_x$ as

$$n_{LL} = \frac{eB}{h} \tag{1-5}$$

Using Equation (1-5), we can define the filling factor $\nu$ as the two-dimensional sheet carrier density ($n_{2D}$) of the system divided by the number of states in an LL ($n_{LL}$).

$$\nu = \frac{n_{2D}}{n_{LL}} \tag{1-6}$$

The $\nu$ is the same as the $N$ in Equation (1-1) whenever the $\nu$ becomes an integer.

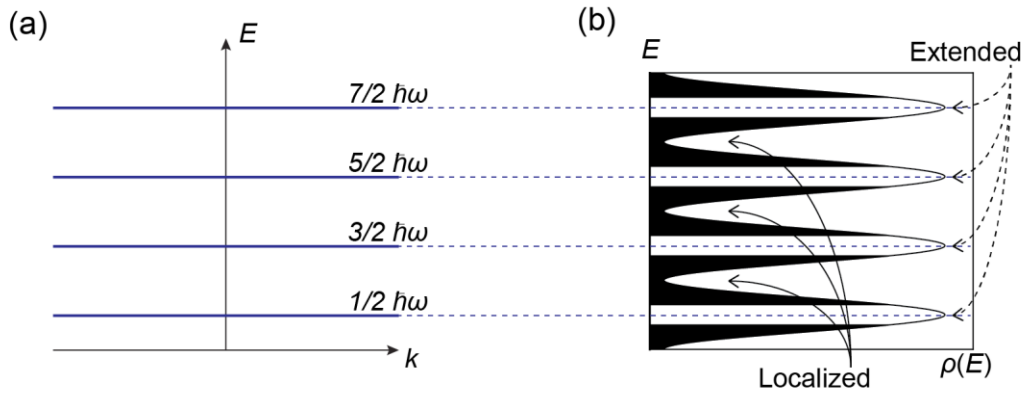


Figure 1-6. Energy levels from Landau quantization. (a) The first few of the nonrelativistic LLs: $E_{nk} = (n - ½)\hbar\omega_c$ with $n$ = 1, 2, 3, and 4. (b) The LLs broaden by scattering events (phonons, impurities, etc.). The centers of the LLs remain extended states where the electrical current flows through the entire area of the 2DEG. In contrast, the tails (black) are localized, so that they do not contribute to the electrical conduction.

The LLs appears as sharp peaks like delta functions in Figure 1-6(a) where the electrons do not undergo any scattering events. However, the LLs, in reality, broaden because the electrons are scattered by impurities, phonons, etc. as in Figure 1-6(b). There remain extended states at the centers of the LLs where the electrical current flows through the entire area of the 2DEG. In contrast, the states in tails indicated by black are localized, so that they do not contribute to the electrical conduction. When the Fermi level sits within the localized states, the 2DEG becomes a 2D insulator, but enters the QH phase.

One of the most important properties of the QH state is the existence of *edge states* which is shown as a red line surrounding the sample in Figure 1-5(a). In the classical regime, the $B$ field makes the electrons deviate, and even form circular orbits if the $B$ is strong enough. In this way, most of the sample area becomes insulating, leaving skipping orbits at the edges as in Figure 1-7(c)

([7]Halperin, 1982). In the quantum mechanical regime, the appearance of the edge states in the QH state can be explained by considering the center of charge distribution. The center of the charge distribution, wave functions or eigenfunctions, at the energy level $E_{nk}$ is $x_k = -\frac{\hbar k}{eB}$, which is the center of the harmonic (effective magnetic) potential, $\frac{1}{2}m\omega_c\left(x+\frac{\hbar k}{eB}\right)^2$, in the system. The strong $B$ field confines the charge distribution more tightly, and the nonzero $k$ makes the center of the distribution shift toward the edges. Here, the $k$ is along the $y$-axis, which can be written as $k_y$. Then, the energy structure in real space is modified accordingly as illustrated in Figure 1-7(a) and (b). Because the direction of the $k_y$ determines the shift direction of the edge states, the edge states become chiral. The chirality means that the conduction through the channels is one way as illustrated in Figure 1-5(a), which is due to broken time-reversal (TR) symmetry. Consequently, if the electrons are in motion, then they can propagate only near the edges under the strong $B$ field with a chirality.

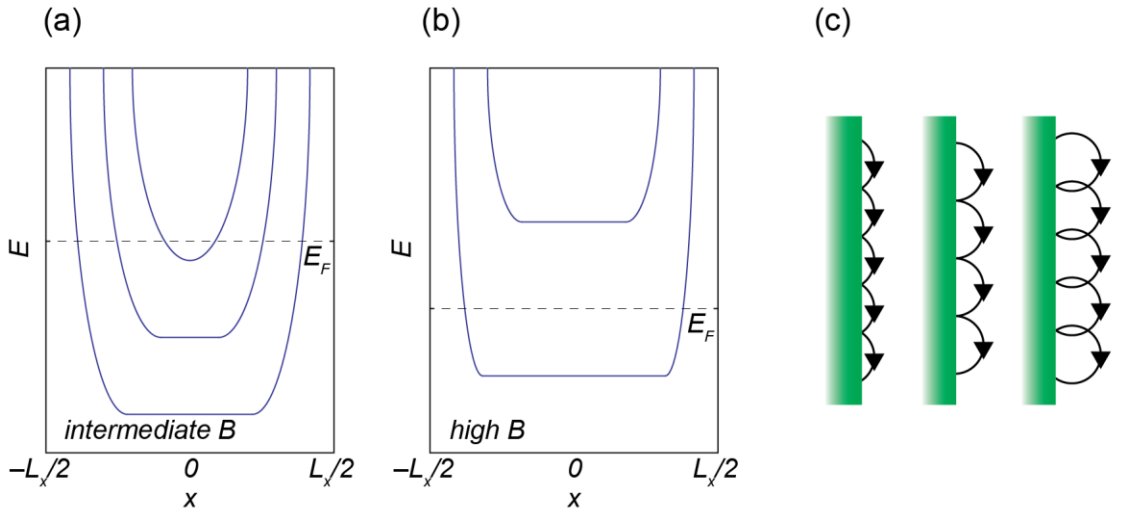


Figure 1-7. Modified energy structures and schematics of the edge channels in the QH state. (a, b) As the $B$ field is increased, the energy structure develops from (a) to (b) due to the effective magnetic potential, $E_{nk} = \frac{1}{2}\hbar\omega_c (x + \hbar k/eB)^2$, and the center of the wave function, $x_k = -\hbar k/eB$. (c) Interpretation of the edge state in the classical regime: skipping orbit motion.

In this section, we briefly introduced fundamental properties of the QH state. The Landau quantization and the emergence of the edge states are not only the results of the quantum mechanical consideration with the Hamiltonian in Equation (1-3), but also the fruit of topology. In the following sections, we will introduce a topological invariant, the Chern number, and take a topological look at the QH state.

## 1.2 A topological look: Topological invariant

The QH state is different from band insulating states in the sense of topological phase in matter. The filling factor $\nu$ is closely related to the topological nature, and the edge states are a result of the nontrivial topology as will be explained. To understand the topological nature of the QH state, the Chern number should be introduced as a topological invariant.

Topological characters of geometric bodies were quantified by Gauss and Bonnet, which categorize the characters with integer, thus discrete, values. The values are constructed by integrating the local curvature ($K$) of the geometric body over the entire surface ($S$).

$$\frac{1}{2\pi}\int_S K dA = 2(1-g) \tag{1-7}$$

The integration consequently results in an integer, $g$, called "a genus," which corresponds to the number of holes in the object. Some examples are in Figure 1-8. The genus of spheres is 0 because spheres do not have any holes as in Figure 1-8(a). However, the torus in Figure 1-8(b) and a little more complicated object in Figure 1-8(c) have one and two holes, respectively. By smooth deformation, one cannot become another.

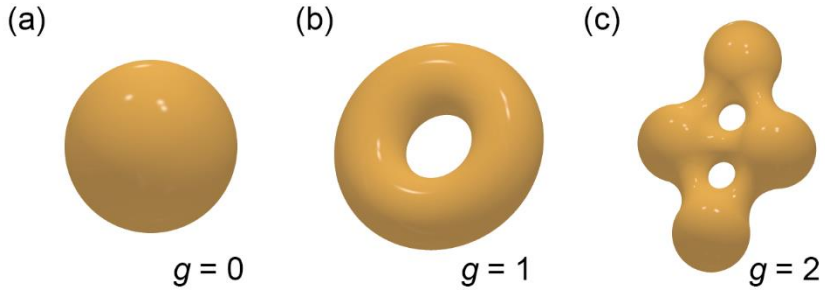


Figure 1-8. Topological classification of geometric forms with the genus, $g$. (a) A sphere, $g = 0$. (b) A torus, $g = 1$. (c) A complicated body with two holes, $g = 2$.

People have started using the concept of "topology" to explain novel properties such as superconductivity (SC), QHE, and superfluid and to classify topological materials in condensed matter physics, eventually leading to the new age of topological materials as recognized with the 2016 Nobel prize in physics. In material classification, the topological character is featured by a topological number, the so-called *Chern number* which is determined by a geometric phase in matter, the *Berry phase*. Figure 1-9(a) shows a simple example of nonzero Berry phase with a simple pendulum. Imagine that the pendulum starts moving from the North pole with an oscillation, and goes to the equator passing through Portland. Then, it moves along the equator, and at some point, comes back to the North pole as shown in Figure 1-9(a). Though the pendulum comes back to exactly the same location, the oscillation angle should be changed depending on the movement along the equator. The change of the angle is a kind of Berry phase. If it is not zero modulo $2\pi$, then the state of the oscillation is not trivial with respect to the loop. We will take a brief look at what the Berry phase is and how to construct it. A more detailed explanation is in Ref. ([8]Vanderbilt, 2018).

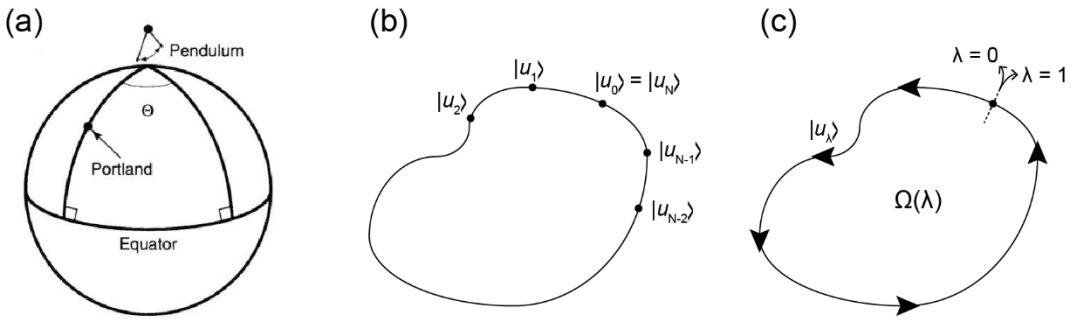


Figure 1-9. Description and construction of the Berry phase. (a) An oscillating simple pendulum departs the North pole, going to the equator. Moving along the equator, it stops at a different latitude Θ, and comes back to the North pole. Then, the final angle of the oscillation differs from the initial angle by Θ: the Berry phase. Figure is adapted from Ref. ([9]Griffiths, 2005). Quantum mechanical wave function sets in cyclic loops in (b) discrete and (c) continuous regime.

In QM, the Berry phase is a geometrical phase difference between initial and final wave functions in a cyclic adiabatic evolution. Figure 1-9(b) and (c) illustrates the evolutions in discrete and continuous manners. For the discrete cyclic set of wave functions as in Figure 1-9(b), the Berry phase is defined as

$$\phi = -\mathrm{Im}\ln[\langle u_0|u_1\rangle\langle u_1|u_2\rangle\cdots\langle u_{N-1}|u_N\rangle] \tag{1-8}$$

In a similar way, the Berry phase becomes as follows for the continuous cyclic evolution in Figure 1-9(c),

$$\phi = -\mathrm{Im}\oint\langle u_\lambda|\partial_\lambda u_\lambda\rangle d\lambda \tag{1-9}$$

By taking a quick look at the integrand, $\langle u_\lambda|\partial_\lambda u_\lambda\rangle$, it is pure imaginary. Therefore, Equation (1-9) can be written as

$$\phi = \oint\langle u_\lambda|i\partial_\lambda u_\lambda\rangle d\lambda. \tag{1-10}$$

This is the expression for the Berry phase in continuous evolution ([10]Berry, 1984). Let us consider 2D space for simplicity. The integrand in Equation (1-10) is called the "Berry potential," $\boldsymbol{A}(\boldsymbol{\lambda}) = \langle u_{\boldsymbol{\lambda}} | i\partial_{\boldsymbol{\lambda}} u_{\boldsymbol{\lambda}} \rangle$, and the equation is simplified to be

$$\phi = \oint \langle u_{\boldsymbol{\lambda}} | i\partial_{\boldsymbol{\lambda}} u_{\boldsymbol{\lambda}} \rangle \cdot d\boldsymbol{\lambda} = \oint_C \boldsymbol{A}(\boldsymbol{\lambda}) \cdot d\boldsymbol{\lambda}. \tag{1-11}$$

The Berry curvature or Berry flux, $\Omega(\boldsymbol{\lambda})$, is defined as the Berry phase in a unit area in the $(\lambda_x, \lambda_y)$ space. The Berry curvature is the curl of the Berry potential,

$$\Omega(\boldsymbol{\lambda}) = \nabla \times \boldsymbol{A}(\boldsymbol{\lambda}) \tag{1-12}$$

then, the Berry phase can be rewritten by Stokes' theorem as

$$\phi = \oint_C \boldsymbol{A}(\boldsymbol{\lambda}) \cdot d\boldsymbol{\lambda} = \int_S [\nabla \times \boldsymbol{A}(\boldsymbol{\lambda})]\, dS = \int_S \Omega(\boldsymbol{\lambda})\, dS. \tag{1-13}$$

By a generalization of the expression of the Berry phase in Equation (1-13) to 3D space, the Berry phase in 3D becomes

$$\phi = \oint_C \boldsymbol{A}(\boldsymbol{\lambda}) \cdot d\boldsymbol{\lambda} = \int_S \boldsymbol{\Omega}(\boldsymbol{\lambda}) \cdot d\boldsymbol{S}. \tag{1-14}$$

Strictly speaking, the last equal sign "=" is not proper here because the Berry curvature is fully gauge invariant and the Berry phase $\phi$ is meaningful only modulo $2\pi$. Therefore, the exact expression should be

$$\int_S \boldsymbol{\Omega}(\boldsymbol{\lambda}) \cdot d\boldsymbol{S} \doteqdot \oint_C \boldsymbol{A}(\boldsymbol{\lambda}) \cdot d\boldsymbol{\lambda}. \tag{1-15}$$

The "≒" means that the unambiguously determined left-hand side is equal to one of the values of the right-hand side modulo $2\pi$.

According as the Chern theorem states, the integral of the Berry curvature over any closed 2D manifold is

$$\oint \boldsymbol{\Omega}(\boldsymbol{\lambda}) \cdot d\boldsymbol{S} = 2\pi m \tag{1-16}$$

where the $m$ can be integers. The $m$ is called a "Chern number" or "Chern index" regarded as a "topological invariant." This is analogous to what Gauss–Bonnet developed in Equation (1-7). If the Chern number of a geometric body is zero, it means the shape of the body is topologically trivial.

However, once the Chern number has a nonzero value, then it is said to be topological, or topologically nontrivial.

In realistic materials, the Chern number is defined by the Berry flux in the BZ in a reciprocal space as

$$n_m = \frac{1}{2\pi}\oint \boldsymbol{\Omega}_m(\boldsymbol{k}) \cdot d\boldsymbol{k}. \tag{1-17}$$

$n_m$ is the Chern number of the $m^{\text{th}}$ energy band, and the $\boldsymbol{\Omega}_m$ is the Berry curvature defined by $\boldsymbol{\Omega}_m = \nabla_{\boldsymbol{k}} \times \boldsymbol{A}_m$, where $\boldsymbol{A}_m = i\langle u_m|\nabla_{\boldsymbol{k}}|u_m\rangle$, and $|u_m\rangle$ is the $m^{\text{th}}$ Bloch wave function. The total Chern number, $n = \sum_{occ} n_m$, the summation over all the occupied bands, is invariant under smooth deformation of the energy bands.

In 1981, Robert Laughlin developed an argument to explain Klitzing's discovery via a *Gedanken* experiment ([11]Laughlin, 1981). Figure 1-10 shows a schematic illustration of the Gedanken experiment where Laughlin interpreted the QHE as a quantum pump. It is assumed that the 2DEG is confined to a looped ribbon, and a strong magnetic field, *B*, is applied normal to the surface. The two different edges of the ribbon are connected to independent electron reservoirs. Then, Laughlin introduced a fictitious magnetic flux Φ threading the loop. The pump is driven by change in the flux. Increasing the flux produces electromotive force around the ring by which the charge transfer happens from one reservoir to the other.

The conductance of the charge transfer is determined by the Aharonov–Bohm effect. In 1959, Yakir Aharonov and David Bohm pointed out that electrons propagating on different sides of a magnetic field in a finite area show interference even though they went through field-free vacuum space ([12]Aharonov and Bohm, 1959). This is a purely quantum mechanical effect, and the calculated single magnetic flux quantum is *h/e*. Increasing the single quantum in the flux is one cycle of the pump. Therefore, the Hall conductance is quantized in units of $e^2/h$. However, in QM, the measurement outcomes are not necessarily reproduced from the same quantum state even though the state is kept the same by gauge invariance before and after the charge transfer occurs.

In other words, we cannot guarantee the same number of electrons is transferred in each cycle. Therefore, topological quantum numbers kick in to quantize the averages: Chern numbers.

In 1982, D. Thouless *et al*. showed that the integer $N$ in Equation (1-1) comes from its topological nature. They showed that the $N$ is equivalent to the Chern numbers, topological invariants, so-called TKNN (Thouless–Kohmoto–Nightingale–den Nijs) invariants named after the discoverers ([13]Thouless, et al., 1982). Using the Kubo formula, TKNN showed that the $N$ in Equation (1-1) is identical to the total Chern number $n$ in the previous section. This means that it cannot change when the Hamiltonian varies smoothly as the Gauss–Bonnet theorem states and that the QH state is a topologically nontrivial insulating state that is different from usual band insulating states.

The bottom plot of Figure 1-5(d) shows a typical longitudinal magnetoresistance vs magnetic field plot in which the resistance becomes zero whenever the Hall resistance is quantized. The dissipationless edge channels in the QH state also have a topological nature. Let us imagine a QH state with the filling factor 1, that is Chern number 1. The QH state is in a vacuum environment whose Chern number is 0. As explained before, one state cannot become a topologically different state via smooth deformation without gap closure. This means that there must be conducting states at the boundary between the areas with different Chern numbers. In other words, the difference of the Chern numbers between the two areas indicates the number of edge channels at the boundary as shown in Figure 1-11. The edge channels are immune to local disorder due to the topological nature, thus dissipationless.

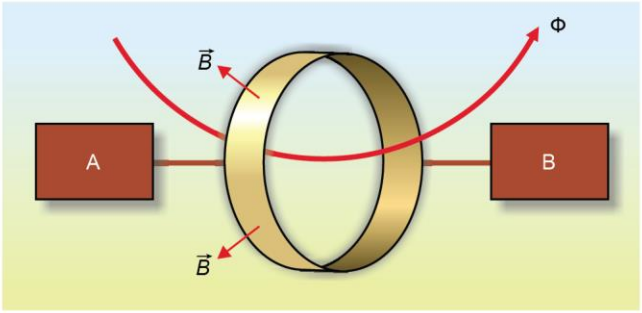


Figure 1-10. Laughlin's Gedanken experiment for the QHE. The 2DEG is confined to a ribbon. Laughlin interpreted the QHE as a quantum pump operated by the fictitious magnetic flux Φ. Whenever the Φ threads the ribbon, a quantized amount of charge transfer between the reservoir A and B occurs. (Redrawn from [14]Avron, et al., 2003).

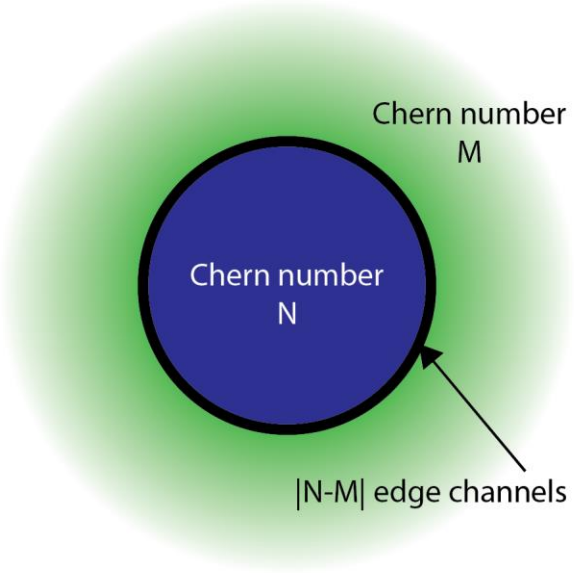


Figure 1-11. Presence of the conducting edge channels at the boundary between two different insulators with different Chern numbers.

## 1.3 Topological insulators

### 1.3.1 $Z_2$ topological insulators

The Chern numbers can distinguish the QH state from other normal insulating states, which is known as "***Z*** *classification*." In 2005, C. Kane and E. Mele introduced a similar invariant to the TKNN that identifies TR invariant systems, the so-called "$\boldsymbol{Z}_2$ topological invariant" ([15]Kane and Mele, 2005a). The $\boldsymbol{Z}_2$ invariant distinguishes trivial insulating phases from the quantum spin Hall phases as will be explained in the following section. When two opposite spin channels are well decoupled, spin-up and spin-down for simplicity, in a 2D system, the Chern numbers can be defined separately for the two channels as ($C_\uparrow$, $C_\downarrow$), which could be called $\boldsymbol{Z} \times \boldsymbol{Z}$ classification. If TR symmetry is preserved in the system, the total Chern number should be zero, $C_{\text{tot}} = C_\uparrow + C_\downarrow = 0$. However, both of the Chern numbers do not need to be zero simultaneously, rather ($C_\uparrow$, $C_\downarrow$) = ($n$, $-n$) is available, where $n$ is an integer. When $n$ is odd, the system is called "$\boldsymbol{Z}_2$-odd," which is topologically nontrivial. On the other hand, the system with even $n$ is called "$\boldsymbol{Z}_2$-even," which is topologically trivial.

Under the preservation of TR symmetry, the $\boldsymbol{Z}_2$-odd phase can be caused by strong spin–orbit coupling (SOC), leading to band inversion near the Fermi level. The band inversion leaves the "edge states" due to the nontrivial topology. Figure 1-12 shows the typical band structures of (a) the $\boldsymbol{Z}_2$-even and (b) $\boldsymbol{Z}_2$-odd phases. The Fermi level in the $\boldsymbol{Z}_2$-even phase can become an insulator by smooth adjustment of $\Gamma_a$, $\Gamma_b$, or the position of the Fermi level. In contrast, the $\boldsymbol{Z}_2$-odd phase, however, must have the Fermi level crossing a band as shown in Figure 1-12(b).

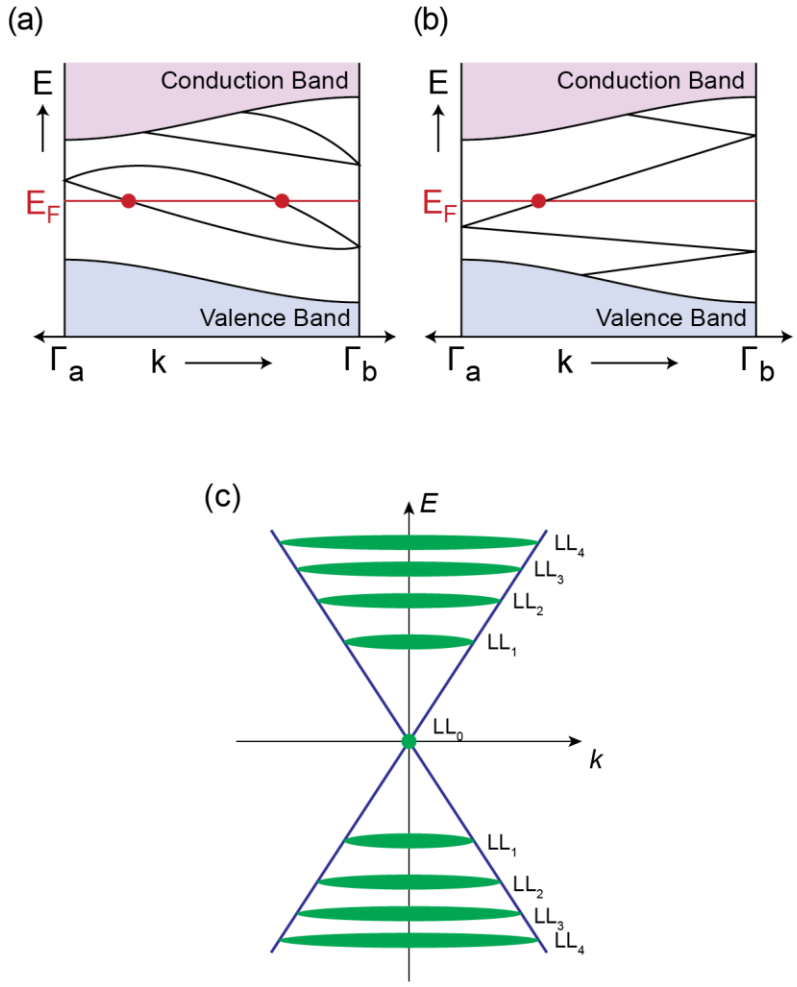


Figure 1-12. Comparison of the band dispersions of $\boldsymbol{Z}_2$ topological insulators and relativistic LLs. (a) $\boldsymbol{Z}_2$-even. The Fermi level crosses two (even) bands, and it could sit in the insulating gap by smooth deformation of the band structure. (b) $\boldsymbol{Z}_2$-odd. The Fermi level must cross one (odd) band. (a, b) (Figures are adapted from [16]Hasan and Kane, 2010). (c) Landau quantization of massless Dirac fermions. Topological materials usually have Dirac-like (linear) band dispersion. Therefore, their LLs follow $E_n = \pm(2e\hbar v_F^2 B|n|)^{1/2}$.

The emerging edge states most likely have linear dispersion, which can be described by the massless Dirac Hamiltonian,

$$H_{edge\ or\ surface} = -i\hbar v_F \vec{\sigma} \cdot \vec{\nabla}. \quad (1\text{-}18)$$

The Hamiltonian leads to the different energy levels of the Landau quantization as

$$E_n = \pm\sqrt{2e\hbar v_F^2 B|n|} \quad (1\text{-}19)$$

Equation (1-19) gives the relativistic LLs in the edge or surface states, which is illustrated in Figure 1-12(c).

### 1.3.2 2D TIs: Quantum spin Hall insulators

To understand the TIs better, we should note that the 2D TIs are known as the quantum spin Hall (QSH) insulators. The spin Hall effect (SHE) is a transport phenomenon in which spin accumulation develops on the lateral sides, unlike the OHE in which electrical potential difference occurs instead. This phenomenon occurs without an external magnetic field. Figure 1-13 illustrates schematics of the SHE. In the SHE as shown in Figure 1-13, when an electrical charge current flows in a direction, a spin movement appears in the perpendicular direction. This is attributed to the opposite directions of the deviation of the spins with different orientations, up and down, thereby the two spin channels are well separated. The spin movement is called "spin current" which occurs with no net charge transport in the transverse direction. Consequently, different spins pile up on the different sides. The term "spin Hall effect" was introduced by J. E. Hirsch in 1999 ([17]Hirsch, 1999), but the SHE was first predicted by Mikhail I. Dyakonov and Vladimir I. Perel in 1971 ([18]Dyakonov and Perel, 1971a; [19]1971b) about 30 years previously. It was experimentally first demonstrated by A. A. Bakun *et al*. in 1984 in the inverse regime ([20]Bakun, et al., 1984), and the direct SHE was observed in 2D semiconductor systems by Y. K. Kato *et al*. and J. Wunderlich *et al*. more than 30 years after the first prediction ([21]Hosten and Kwiat, 2004; [22]Wunderlich, et al., 2005). People are still debating the origin of the SHE.

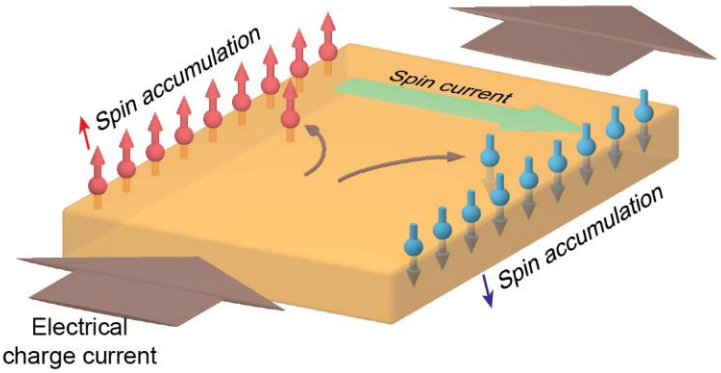


Figure 1-13. A schematic of the SHE. Red and blue indicate the different spin states. The charge flows get deviated by the spin states, producing the spin current without an external magnetic field.

The QSH state can be understood as a 2D insulating state surrounded by the spin currents of the SHE. Figure 1-14(c) shows a schematic illustration of the QSH state. The spin-up current colored by red flows counterclockwise, and the spin-down colored by blue goes the other way. These 1D conducting edge states can be interpreted as a combination of the two QH states with opposite magnetic fields displayed in Figure 1-14(a) and (b). The magnetic fields are cancelled out in the 2D bulk, but the chiral edge states are still alive in the QSH state due to each of the nontrivial topologies being preserved. This results in the two "spin-dependent" 1D channels juxtaposed in the edge states. In other words, the $\boldsymbol{Z}_2$ indices are not zero though their summation is zero, therefore, the edge states are topologically protected by TR symmetry. The edge states of the QSH state are immune even to strong disorder due to the topological nature as indicated by the $\boldsymbol{Z}_2$ indices while electronic states are usually weak against disorder by Anderson localization ([23]Anderson, 1958; [24]Lee and Ramakrishnan, 1985).

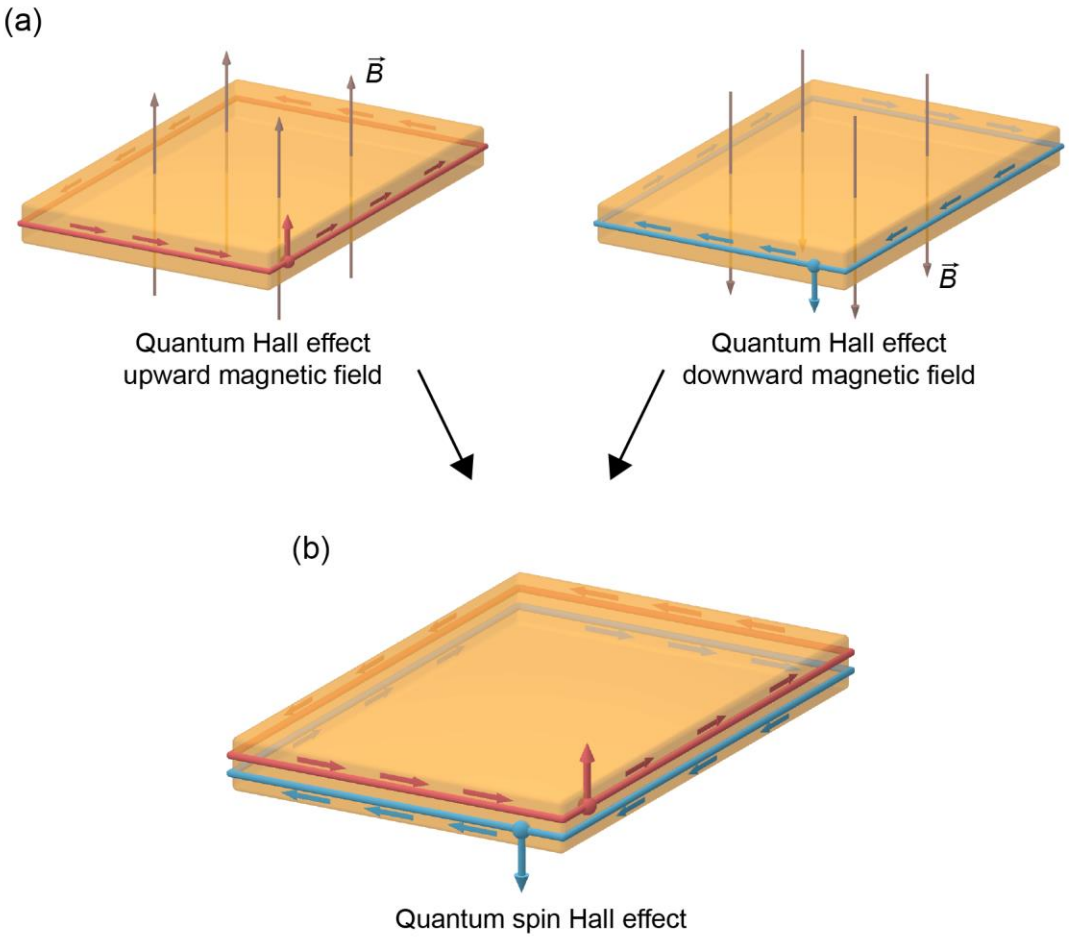


Figure 1-14. Description of the QSH state as a superposition of the two QH states. The combination of the QH state with (a) upward *B* and the one with (b) downward *B* results in (c) the QSH state with preserved nontrivial topology.

Kane and Mele showed that the reflection amplitude coming from the scattering centers, disorders, is odd under TR operation, suppressing backscattering ([25]Kane and Mele, 2005b): the weak antilocalization (WAL). This effect is illustrated in Figure 1-15(a). When the electrons are moving through an edge channel, and meet a scattering center, they should follow one of the two

time-reversible paths. The phase difference between the two paths after the scattering events is $2\pi$, which leads to a quantum mechanical phase factor of $-1$, thereby destructive interference. The WAL effect is shown as a sharp cusp in magnetoconductance as in Figure 1-15(c). It is compared with the weak localization (WL) in Figure 1-15(b) which is the opposite effect to the WAL. The transport along the edge becomes "ballistic" at $T = 0$. Ballistic transport means that the charge propagation does not experience any scattering event ([26]Büttiker, 1988). In reality, of course, inelastic backscattering processes at the scattering centers are allowed at nonzero temperature, leaving a nonzero conductivity.

The initial idea of the QSH state was proposed in 1987 ([27]Pankratov, et al., 1987), and the QSH state was predicted in a realistic material, graphene ([25]Kane and Mele, 2005b) and 2D semiconductor systems ([28]Bernevig and Zhang, 2006). However, the insulating band gap of graphene was likely to be small due to relatively weak SOC. Not much later, the very realistic consideration of the quantum well structure, CdTe–HgTe–CdTe which is known as a material with strong SOC ([29]Dornhaus, et al., 1983), by B. A. Bernevig, T. L. Hughes, and S. C. Zhang ([30]Bernevig, et al., 2006) has boosted the first experimental observation of the first signature of the QSH state achieved by M. König *et al*. in 2009 ([31]König, et al., 2007) within a year of the theoretical proposal.

Figure 1-16 shows the experimental data of the first signature of the QSH. The topology is determined by the thickness of the middle layer, HgTe. If it is thicker than the critical value 6.5 nm, the system is topological while it is not with a thinner HgTe layer. In the topological regime, the study shows the edge bands and the quantized longitudinal resistance in the right of Figure 1-16(c) compared with normal insulating bands and its nonmeasurable resistance in the left. The quantized longitudinal resistance can be understood as the ballistic edge state transport at low temperature: the Landauer–Büttiker formalism, which tells about the quantized conductance $e^2/h$ associated with each set of edge states ([26]Büttiker, 1988).

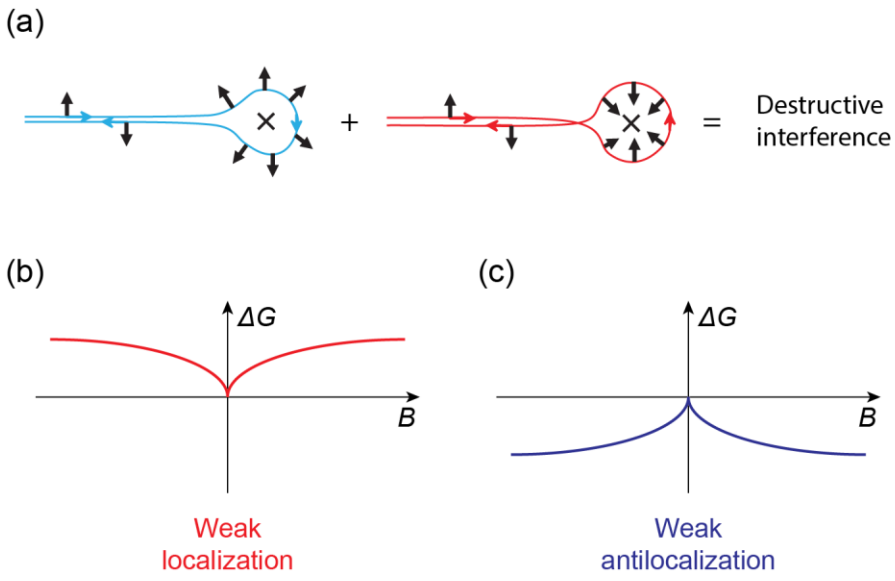


Figure 1-15. Description of weak antilocalization. (a) The summation of the charge propagation along the two TR invariant paths in the edge channels of the QSH state results in a "destructive interference," leading to suppressed backscattering. The figure is redrawn from Ref. ([32]Qi and Zhang, 2010). (b, c) (b) WL is shown by a cusp, low conductivity at $B = 0$. (c) WAL is shown by another cusp, higher conductivity at $B = 0$.

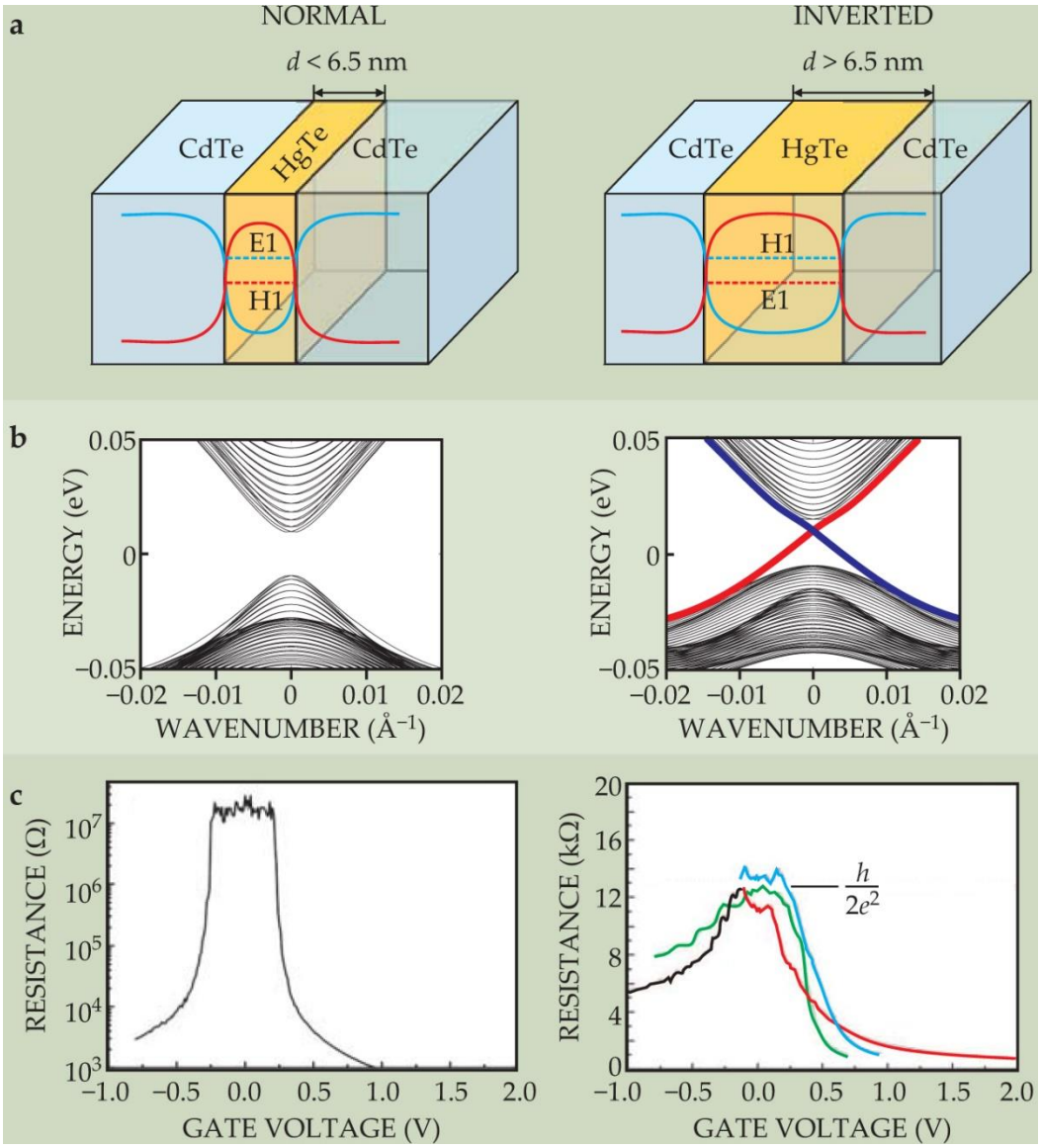


Figure 1-16. CdTe–HgTe–CdTe quantum wells in the normal and topological regime as the QSH state. Compared with the normal insulating state, the QSH (inverted) state shows (b) the topological bands and (c) the quantized resistances. (Figures are adapted from [32]Qi and Zhang, 2010).

### 1.3.3 3D TIs: Weak and strong TIs

The $\boldsymbol{Z}_2$ topological invariants for 3D TIs consist of four indices, ($\nu_0$; $\nu_1'$, $\nu_2'$, $\nu_3'$) where $\nu_i \in \{0, 1\}$ ([33]Fu and Kane, 2007; [2]Moore and Balents, 2007; [34]Roy, 2009). The $\nu_0$ is the strong index that

determines if the 3D TI is a strong TI or not, constructed by the other indices, $\nu_1'$, $\nu_2'$, and $\nu_3'$ which are defined in the reciprocal space as sketched in Figure 1-17. The eight dots are so-called TR invariant momenta (TRIM) in the first BZ where the Kramer's degeneracy is held. Each line and plane is the TR invariant lines and planes, respectively. From the relation between the strong index $\nu_0$ and the others ([8]Vanderbilt, 2018), the 3D TIs with $\nu_0$ even, but at least one of the other $\nu_i$s is odd, are called "*weak*" TIs, and ones with $\nu_0$ odd are called "*strong*" TIs.

To construct the TIs in 3D, we can think about a stack of QSH insulators. Once the stack is thick enough, it may become a 3D system with keeping its own topology. Let us imagine the QSH sheets arrayed along the out-of-plane direction as in Figure 1-18(c). If the layers are initially far enough apart to be independent of each other, no charge flow would occur along the out-of-plane direction as expected. In this case, the $\nu_3$ does not change in the BZ, that is $\nu_3 = \nu_3'$. This means that the system is not topological along the out-of-plane direction. As we decrease the space between the layers, they start to interact with the adjacent layers, leading to variation in the band structure. However, the $\nu_0$ cannot become odd without a band gap closure. Therefore, a simple stack of the QSH insulators is just a weak TI without spin current occurring along the stacking direction.

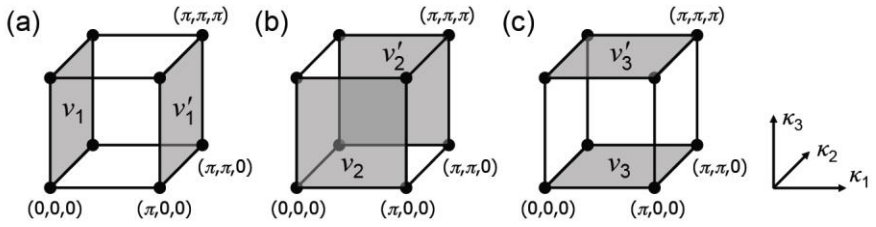


Figure 1-17. Definition of the $\boldsymbol{Z}_2$ indices of the 3D TIs in reciprocal space. The heavy dots are TRIM. (Adapted from [8]Vanderbilt, 2018).

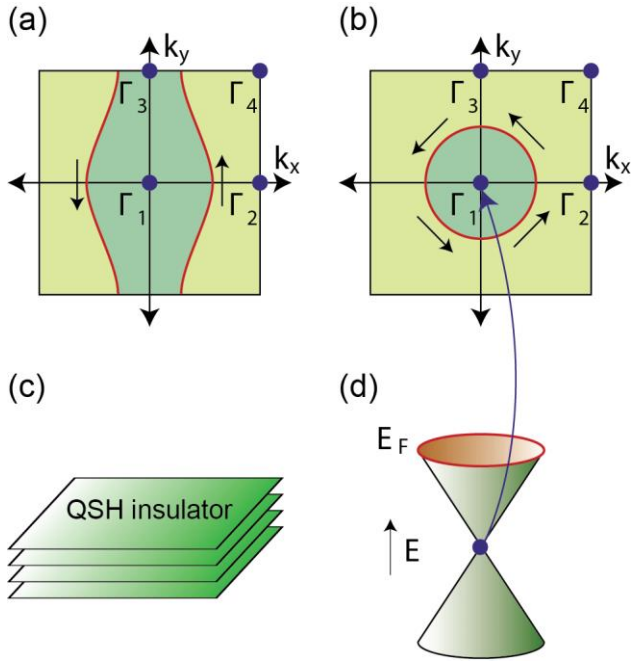


Figure 1-18. Comparison of the weak and strong TIs. (a) Fermi surface of a weak TI. The Fermi surface encloses an even number of TRIM points. (b) Fermi surface of a strong TI. The Fermi surface encloses an odd number of TRIM points. (c) A stack of QSH insulators, which is a weak TI. (d) Dirac cone of a strong TI. (Figures are adapted from [16]Hasan and Kane, 2010).

On the other hand, the strong TIs are represented by $\nu_0$ odd. The $\boldsymbol{Z}_2$-odd, $\nu_0$ odd, results in an odd number of the TRIM enclosed by the surface Fermi circle in the first BZ. Figure 1-18(b) and (d) shows the simplest case of the band dispersion and Fermi circle in strong TIs which is compared with the case of weak TIs shown in Figure 1-18(a). The surface states of the 3D TIs can be understood as the edge states of the 2D TIs extended to 3D. In the 2D TIs, one or the other way propagation of charge carriers is determined by the spin-up or -down state, which is spin-dependent 1D transport. In the 3D TIs, spin-dependent 2D transport occurs, which is coming from the spin–momentum locking as shown in Figure 1-18(b). The spin–momentum locked state is called a

"helical spin state" which is one of the results from the Dirac equation. The helical spin structure leads to the WAL effect in 3D TIs.

The first experimental realization of a 3D TI was $Bi_{1-x}Sb_x$, reported in 2008 ([35]Hsieh, et al., 2008) about a year after its theoretical prediction in a small $x$ range ([33]Fu and Kane, 2007; [36]Shuichi Murakami, 2007). However, its surface states and the mechanism for the band inversion were too complicated. Therefore, in 2009, Zong Fang's group at the Chinese Academy of Sciences and Shou-Cheng Zhang's group in Stanford proposed $(Bi,Sb)_2(Te,Se)_3$ family as 3D TIs, generally referred to as the second generation of 3D TIs ([37]Moore, 2009), except for $Sb_2Se_3$ which was expected to be a trivial insulator ([38]H. Zhang, et al., 2009).

The $(Bi,Sb)_2(Te,Se)_3$ family shares the same rhombohedral crystal structure. Figure 1-19(a) shows the crystal structure of $Bi_2Se_3$ where the $\boldsymbol{t}_1$, $\boldsymbol{t}_2$, and $\boldsymbol{t}_3$ indicate the rhombohedral primitive unit cell. $Bi_2Se_3$ has layered structures with an in-plane hexagonal lattice, and an ABC stacking along the out-of-plane direction as shown in Figure 1-19(b). Each layer consists of a single element, Bi or Se, and Se–Bi–Se–Bi–Se layers repeat, which is known as quintuple layers (QLs, 1 QL is approximately 1 nm thick) indicated in Figure 1-19(a) and (c). Considering the QLs and the ABC stacking, the out-of-plane unit cell is 3 QLs. Table 1-1 shows the in-plane and out-of-plane unit cell lattice vectors of the $(Bi,Sb)_2(Te,Se)_3$ TIs.

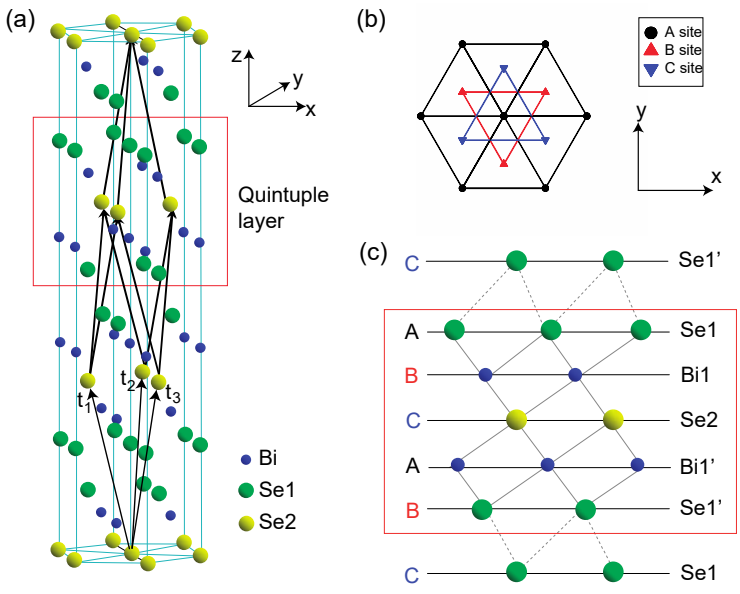


Figure 1-19. Crystal structure of $Bi_2Se_3$. (a) Crystal structure with rhombohedral primitive lattice vectors. (b) Illustration of the stacking order from a top view. (c) QL from a side view. (Adapted from [38]H. Zhang, et al., 2009).

| | | $Bi_2Se_3$ | $Bi_2Te_3$ | $Sb_2Te_3$ |
|---|---|---|---|---|
| Lattice constant | *a* (Å) | 4.138 | 4.383 | 4.250 |
| | *c* (Å) | 28.64 | 30.48 | 30.35 |

Table 1-1. Lattice constants of $Sb_2Te_3$, $Bi_2Te_3$, and $Bi_2Se_3$. (Data taken from [39]Wyckoff, 1964).

In 2009, the characteristic signature of the 3D TIs was observed and investigation of the surface states was performed in $Bi_2Se_3$ ([40]Xia, Qian, Hsieh, Wray, et al., 2009; [41]Hor, et al., 2009; [42]Hsieh, Xia, Qian, Wray, Dil, et al., 2009), $Bi_2Te_3$ ([42]Hsieh, Xia, Qian, Wray, Dil, et al., 2009; [43]Chen, et al., 2009; [44]Hsieh, Xia, Qian, Wray, Meier, et al., 2009; [45]Xia, Qian, Hsieh, Shankar, et

al., 2009), and $Sb_2Te_3$ ([44]Hsieh, Xia, Qian, Wray, Meier, et al., 2009). Figure 1-20 shows the observations of the topological surface bands in $Bi_2Se_3$, $Bi_2Te_3$, and $Sb_2Te_3$ by angle-resolved photoemission spectroscopy (ARPES). Figure 1-21(a–d) shows the helical spin states of the topological surface bands in $Bi_2Se_3$, $Bi_2Te_3$ detected by spin-resolved ARPES ([42]Hsieh, Xia, Qian, Wray, Dil, et al., 2009). The spin helicity leads to WAL effect as mentioned above, which is shown in $Bi_2Se_3$ by the magnetoresistance measurement in Figure 1-21(e).

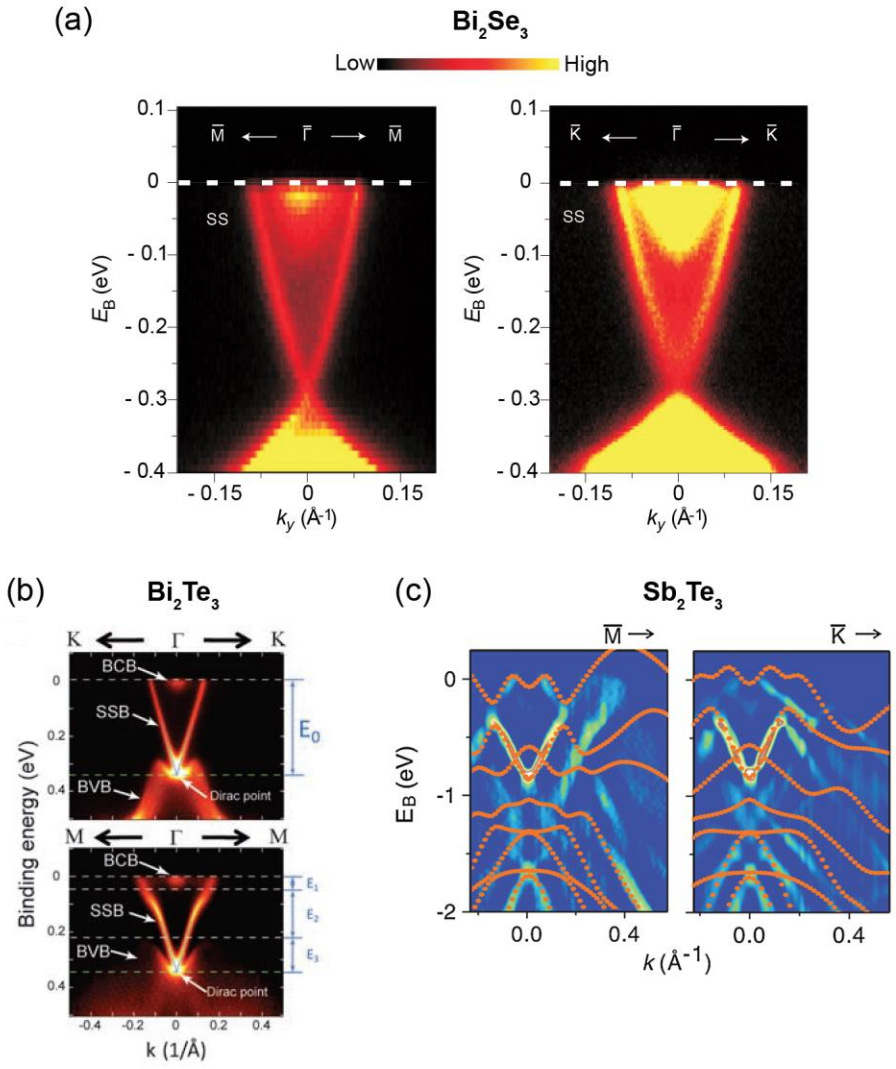


Figure 1-20. Observation of the topological surface bands in (a) $Bi_2Se_3$, (b) $Bi_2Te_3$, and (c) $Sb_2Te_3$ 3D TIs using ARPES. Adapted from (a) Ref. ([40]Xia, Qian, Hsieh, Wray, et al., 2009), (b) Ref. ([43]Chen, et al., 2009), and (c) Ref. ([44]Hsieh, Xia, Qian, Wray, Meier, et al., 2009).

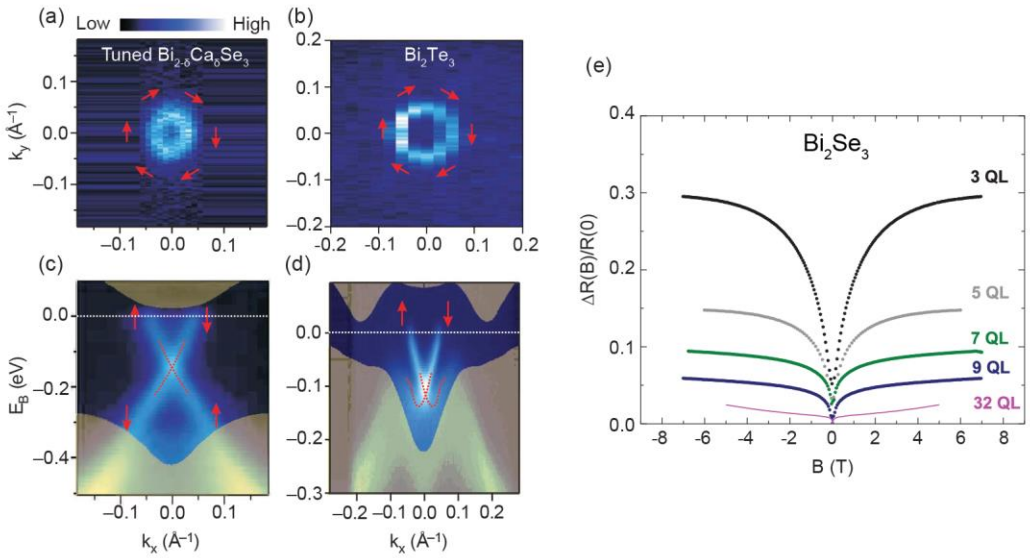


Figure 1-21. Observation of helical spin structure using spin-resolved ARPES and WAL effect. (Adapted from (a) [42]Hsieh, Xia, Qian, Wray, Dil, et al., 2009; (b) [46]Kim, et al., 2011).

## 1.4 The scope of this work

We seek to understand the properties of the surface states of the TI thin films. $Bi_2Se_3$ was predicted to show topological properties even at room temperature due to the largest nontrivial bulk band gap, 0.3 eV, which is larger than the energy scale of room temperature. In reality, however, many parasitic defects cause raising of the Fermi level of $Bi_2Se_3$, screening the effects from the surface states due to the bulk conduction. In this dissertation, we performed charge compensation doping as well as defect engineering to suppress the sheet carrier density ($n_{2D}$) to lower the Fermi level, eventually positioning it at the charge neutrality point (Dirac point) in $Bi_2Se_3$ grown by molecular beam epitaxy (MBE).

In the following two chapters, we will introduce MBE as a thin film growth technique, and DC electric transport as our main film characterization. In the introduction to MBE, we will show

how to grow the $Bi_2Se_3$ thin films (usually thinner than 50 QLs), how to perform the defect engineering and doping in parallel with the fundamentals of MBE. In the following two chapters, we will show and discuss the experimental results. $Bi_2Se_3$, one of the most widely studied TIs, is naturally electron-doped due to n-type native defects, precluding the achievement of p-type $Bi_2Se_3$ thin films: the hole doping problem. We provided a solution to this long-standing problem by suppressing these defects through an interfacial engineering scheme. In addition, we will show the successful implementation of the ferromagnetic anomalous Hall effect, deviation of a linear Hall effect curve due to internal magnetism with a hysteresis loop, in Cr-doped $Bi_2Se_3$ thin films by utilizing a surface-state engineering scheme. We will further explain the emergence of the positive anomalous Hall effect with analyzing the mass-gap susceptibility based on a first-principles method. In the last chapter, we will review the studies in this dissertation.

# CHAPTER 2. THIN FILM GROWTH OF TOPOLOGICAL INSULATORS: MOLECULAR-BEAM EPITAXY

The emergence of low-dimensional systems was the beginning of a new age of semiconductor physics. Such systems are of fundamental importance in modern quantum physics, material science, and quantum chemistry. Low-dimensional physics relies on the technology of precisely controlled heterostructures on the scale of a nanometer, and give rise to exotic quantum phenomena such as the quantum Hall effect (QHE), 2D TIs, Dirac fermions in graphene, and non-Abelian anyons in superconductors. Two Nobel prizes have been awarded for the QHE, one for the discovery of the quantization of the Hall conductivity at integer multiples of $e^2/h$ in 1985 (Klitzing) and another for fractional multiples of $e^2/h$ in 1998 (Laughlin, Stormer, Tsui). The 2DEG formed in a GaAs–$Al_xGa_{1-x}As$ heterostructure acted as an elementary quantum well so that the electrons were confined to a very narrow layer, becoming effectively 2D.

Molecular-beam epitaxy (MBE) lies at the heart of modern 2D physics. It is a great technique for the growth of numerous kinds of thin films. The basic MBE technique was first developed by two American physicists, Chinese-born Alfred Y. Cho and John R. Arthur, Jr. at Bell Laboratories around 1968. Figure 2-1 shows the original MBE patent granted in 1971. After that, the MBE technique has been improved by many other scientists and has become a crucial tool for thin-film studies of various semiconducting materials up to TI films.

In this chapter, our main focus is on growing thin films using MBE and their characterization. We will first give a brief introduction to MBE with its fundamentals and the facilities at Rutgers University. Following this, we will review the basic film growth procedures and how to characterize them. Lastly, we will discuss the particular example of growing the second generation of the 3D strong TI family, which will be the main focus of this thesis.

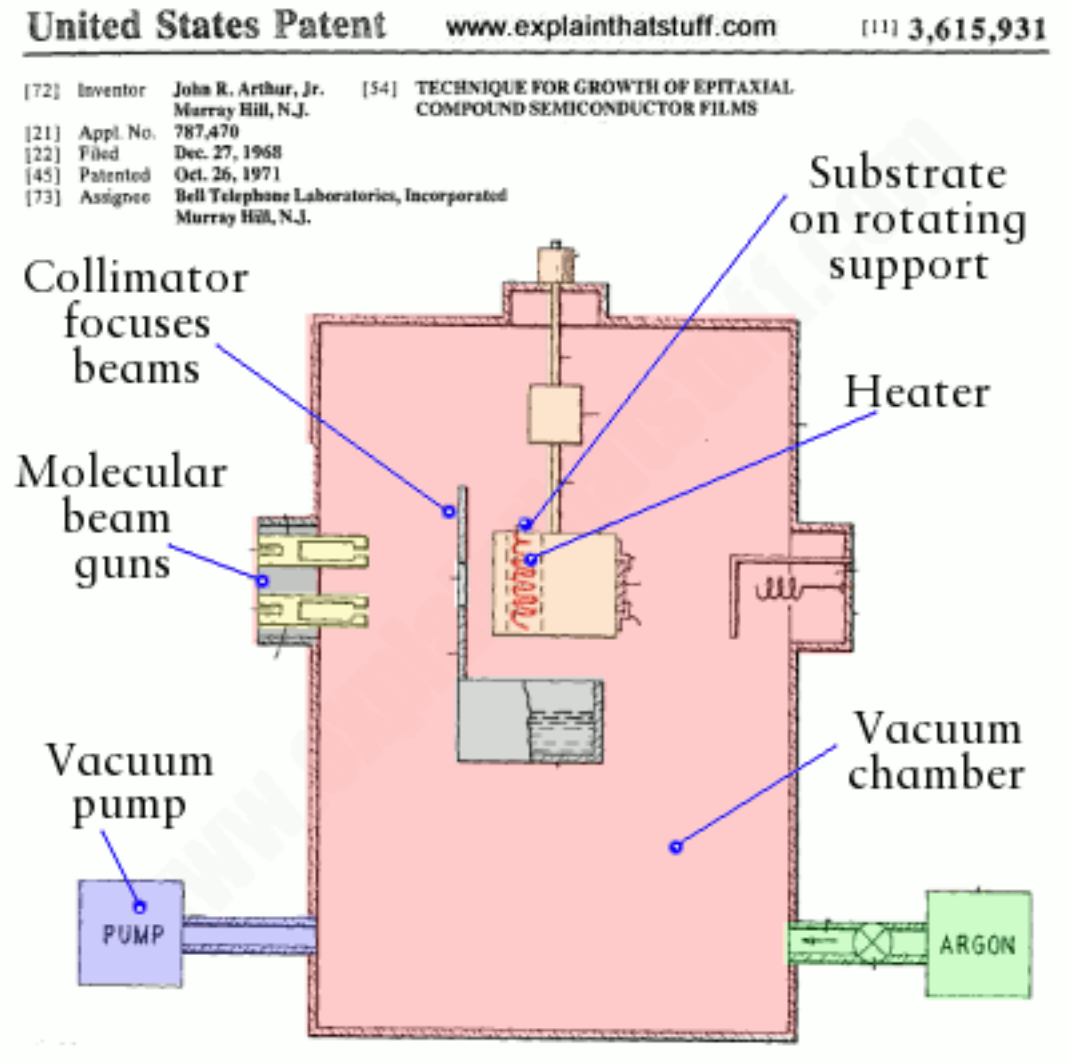


Figure 2-1. A drawing taken from J. R. Arthur, Jr.'s original MBE patent, filed in 1968 and granted in 1971 ([47]Arthur, 1971). (Figure is taken from [48]Woodford, 2018)

## 2.1 Fundamentals of epitaxial thin film growth using MBE

MBE is an atomic scale layer-by-layer crystal (film) growth technique, based on the reaction of thermally evaporated molecular or atomic beams with a heated crystalline substrate. It is sometimes described as an atomic spray due to the similarity between thermal evaporation from a source and particle dispersion from a spray. The MBE is performed in an ultra-high-vacuum (UHV) environment, usually ~$10^{-10}$ Torr. The term *epitaxy* is composed of the Greek words *epi* and *taxis* meaning akin or upon and arrangement or order, respectively. Epitaxy signifies ordered growth of one crystalline layer on another crystalline layer, with the same (or reasonably related) crystal arrangement. Therefore, the surface conditions of a starting crystal (a substrate) and the subsequent few layers are one of the most critical issues in epitaxial crystal growth. Most of the efforts to improve film quality reside in how to reduce the interfacial defects.

### 2.1.1 The necessity for an ultra-high-vacuum environment

MBE is performed in a UHV condition for two main reasons: mean free path and impurity issues. Atom-to-atom scatterings can be reduced in such a high-vacuum environment, which enables line-of-sight evaporation, and less diffusion for the elemental and electron beams by increasing the mean free path of the evaporated sources. The second reason, which is more important than the first one, is to lower defects from the impurities in the thin films. If the background pressure is not low enough, then as the film grows, the residual gas molecules may adsorb onto the film surface, and become incorporated in the film. Such an effect could be fatal depending on the native defect level inside the film.

### 2.1.2 Substrate preparation

For thin film growth using MBE, a substrate is required, and its choice is crucial. In substrate preparation, we first need to clean the related tools such as tweezers, scissors, and a Teflon piece

with acetone and isopropyl alcohol (IPA). Acetone dissolves almost all organic compounds because it is a very polar substance. In addition, it is not only safe (safer than methanol and ethanol) but also water miscible so that it rinses away with water, too. IPA also removes water well, leaving surfaces to dry without spotting. IPA cleaning displaces the residual acetone, which is hard to remove once it dries. Methanol is better than IPA for the cleaning purpose, but we hardly use methanol due to its significant toxicity and flammability.

Substrates were purchased from MTI Corporation (https://www.mtixtl.com/). We usually use one-side polishing for convenience unless there are special reasons such as optical measurements with transmitted light. After tearing off a plastic bag of a substrate, we first blow the surface of the substrate with dry $N_2$ gas. Then, we check the surface using a microscope to exclude poor ones, which usually have cracks or dirty black dots. If the surface is good, we perform ultraviolet ray (UV)–ozone ($O_3$) cleaning of the surface for 5 minutes to remove organic contaminants on the surface.

The UV produced by a low-pressure mercury (Hg) vapor lamp generates two wavelengths: 184.9 nm and 253.7 nm. The UV of wavelength 184.9 nm converts the atmospheric oxygen $O_2$ into $O_3$ by

$$\begin{array}{rcl} O_2 & \rightarrow & O + O \\ O + O_2 & \rightarrow & O_3 \end{array}. \qquad (2\text{-}1)$$

The $O_3$ generated in the process above absorbs the UV of wavelength 253.7 nm, being decomposed. Both the processes of the formation and decomposition of $O_3$ generate highly reactive atomic oxygen O. Most of the organic compounds can also be decomposed by the stronger UV, photolysis, and reaction with the atomic O to form volatile substances such as $H_2O$, $CO_2$, and N. The wavelengths 184.9 nm and 253.7 nm of the UVs can be converted to energies in kJ/mol unit with the formula,

$$E = N\frac{hc}{\lambda}. \qquad (2\text{-}2)$$

$N$ is the Avogadro constant, $c$ is the speed of light, and $\lambda$ is the wavelength. According to Equation (2-2), the wavelengths 184.9 nm and 253.7 nm correspond to 647 kJ/mol and 472 kJ/mol, respectively. The UV–$O_3$ can break the chemical bonds with bond energies below 647 kJ/mol and 472 kJ/mol in Table 2-1.
Table 2-1

| Bond | Bond energy (kJ/mol) | Bond | Bond energy (kJ/mol) |
|---|---|---|---|
| **O–O** | 138.9 | C–F | 441.0 |
| **C–N** | 291.6 | O–H | 462.8 |
| **N–H** | 309.8 | O=O | 490.4 |
| **C–Cl** | 328.4 | H–F | 563.2 |
| **C–C** | 347.7 | C=C | 607.0 |
| **C–O** | 351.5 | C=O | 724.0 |
| **C–H** | 413.4 | C≡N | 791.0 |
| **H–Cl** | 431.8 | C≡C | 828.0 |

Table 2-1. Chemical-bond energy.

### 2.1.3 Principles of molecular-beam epitaxy

MBE is based on kinetic processes such as adsorption, desorption, dissociation, migration, reaction, and incorporation. These features enable us to ensure the best conditions for stoichiometry and epitaxy during the substrate preparation and film growth via real-time in situ monitoring and control. Consequently, MBE is different from other evaporation crystal-growth techniques in the sense of employing atomic or molecular beams in a UHV environment, which allows precise control of composition, growth condition and preservation of high purity, and real-time in situ monitoring although there exist many other types of vacuum evaporation techniques. Furthermore, because the MBE thin film growth is governed by the surface kinetics generally at relatively low substrate

temperatures, material and dopant interdiffusion can be kept to a minimum. Therefore, MBE is able to produce extremely high purity and highly crystalline thin-film heterostructures with precise control over composition, doping, and interfaces in a nanometer range with good lateral uniformity.

Figure 2-2 shows the schematic geometry of MBE and deposition. The MBE growth chamber consists of a substrate stage, thermal evaporation sources, a cryogenic pump, a reflection high-energy electron diffraction (RHEED) system, etc. In growth, a constituent, typically individual, material sources are evaporated and allowed to interact chemically on a heated substrate. The beams usually do not interact with each other in the gas phase because they possess mean free paths much longer than the typical source-to-substrate distance, 20–30 cm, due to the UHV conditions. The use of pure solid-source material allows not only very pure epitaxial growth but also much-simplified chemical reaction when the source material reaches the substrate. MBE is extremely useful to generate very sharp interfaces. The effusion cells that produce the molecular beams of source materials are typically paired with a mechanical pneumatic shutter that can quickly start or stop the beams in much less time than it takes to grow an atomic layer of material. The temperature of the sources should be precisely controlled for very reproducible and stable flux generation from the effusion cells. This makes the controls simple for accurate alloy compositions and doping concentrations. The UHV environment also enables incorporation of various in situ monitoring techniques that can be used during growth, including RHEED, low-energy electron diffraction, and mass spectrometry.

The epitaxial thin film growth involves the condensation process of the molecular beams onto a substrate. The molecules interact with the substrate surface with forces originating either from the van der Waals interaction (physical) or from the formation of chemical bonding (chemical) with those of the atoms of the substrate. Depending on which contribution dominates, they are called *physisorption* (physical adsorption) or *chemisorption* (chemical adsorption). There exists a weak potential well on the surface of a substrate due to attractive van der Waals forces, often modeled by the 6–12 Lennard-Jones potential $U(r) = 4\epsilon((\sigma/r)^{12} - (\sigma/r)^{6})$, where $r$ is the

distance from the surface, $\epsilon$ is the potential well depth, and $\sigma$ is the distance where the potential is zero. If the substrate temperature is too high, then the atoms will be desorbed off the substrate right away even if physisorption occurs. In contrast, the substrate temperature needs to be moderately high so that the atoms that are adsorbed onto the substrate have enough energy to remain mobile, so they can diffuse around and find the optimal place to adsorb chemically with overcoming an activation energy. The process of physisorption to chemisorption usually occurs at a nucleation point, typically a point of stronger confinement, such as a step edge. Chemisorption is a much stronger adsorption process.

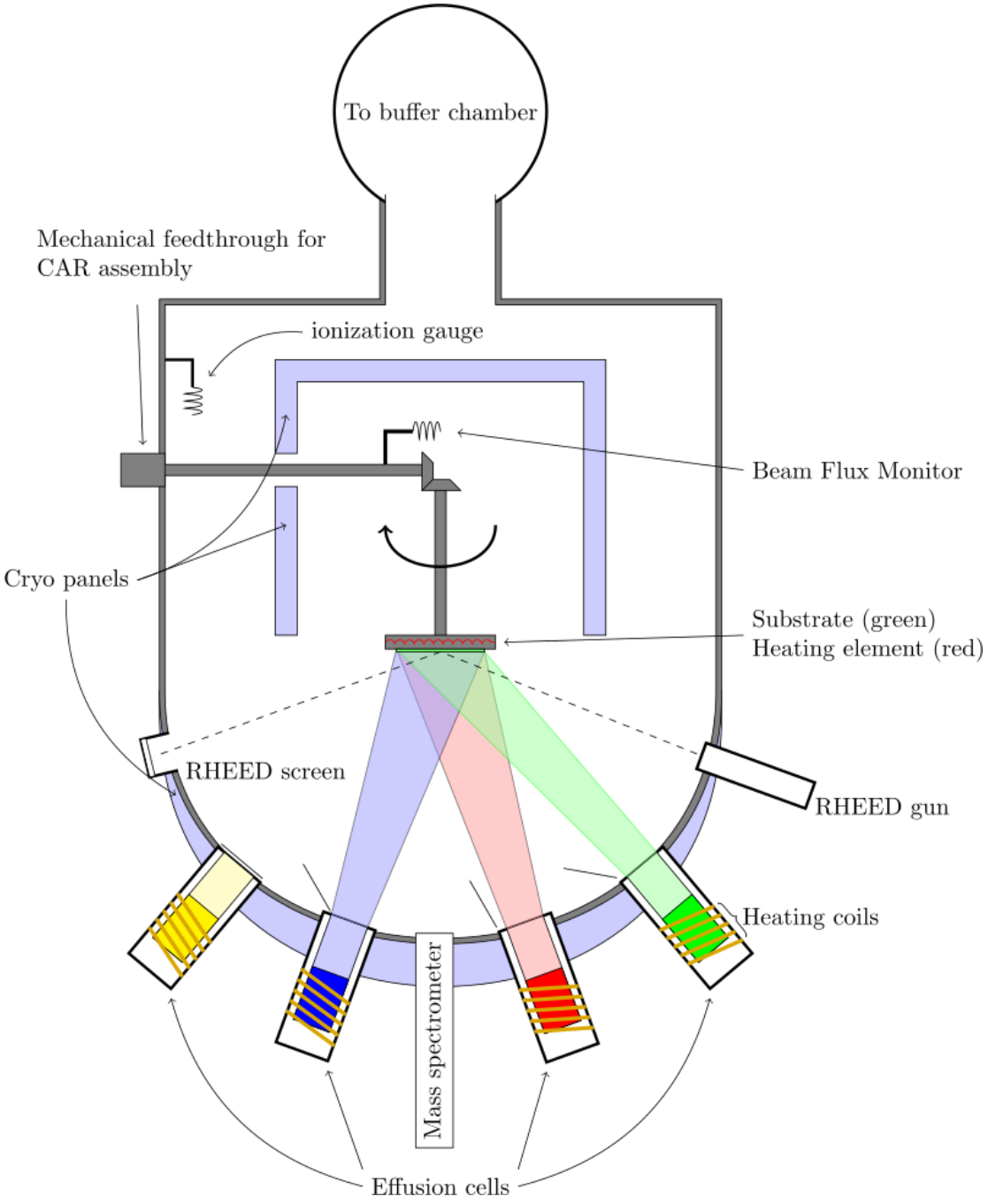


Figure 2-2. A simple illustration of a molecular-beam epitaxy system. (Figure is taken from [49]Wikipedia, n.d.)

## 2.2 In situ atomic flux measurement: Quartz crystal microbalance

One of the great advantages of the thin film growth using MBE is control of the thickness in the atomic layer scale. The thickness of the films is determined by the number of atoms and their chemical compositions. To manipulate the film thickness and chemical compositions, the exact atomic or molecular-beam flux should be in our hands. Therefore, the atomic flux calibration is important in epitaxial thin film growth. We introduce two methods for atomic flux measurement of the individual sources that have been used in our group: quartz crystal microbalance and Rutherford backscattering.

Quartz is the second most abundant mineral in the Earth's continental crust behind feldspar and is composed of Si and O atoms ($SiO_2$) ([50]Anderson and Anderson, 2010). Some types of quartz generate electric potential differences by deformation of their physical body and vice versa. This phenomenon is known as the "piezoelectric" effect or "piezoelectricity." The piezoelectric effect has a wide variety of applications such as clocks, musical instruments, motor actuators, sonar equipment, and scientific measurements. In epitaxial thin film growth, the piezoelectricity is used to detect a mass variation by measuring the change in frequency of a quartz crystal resonator, the quartz crystal microbalance (QCM). When a thermally evaporated element is deposited on the quartz crystal, the capability of sensing a very small mass change can tell us its deposition rate (min/nm or s/Å).

Figure 2-3(a) shows a schematic description of a piece of quartz crystal coated by electrodes. Both sides of the crystal are coated by electrodes. The structure of a quartz crystal is pretty complicated compared with other crystals, and the crystal can be cut in an infinite number of ways. However, there are only a few cuts for particular uses. The most widely used crystal cut is the AT crystal cut, developed in 1934. The plate contains the crystal's *x*-axis and is inclined by 35°15′ from the *z*- (optic) axis. The cut is used for quartz crystal oscillators as well as for other

electronic instruments where oscillators are required to run typically in the range 500 kHz to around 300 MHz.

In 1959, a German physicist, Günter Hans Sauerbrey, first derived an explicit quantitative relationship between the shift of resonant frequency and added mass, which is important to ease of use in a QCM ([51]Sauerbrey, 1959) as

$$\Delta f \approx -C_f \Delta m_f , \tag{2-3}$$

where $C_f$ is a crystal calibration constant which is related to the resonant frequency, density (2.648 g/cm$^3$), and shear modulus (2.947 × 10$^{11}$ g/(cm·s$^2$)) of the AT-cut quartz crystal. From Equation (2-3), the mass addition can be estimated using the change of the resonance frequency, and source fluxes can be obtained through the information.

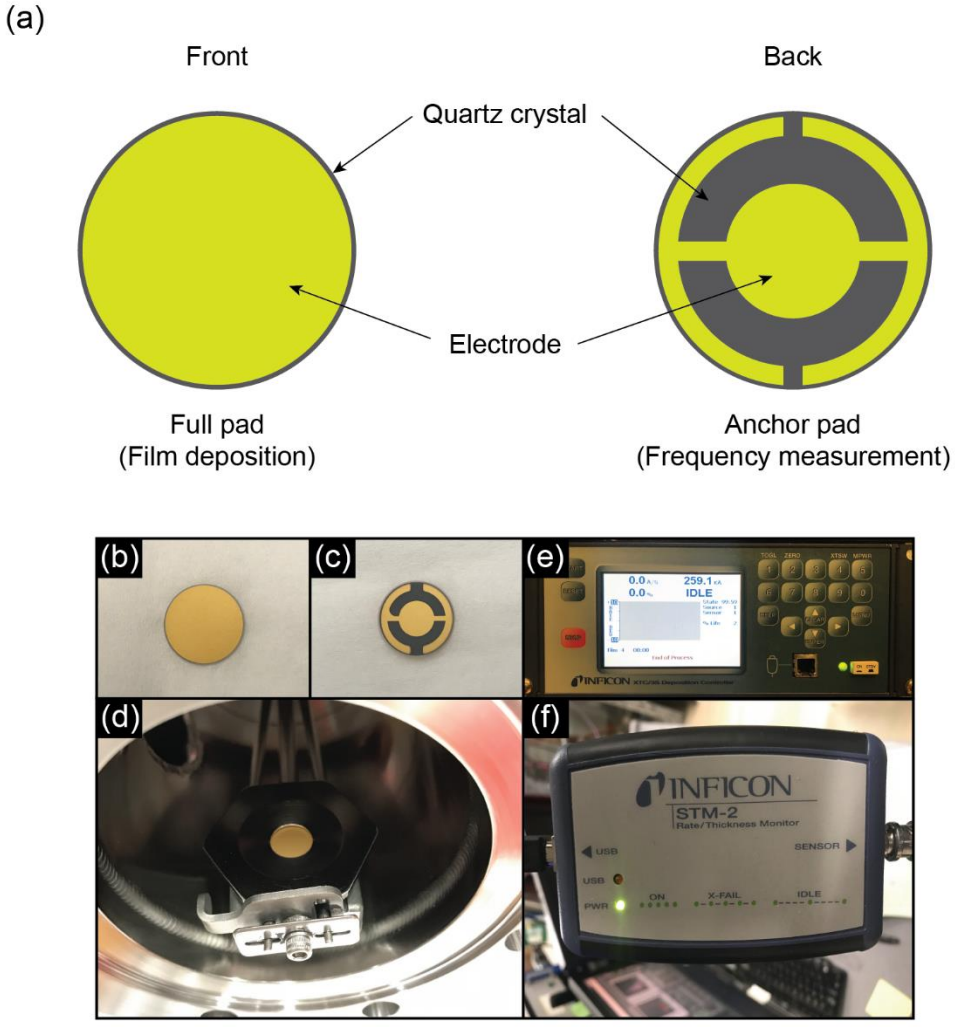


Figure 2-3. Description of a quartz crystal and the QCM equipment.

## 2.3 In situ structural characterization: Reflection high-energy electron diffraction

The single most important technique in regard to MBE technique is in situ RHEED, which enables us to achieve high-quality atomic scale films. With RHEED, one can keep monitoring the crystal structure of the terminating layer of a growing film in real time. This allows many growth trials to

be performed in a relatively short time, in sequence (usually on the same sample), and produces unambiguous details of morphology and film structure. One can pinpoint the optimal growth parameters usually within a few days to a week with RHEED. To obtain similar information as that with RHEED, ex situ structural characterization probes should be used after every single growth trial, which may take much more time.

A thorough discussion of the principles of RHEED is beyond the scope of this dissertation. A more specific and detailed introduction to RHEED can be found in many other books (e.g. [52]Nizzoli, et al., 1985; [53]Ichimiya and Cohen, 2004). In RHEED, an electron beam strikes a single crystal surface of a substrate at a grazing incidence, producing a diffraction pattern on a phosphorescent screen as shown in Figure 2-4. Focused electron beams with energy typically of the order of keV are incident on the surface. Then, the electrons are scattered by the periodically positioned atoms of the surface, which results in its characteristic diffraction pattern on the screen. If electrons are diffracted only by the first flat atomic layer, the 3D reciprocal lattice spots degenerate into parallel infinite rods. Thermal lattice vibrations and imperfections, in reality, cause the reciprocal lattice rods to be broadened, while the Ewald sphere itself also has some nonzero thickness due to divergence and dispersion of the electron beam. Therefore, even diffraction from an atomically flat surface leads to a diffraction pattern consisting of streaks with modulated intensity. If the surface is not flat, many electrons will be transmitted through some islands on the surface and scattered in different directions, resulting in a RHEED pattern being *spotty* (a 3D feature). Therefore, the flatness of a surface is the first important information instantly provided by the RHEED pattern. In the case of an amorphous surface (e.g., an oxide layer on Si surface), it is evident that the diffraction would give no pattern at all, and only a diffuse background would appear.

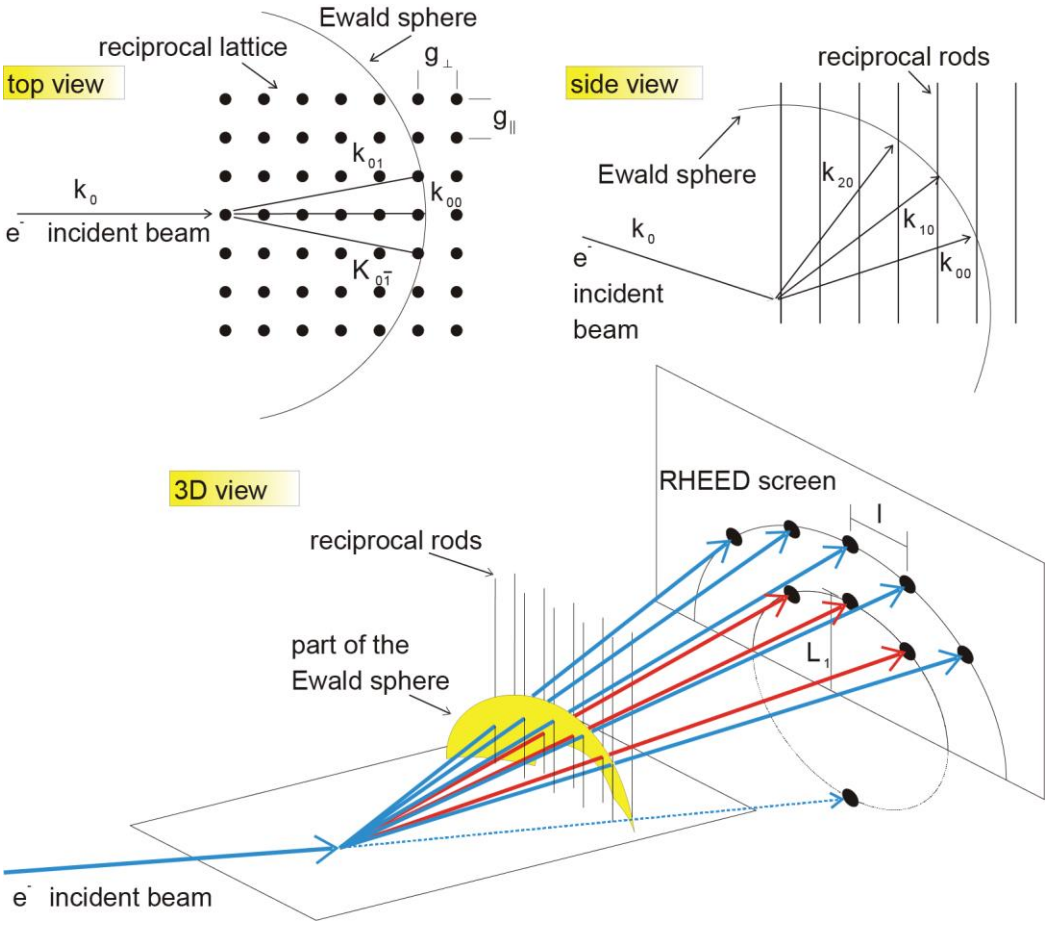


Figure 2-4. Description of electron diffraction on a flat surface. (Redrawn from [54]Klein, 2001)

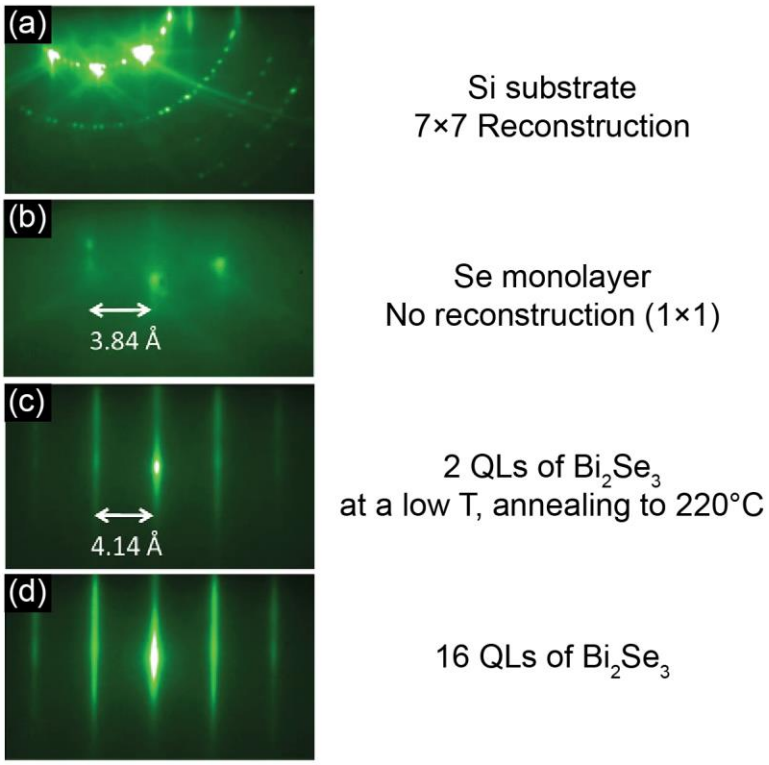


Figure 2-5. Evolution of a RHEED pattern on the surface from Si (111) to the $Bi_2Se_3$ layers. (a) Si (111) 7 × 7 reconstructed surface after ex situ UV–ozone cleaning and in situ thermal cleaning in a UHV chamber. (b) RHEED pattern change after a monolayer of Se. The 7 × 7 reconstruction vanished. The estimated Si (111) 1 × 1 in-plane lattice is 3.84 Å. (c) RHEED pattern change after 2 QLs of $Bi_2Se_3$. The $Bi_2Se_3$ layers were deposited at a low temperature and annealed at 220 °C. The estimated $Bi_2Se_3$ in-plane lattice is 4.14 Å. (d) Brighter and sharper RHEED pattern after further growth of 16 QLs $Bi_2Se_3$ film. (Adapted from [55]Bansal, et al., 2011)

Use of RHEED provides a lot of information on the terminating layer quality of a growing film or a substrate. Figure 2-5, for example, shows the RHEED pattern development in $Bi_2Se_3$ growth on a Si (111) substrate. The substrate initially yields a clean Si (111) as shown in Figure 2-5(a). The bright and sharp pattern with 7 times more streaks indicates a 7 × 7 reconstructed surface. The appearance of the 7 times denser streaks implies that the unit cell was extended by 7

times in real space. The clear diagonal lines are called Kikuchi lines, which are indicative of a high-quality single crystalline growth. After a monolayer deposition of Se, the RHEED pattern shows the Se-terminated 1 × 1 Si surface as in Figure 2-5(b). The denser streaks disappear, and a modified pattern shows up, indicating 1 × 1 Si surface without the reconstruction due to the reaction between Se and Si. Figure 2-5(c) shows the pattern change corresponding to a $Bi_2Se_3$ surface. The smaller spacing of the $Bi_2Se_3$ streaks is shown because the in-plane lattice constant of $Bi_2Se_3$ is 4.14 Å, which is greater than the 3.84 Å of the Si (111) plane, which is identical to the bulk lattice constant of $Bi_2Se_3$. The diffraction pattern becomes sharper on the deposition of more QLs as shown in Figure 2-5(d). It is evident that the film quality improves based on the sharper and brighter RHEED streaks. As the process above shows, RHEED can provide helpful information about surface geometry and chemistry.

## 2.4 Molecular-beam epitaxy at Rutgers University

The MBE group at Rutgers University hosts two custom-built MBE systems (SVTA) with base pressure less than $5 \times 10^{-10}$ Torr. One of them is dedicated to oxide materials growth and the other is usually used for chalcogenide TI films. Figure 2-6 shows the latter MBE facility, showing RHEED, effusion cells, QCM, pneumatic shutters, etc. We will briefly look into the vacuum and evaporation systems which are the most essential components in MBE thin film growth.

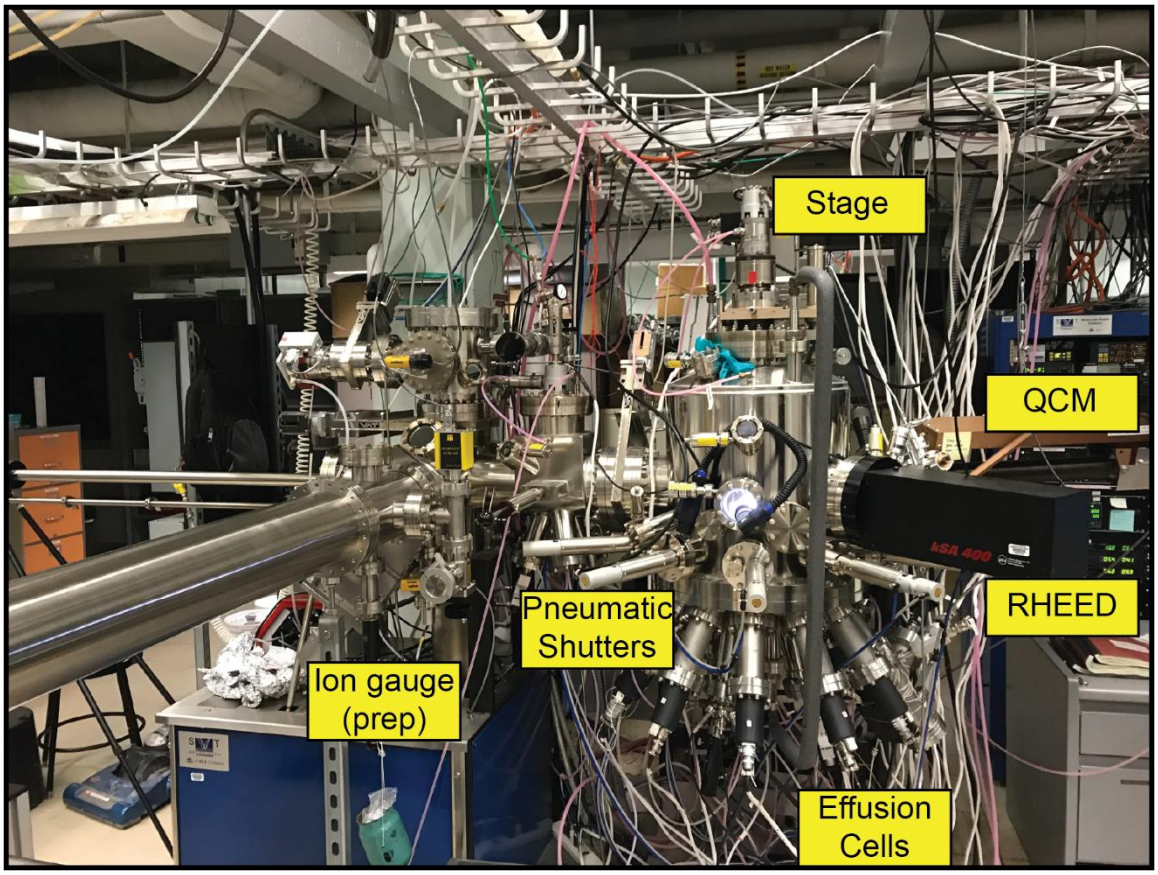


Figure 2-6. Chalcogenide-only MBE facility at Rutgers University.

### 2.4.1 Vacuum system: chambers and pumps

To achieve a UHV environment, three different types of pumps are used: roughing pump, turbopump, and cryopump. A roughing pump is any vacuum pump (typically a scroll pump at Rutgers) used to evacuate a vacuum system initially, as a first stage toward achieving UHV. A roughing pump is supposed to work in the range of atmospheric pressure down to ~mTorr. It would not work efficiently below 1 mTorr, thus it is used to decrease the atmospheric pressure to ~mTorr. A scroll pump is shown in Figure 2-7(a).

Once ~mTorr is achieved with a scroll pump, it needs to be changed to a turbopump, which is capable of produce much higher vacuum. The base pressure of a turbopump usually depends on

the condition of the chamber. In the MBE growth chamber at Rutgers, the usual lowest pressure with a turbopump is ~$10^{-7}$ Torr. If there exist small leaks or KF flange connections, then the pressure might stay around ~$10^{-6}$ Torr, and it may take a bit longer time to get a lower pressure. A turbopump from Pfeiffer Vacuum is shown in Figure 2-7(b).

The last type of pump works a bit differently. It uses cryogenic temperatures to suck and hold particles (a cryopump). This type of pump is usually much stronger than any other mechanical pump. Therefore, when the pressure stays at $10^{-6}$–$10^{-7}$ Torr, a cryopump needs to work by opening the gate valve, which is usually able to produce $10^{-10}$ Torr or even lower. A cryopump is shown in Figure 2-7(c).

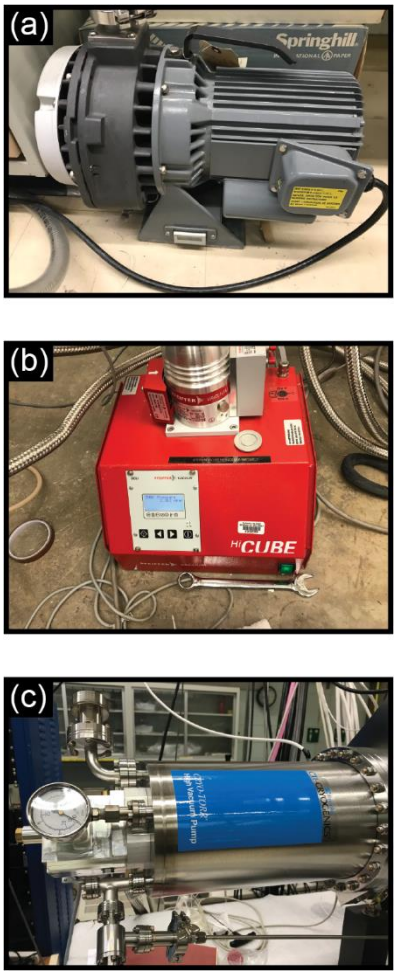


Figure 2-7. Pumps for UHV conditions. (a) A scroll pump (roughing). (b) A turbopump. (c) A cryopump connected to an MBE growth chamber.

### 2.4.2 Evaporation system

In MBE, the most commonly used effusion cell is a Knudson-type effusion cell. It was first developed by Martin Knudsen (1871–1949). A typical Knudsen cell contains a crucible (made of alumina, pyrolytic boron nitride, tungsten, or graphite), heating filaments (often made of the metal tantalum), water cooling system, heat shields, and a shutter. Figure 2-8 shows several thermal effusion cells. A crucible holds a proper amount of a source and is heated by a current across a surrounding coil (Figure 2-8(d)). The temperature is precisely controlled by a proportional integral derivative (PID) controller. Depending on the operating temperatures of the elements, the choice of a cell could be different. There are three types of Knudsen effusion cells with respect to operation temperatures: low-, medium-, and high-temperature cells. The cell for low-temperature operation is shown in Figure 2-8(a). The typical upper limit of low-temperature cells is around 1,000 ℃. The shroud has multiple holes to release heat, which makes it easy to stay at the low temperature. In contrast, a high-temperature cell does not have any holes in the shroud as shown in Figure 2-8(c) and is capable of running relatively high currents to maintain the high temperature. Its upper limit is usually 1,800 ℃. Medium temperature cells can generally work up to 1,400 ℃, and an example is shown in Figure 2-8(b).

In the case that higher reactivity of a source is required in an MBE growth, one can use a cracker cell. In some of selenides' growth, one might need atomic selenium instead of the molecular form. Then, by using a Se cracker cell, one can crack the selenium molecules to achieve higher reactivity of selenium. This is performed by an additional hot zone which is called a cracking tube. Figure 2-8(e) shows a selenium cracker cell that consists of bulk (crucible), valve (in the middle), and tube (relatively thin tube on top). Evaporated selenium molecules passing through the valve experience the very hot zone and get cracked by bouncing off the hot wall. Eventually, atomic selenium flux would be generated.


Figure 2-8. Pictures of thermal effusion cells. (a) Low-, (b) Medium-, (c) High-temperature thermal effusion cells. (d) Inside coil of an effusion cell. (e) Se cracker cell.

When refractory metals such as niobium, tungsten, and tantalum need to be evaporated as a source, another type of effusion equipment is required because their proper operating temperatures are far higher than the limit of the high-temperature cells (~1,800 ℃). The materials need to be heated to 2,000–2,400 ℃ or higher to generate a reasonably high flux. The Knudsen-type thermal effusion cells cannot evaporate those materials, and another kind of evaporation technique is needed: electron-beam (E-beam) evaporator. Figure 2-9(a) shows a schematic illustration of the principles of E-beam evaporators. A source rod, typically one of the refractory

metals, is located at the center, and a round tungsten–rhenium filament is positioned above the top of the rod as shown in Figure 2-9(a). A high bias voltage is applied across the rod and the filament, and the filament starts to be heated by applying a current. Typically, proper operation requires 6–7 amps or above. Then, by thermionic effect, the filament releases electrons, which are rapidly accelerated toward the top of the rod, bombarding the surface and consequently heating the top part of the rod. In this way, the source rod can be heated to a much higher temperature above 2,000 ℃. Figure 2-9(b) shows the inside of an E-beam evaporator.

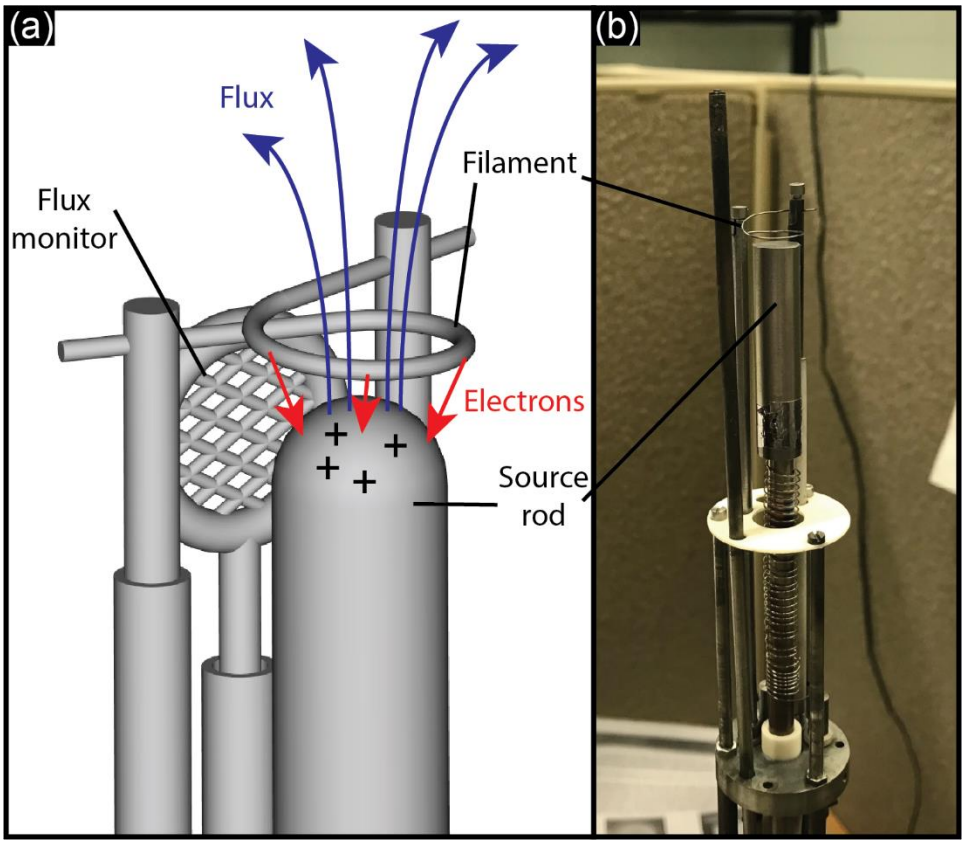


Figure 2-9. (a) A schematic description and (b) an image of an electron-beam evaporator.

## 2.5 Epitaxial growth of $(Bi,Sb)_2(Te,Se)_3$ thin films

$Bi_2Se_3$ is one of the most widely studied 3D TIs because it has relatively large bulk band gap, ~0.3 eV, roughly equivalent to 3,500 K, among the second generation of 3D TI family ([38]H. Zhang, et al., 2009; [42]Hsieh, Xia, Qian, Wray, Dil, et al., 2009; [40]Xia, Qian, Hsieh, Wray, et al., 2009). It was expected that the Fermi level would be easily tuned into the bulk band gap, but it turned out to be not completely true. In reality, $Bi_2Se_3$ suffers from significant Se vacancies that release electrons, making it electron-doped. Moreover, the vacancies have high chances to get oxygen atoms easily, which introduces more disorder, thereby more electrons are produced in the system. Almost all defects in $Bi_2Se_3$ are known to act as electron dopants ([56]West, et al., 2012). The increased number of electrons pushes up the Fermi level even into the bulk conduction band. This is the major reason for the parasitic nontopological bulk contribution to electrical charge transport, which needs to be addressed for high-quality films.

### 2.5.1 Consideration of structural defects in $(Bi,Sb)_2(Te,Se)_3$ films

Although the topological surface state is robust due to the topological nature, therefore it can survive even in defective films, TI films are also prone to a variety of structural defects such as stacking faults, antiphase domain boundaries (APBs), mosaicity-tilt, mosaicity-twist, and twin defects ([57]Tarakina, et al., 2014; [58]Kampmeier, et al., 2015; [59]Richardella, et al., 2010; [60]Schreyeck, et al., 2013). The defects generally negatively affect the electrical transport properties, which are sensitive to structural defects. TI film quality is typically indicated by sheet carrier density ($n_{2D}$) and mobility ($\mu$). High-quality TI films should have a low $n_{2D}$ and a high $\mu$ for the electrons in the surface states because of the topological nature of the emergent Dirac bands. Typically, $n_{2D}$s have a tendency to be determined by point defects such as vacancies and antisite defects. On the other hand, mobility is affected by both point defects and line or planar defects. Several kinds of structural defects will be briefly introduced in detail below.

Stacking faults can occur in the TI materials easily due to the in-plane threefold symmetry as shown in Figure 1-19. Three possible orientations for a TI domain labeled with A, B, and C are shown in Figure 2-10(b). A flawless stacking sequence would be ⋯ ABCABCABC ⋯, with the following QL rotated 120° from the previous QL as in Figure 2-10(a). A stacking fault occurs when a discontinuity is present in the sequence such as a missing single QL, leading to a sequence of e.g., ABABCABC, or an additional single QL, leading to a sequence of e.g., ABBCABCABC, as shown schematically in Figure 2-10(c) and (d). Stacking faults may cause serious effects in the electrical properties of the film, including forming topologically protected states along the fault or shifting the Dirac point with respect to the pristine band structure ([61]Seixas, et al., 2013). It is generally difficult to avoid these types of defects.

When two domains with different stacking sequences meet, another kind of defect occurs, twin defects. Twin defects appear over a much larger area than stacking faults. A change in stacking in the vertical direction leads to a so-called lamellar twin, while a different stacking in the same plane leads to a rotational twin. Rotational twin defects emerge as oppositely oriented triangular domains, which can be found by atomic force microscopy (AFM) scans. Both types of twin defects can be visualized using transmission electron microscopy (TEM) ([62]Wang, et al., 2011; [63]Tarakina, et al., 2012; [57]2014) as shown in Figure 2-11. In general, the higher the structural quality of a film, the larger the domains, thus there are fewer triangular domains, which is correlated to a higher mobility. The domain size can become larger by growing the films on a well-lattice-matched substrate or optimizing growth conditions.

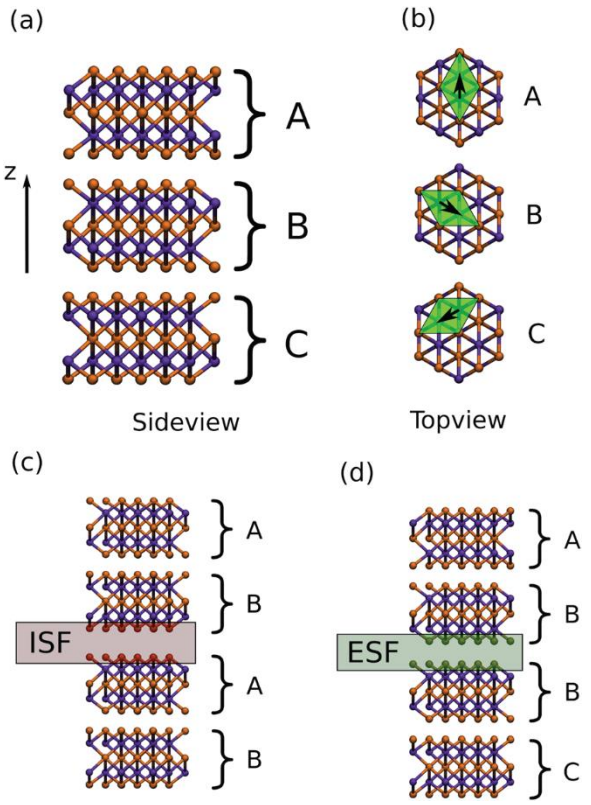


Figure 2-10. Atomic structures and stacking faults of $Bi_2Se_3$ and $Bi_2Te_3$. (a) Side view of three different QLs consecutive stacking along the (0001) direction. (b) Top view of each QL of A, B, and C. The green areas and black arrows show the relative orientations among the QLs. Examples of stacking fault models, (c) intrinsic stacking fault, and (d) extrinsic stacking fault. (Adapted from [61]Seixas, et al., 2013)

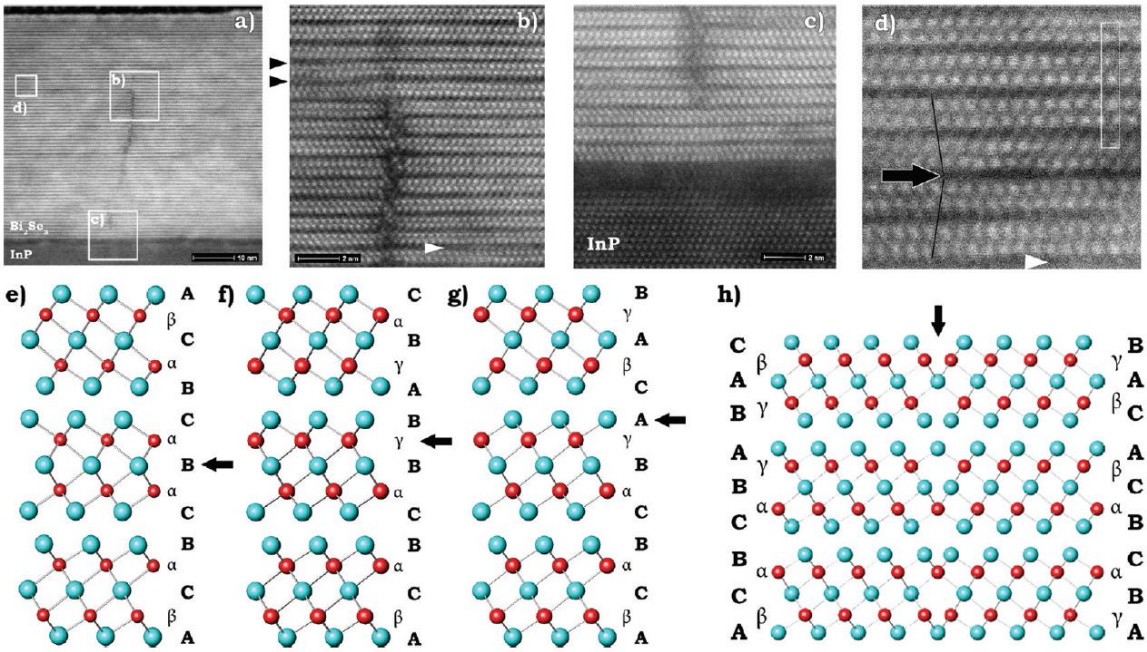


Figure 2-11. HAADF-STEM cross-sectional image of $Bi_2Se_3$ grown on an InP (111) substrate: (a) overview image, (b) rotation twin boundary enlarged from the middle part of the film. Arrows indicate the presence of dislocations. (c) Twin boundary enlarged from the interface region, (d) lamellar twin boundary enlarged from the middle part of the film. White borders indicate unit cell of $Bi_2Se_3$. (e–g) Structural models for the lamellar twin with twin boundaries at the position of (e) Se(1), (f) Bi, and (g) Se(2) atoms. The boundaries are marked by arrows. (h) A structural model for the rotation twin boundary. Bi and Se atoms are represented by red and blue spheres, respectively. (Adapted from [63]Tarakina, et al., 2012)

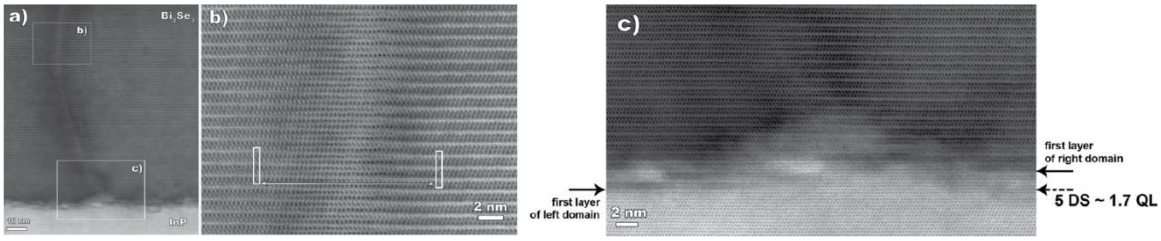


Figure 2-12. Side view of STEM images of an antiphase domain boundary in a $Bi_2Se_3$ film grown on a rough InP(111)B substrate: (a) overview bright field-STEM image, (b) HAADF-STEM image of the upper part of the antiphase domain boundary indicated in (a), (c) enlargement of image (a) at the interface region. (Adapted from [57]Tarakina, et al., 2014)

The difference in unit cell height between the substrate and the TI film gives rise to the formation of antiphase domains. On the surfaces of substrates, there exist large and flat step terraces with the step heights equal to the out-of-plane lattice of the materials. TI film domains may start to nucleate on each terrace, and expand as the growth continues. When the two adjacent domains meet, an antiphase domain boundary will emerge due to the out-of-plane lattice difference between the TI film and the substrate. In other words, a vertical lattice mismatch between the two domains which started from two different adjacent steps of the substrate. Figure 2-12 shows STEM images of a $Bi_2Se_3$ film grown on a rough InP(111)B substrate. In Figure 2-12(c), it is clearly shown that the left and the right side are different, causing an antiphase domain boundary shown in Figure 2-12(a) and (b). This type of defect negatively influences the electrical properties of the film ([57]Tarakina, et al., 2014; [64]Borisova, et al., 2012) and is hard to remove. Isostructural substrates are necessary to inhibit the defects.

Lastly, when the film nucleates in many small domains even if they are on the same step terrace, mosaicity-twist and mosaicity-tilt can both occur. The domains are sometimes slightly rotated with respect to one another in the same plane as the film: mosaicity-twist. If the domains are slightly misaligned in the out-of-plane direction, that is called mosaicity-tilt. The degree of mosaicity can be evaluated by X-ray diffraction studies. For $Bi_2Se_3$ films, mosaicity is generally low and does not have a strong effect on the film transport properties, though the roughness of the substrate can increase this effect ([57]Tarakina, et al., 2014; [60]Schreyeck, et al., 2013).

Structural defects in TI films including those mentioned above, in general, can have significantly negative effects on the transport properties. Although the topological surface states will still exist even in a defective film, the mobility of those states may be lower than that in a perfect film and the topologically protected states may be more difficult to distinguish from trivial states. In the following sections, we will discuss growth techniques for reducing structural defects.

### 2.5.2 Substrate selection

The ideal substrate is the same material as the film that will be grown. However, commercially available substrates of different materials are generally used due to realistic limits such as a lack of the substrates or difficulty in thickness control. Sapphire substrates are more advantageous than others thanks to their relatively low cost, easy availability, high surface quality, stability at relatively high temperature, and chemical inertness. One of the drawbacks to using sapphire substrates is large lattice mismatch between sapphire and TIs (14.9% for $Bi_2Se_3$) as shown in Table 2-2. It can lead to a variety of structural defects discussed above. People have been growing $(Bi,Sb)_2(Te,Se)_3$, the second generation family of the 3D TIs, thin films on a variety of commercially available substrates such as Si (111), c-plane (0001) sapphire ($Al_2O_3$), $SrTiO_3$ (111), InP (111), SiC (0001), and GaAs. The lattice constants for selected substrates are shown in Table 2-2.

Using many of the more closely lattice-matched substrates is not all it is cracked up to be due to the presence of dangling bonds and surface oxide layers. We have access to the bare surface of the high-quality substrate only after in situ cleaning, but problems may arise during the cleaning process in some cases. For example, InP (111) is closely lattice-matched to $Bi_2Se_3$, about 0.2% mismatch as shown in Table 2-2. However, a surface oxide layer always exists on an InP substrate in air. The oxide layer is usually thermally desorbed at a relatively high temperature. The problem is that phosphorus would be outgassing from the sample at this high temperature, which should be compensated to preserve the high-quality surface of the substrate. Supplying a phosphorus flux could be a good solution to the problem, but it is pretty difficult in a chalcogenide-only chamber unlike in a traditional III/V chamber. As an alternative, the chalcogenide atoms can be supplied in excess when desorbing surface oxides from III/V and other substrates ([65]Guo, et al., 2013). In addition to the surface oxides, many of the available substrates have surface dangling bonds which degrade the substrate surfaces. For those cases, some success has been reported such as passivating these surfaces by a chalcogenide overpressure ([66]Haazen, et al., 2012; [55]Bansal, et al., 2011;

[64]Borisova, et al., 2012) or by an initial monolayer deposition of bismuth ([62]Wang, et al., 2011). These growth demands, as well as the relatively high price of many lattice-matched substrates (~2 times for $SrTiO_3$, ~5 times more expensive for SiC substrates than sapphire), is why most of the TI film are grown on sapphire substrates.

| Substrates | In-plane lattice constant (Å) | Mismatch with $Bi_2Se_3$ (%) |
|---|---|---|
| Graphene | 2.46 | –40.6 |
| SiC | 3.07 | –25.8 |
| GaN | 3.19 | –22.9 |
| Si | 3.84 | –7.2 |
| GaAs | 4.00 | –3.4 |
| α-$In_2Se_3$ | 4.03 | –2.7 |
| InP | 4.15 | 0.2 |
| InAs | 4.28 | 3.4 |
| $Al_2O_3$ | 4.76 | 14.9 |
| $SrTiO_3$ | 5.52 | 33.3 |

Table 2-2. Hexagonal in-plane lattice constants and mismatch of various substrates for $Bi_2Se_3$ films. The mismatch is calculated by (lattice constant – 4.14)/4.14 × 100 (%). The hexagonal in-plane lattice constant of $Bi_2Se_3$ is 4.14 Å.

Recently, buffer layer engineering schemes were reported as excellent artificial substrates for $Bi_2Se_3$ film growth. $In_2Se_3$ on Si (111) substrate was reported as the most suitable substrate for $Bi_2Se_3$ ([67]Rathi, et al., 2014). α-$In_2Se_3$ has the same layered crystal structure and similar lattice constant to the TIs as shown in Table 2-3. The QL spacing of α-$In_2Se_3$ is almost the same as that of $Bi_2Se_3$, minimizing additional structural incompleteness. Therefore, utilizing α-$In_2Se_3$ as a buffer layer could enhance the crystal quality of $Bi_2Se_3$ films. Moreover, because $In_2Se_3$ is a trivial band insulator, it does not contribute to electrical conduction. The MBE growth parameters of $In_2Se_3$ on

Si (111) substrate can be optimized through a three-step growth sequence (See Reference ([67]Rathi, et al., 2014) for details). One year later, Koirala *et al*. reported that using $(In_{0.5}Bi_{0.5})_2Se_3$ as a buffer layer for $Bi_2Se_3$ produced a defect-free interface and led to a record high surface mobility, exceeding 16,000 $cm^2/(V{\cdot}s)$ ([68]Koirala, et al., 2015). They realized that $Bi_2Se_3$ films directly grown on $In_2Se_3$ usually suffer from In diffusion into the $Bi_2Se_3$ layer. Therefore, they inserted 20 QLs of insulating $(In_{0.5}Bi_{0.5})_2Se_3$ layer, protecting the $Bi_2Se_3$ layer from the In diffusion problem and providing even better lattice matching. The growth process will be introduced in Section 2.5.5, and see Reference ([68]Koirala, et al., 2015) for full details. These results imply that substrate choice and preparation are crucial for high-quality MBE growth of TIs.

| material | *a* (Å) | *c* (Å) | crystal structure | QL spacing (Å) |
|---|---|---|---|---|
| α-$In_2Se_3$ | 4.03 | 19.2 | hexagonal | 9.6 |
| $Bi_2Se_3$ | 4.14 | 28.6 | hexagonal | 9.5 |

Table 2-3. Crystal structure parameters for α-phase (hexagonal layer) of $In_2Se_3$ and $Bi_2Se_3$. Adapted from Ref. ([67]Rathi, et al., 2014).

### 2.5.3 In situ thermal cleaning of substrates

In substrate preparation, after the UV–$O_3$ cleaning, we mount the substrates on the molybdenum (Mo) or Inconel plates and put them in the vacuum chamber. About a few tens of minutes after pumping down, we move a new substrate to the growth stage in the main growth chamber using the linear motion controller and magnetic transfer arm.

Then, the substrate is in situ thermally cleaned before we start initial deposition on the substrate. This is to remove further organic contaminants and fully outgas the surface of the substrate. In the case of sapphire substrates, the substrate is heated to 750 °C by ramping at up to

35 ℃/min under an $O_2$ environment with a pressure of $10^{-6}$ Torr. The high temperature is maintained for about 20 min, then we cool it to the growth temperature without the $O_2$. STO substrates are heated to 600 ℃, lower than 750 ℃ because they easily lose oxygen atoms at high temperatures. The oxygen vacancies make the STO substrates conducting, which is inappropriate in typical transport measurements. For that reason, we keep the $O_2$ environment all the time with a pressure of $2 \times 10^{-6}$ Torr above 200 ℃ in the in situ cleaning process.

The cleaning process for Si (111) substrates is somewhat different from those for sapphire and STO substrates. As for Si (111) substrates, a preliminary outgassing step should be preceded with an extra substrate prior to the actual cleaning process. The growth stage with an extra substrate, usually a poor substrate that is not used for epitaxial growth, should be outgassed around 900 ℃ for 30 minutes to desorb almost all of the possible residual Se or other contaminants. The reason for the outgas temperature 900 ℃ will be discussed later. Si substrates always have amorphous $SiO_2$ layers on top of the surfaces. Some Si substrates have ~10 nm – 5 μm or more of the oxide layers by intentional (wet or dry oxidation) process while the others are coated by ~1–2 nm of the thin native oxide layers by air exposure ([69]Raider, et al., 1975). The amorphousness of the $SiO_2$ layers is indicated by the lack of RHEED pattern. To remove the oxide layer, the substrate needs to be outgassed up to ~830 ℃, which usually varies from substrate to substrate. As the $SiO_2$ layer evaporates away, the RHEED pattern of Si (111) would appear. Because the surface of Si (111) is highly reactive, one must cool it once the streaks can be seen. This is why the prior outgassing step should be preceded at 900 ℃ as mentioned above. We minimize the possibility of any contaminants coming out of the stage at around 830 ℃. On cooling the substrate, 7 × 7 reconstruction in real space would occur on a clean enough Si (111) surface ([70]Binnig, et al., 1983), which would be shown as 7 times smaller spacing of the RHEED streaks. The surface cleanliness is indicated by the modified RHEED patterns. If a Si substrate fails to reconstruct, it must be abandoned because the Si (111) surface is very susceptible to contaminants, therefore, it cannot reconstruct in the presence of even a monolayer of contaminants.

### 2.5.4 $Bi_2Se_3$ growth on Si and $Al_2O_3$: the basic recipe

In the growth of $Bi_2Se_3$ on Si (111), a concern after the in situ cleaning is the presence of dangling bonds on the surface of the Si substrate, which function as active sites for adsorption of contaminants ([71]Ishizaka and Shiraki, 1986), and the high reactivity of the silicon surface, which is likely to form second phases such as $SiSe_2$ at high temperatures, leading to a rough interface ([72]Song, et al., 2010; [73]Li, et al., 2010). To terminate the dangling bonds chemically at the Si surface for better epitaxial growth, deposition of Bi onto the surface followed by annealing to form β-phase $\sqrt{3}\times\sqrt{3}$ Bi surface was reported as a buffer layer solution ([74]G. Zhang, et al., 2009). After that, other groups have also used this technique to grow $Bi_2Se_3$ films on Si ([73]Li, et al., 2010; [75]Hirahara, et al., 2010; [76]Sakamoto, et al., 2010). Another effort has been made with deposition of an initial thin seed layer of $Bi_2Se_3$ at a cryogenic temperature followed by further high-temperature growth, but this caused the formation of a few nm-thick amorphous film at the interface and twinned domains ([73]Li, et al., 2010). Suppression of the surface effect is the main purpose of the growth process below.

Inspired by the report that Se atoms can passivate the surface dangling bonds on GaAs ([77]Koma, 1992), we exposed the Si substrate to Se flux for a few seconds prior to the growth to generate the unreconstructed Si (111) surface at low temperature, ~110 °C, which prevents the development of $SiSe_2$ phases as well as an amorphous selenium layer. The next step is to grow a few layers, ~2 QLs, of $Bi_2Se_3$ at a comparatively low temperature as well. After that, we anneal it to 220 °C, which shows a sharp and streaky pattern as shown in Figure 2-5(c). It is followed by the rest of the QLs of $Bi_2Se_3$ deposition. In this way, we can obtain a highly crystalline, second-phase-free, and atomically sharp interface between $Bi_2Se_3$ and Si substrate, as verified by RHEED (Figure 2-5), TEM, and scanning tunneling microscopy (STM) as shown in Figure 2-13.

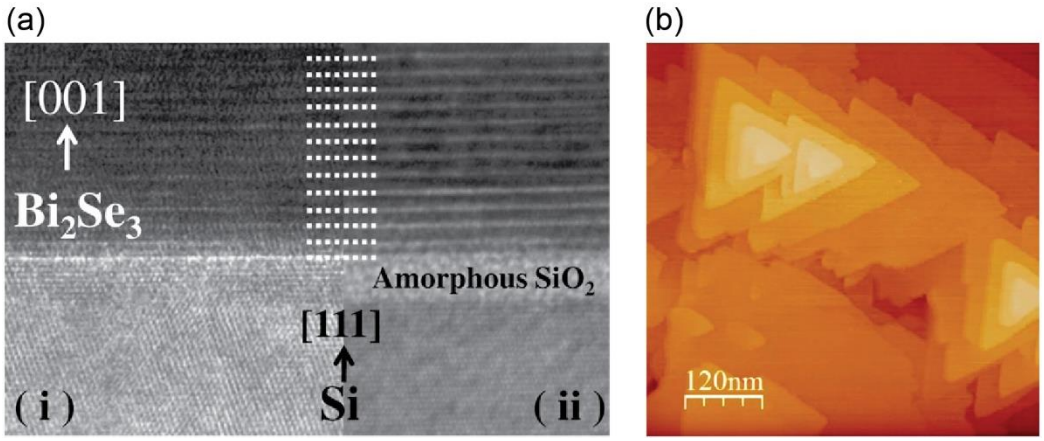


Figure 2-13. Structural characterization of $Bi_2Se_3$ films grown on Si (111) substrates. (a) TEM cross-sectional images exhibiting (i) the sharp interface between the $Bi_2Se_3$ film and the Si (111) substrate after the two-step growth scheme with a 300 nm-thick Se-capping. (ii) TEM cross section of a $Bi_2Se_3$ film kept in ambient condition for weeks without a capping layer. Oxygen diffused through the grown film, forming an amorphous layer of silicon dioxide at the interface. (b) STM image of a 100 QL sample grown on Si (111) substrate. The triangular terraces are indicative of the threefold symmetry of the $Bi_2Se_3$ (111) plane. (Adapted from [55]Bansal, et al., 2011)

High-quality $Bi_2Se_3$ thin films are grown on sapphire substrates via a similar two-step growth method. Although a sapphire substrate ($Al_2O_3$) has a much larger in-plane lattice constant, ~4.785 Å, than Si (111), having a very large lattice mismatch of ~15% with $Bi_2Se_3$ as shown in Table 2-2, sapphire is far more chemically inert than Si (111) due to the strong bonding between Al and O. The growth process is almost the same as $Bi_2Se_3$ growth on Si (111), but the rationale for using the method is completely different. As discussed previously, utilizing the two-step growth procedure was to avoid surface reaction and subsequent second-phase formation on Si (111). In contrast, the $Bi_2Se_3$ growth on sapphire does not have such issues due to the chemical inertness of sapphire, but still, the two-temperature growth is necessary to achieve high-quality $Bi_2Se_3$ films. If one grows a $Bi_2Se_3$ film on a sapphire substrate with the low-temperature growth step, achieving the initial heteroepitaxial layer on the sapphire substrate is difficult because Bi or Se alone does not stick to the substrate above ~190 °C. It is only when both Se and Bi are codeposited onto the

substrate that chemisorption is triggered. Furthermore, even if one tries to deposit Bi and Se together to form $Bi_2Se_3$ at a high temperature, ~220 °C, the coverage will be disordered and the thickness will not easily be controlled during the first few layers. For the aforementioned reasons, to achieve heteroepitaxy at a lower temperature, one needs to use a similar two-temperature-growth scheme to achieve good coverage at low temperature, and anneal it to the higher temperature to improve crystalline quality as the subsequent layers are deposited. As a result of the growth of $Bi_2Se_3$ on sapphire substrates with the two-temperature scheme, the *thickness-independent* carrier density was observed in $Bi_2Se_3$ grown directly on sapphire ([78]Bansal, et al., 2012), thenceforth we have been growing $Bi_2Se_3$ on sapphire substrates with the two-step scheme.

### 2.5.5 $(Bi_{0.5}In_{0.5})_2Se_3$ buffer layer growth

As reported in 2015 ([68]Koirala, et al., 2015), most of the native defects responsible for the high level of n-type carrier densities in $Bi_2Se_3$ thin films originate from the interface with commercially available substrates due to chemical and structural mismatch. This leads to a high density of n-type carriers and prevents $Bi_2Se_3$ thin films from being hole-doped ([46]Kim, et al., 2011). Therefore, we employ $In_2Se_3$ as a buffer layer that works as an excellent substrate for $Bi_2Se_3$ thin films, sharing a chemical similarity and the same crystal structure ([67]Rathi, et al., 2014). However, $In_2Se_3$ has multiple phases unlike $Bi_2Se_3$ and grows on $Al_2O_3$ in a disordered form, which needs to be overcome, and we developed the $(Bi_{0.5}In_{0.5})_2Se_3$ (in short BIS) buffer layer (BIS-BL) scheme. Full details of the growth can be found in Ref. ([68]Koirala, et al., 2015).

Figure 2-14 shows the growth process to address the problem above, we grow a seed layer of 3 QL $Bi_2Se_3$ on $Al_2O_3$ substrate at 135 ℃ before growing $In_2Se_3$: for all subsequent layers, our typical growth rate is ~1 QL/min. The seed layer serves as a substrate for $In_2Se_3$, and it is followed by 20 QL of $In_2Se_3$ deposition at 300 ℃. Then, we anneal it at 600 ℃, which forces the $Bi_2Se_3$ layer to diffuse into the $In_2Se_3$ layer and eventually vaporize out. As the last step in the buffer layer

growth, 20 QL $(Bi_{0.5}In_{0.5})_2Se_3$ are deposited on the highly crystalline $In_2Se_3$ layer at 275 ℃. This 50% BIS layer provides $Bi_2Se_3$ not only with less lattice mismatch, ~1.6%, than the $In_2Se_3$ layer (~3.3%) but also with suppression of In diffusion into the $Bi_2Se_3$ film on top. Now, we grow $Bi_2Se_3$ film as the active TI layers on the BIS at 275 ℃, then an atomically sharp and defect-free interface between $Bi_2Se_3$ and the BIS can be obtained. Utilizing the properly designed BIS-BL, we were able to eliminate most of these interfacial defects. The surface Fermi levels of these films were so low that they revealed a series of—previously inaccessible—topological quantum effects such as QHE ([68]Koirala, et al., 2015), quantized Faraday/Kerr rotation ([79]Wu, et al., 2016), and quantum size effect during topological phase transitions ([80]Salehi, et al., 2016). The significantly reduced defect density in these films can be seen in the Hall resistance data in Ref. ([81]Moon, et al., 2018): an 8 QL $Bi_2Se_3$ thin film directly grown on $Al_2O_3$ (0001) shows an n-type sheet carrier density of $2.5 \times 10^{13}$ /cm$^2$, whereas a similar film on the BIS-BL exhibits only $1.0 \times 10^{12}$ /cm$^2$, 1/25 of the former value.

$Bi_2Se_3$ films grown on BIS-BL exhibit much higher crystalline quality than those on commercial substrates. This is shown by RHEED patterns and (scanning) transmission electron microscopy ((S)TEM) images in Figure 2-14. The RHEED streaks of $Bi_2Se_3$ grown on BIS-BL are much brighter than $Bi_2Se_3$ directly grown on $Al_2O_3$ (0001) substrate as shown in the second and sixth columns in Figure 2-14(a). The brighter RHEED pattern in reciprocal space indicates lower disordered atomic surface structure in real space. In addition, STEM images of $Bi_2Se_3$ grown on BIS-BL in Figure 2-14(b) and (c) show an atomically sharp interface between $Bi_2Se_3$ and BIS layers. Compared with the images of BIS-BL, $Bi_2Se_3$ films grown on $Al_2O_3$ (0001) and Si (111) in Figure 2-14(d) and (e) show the disordered interface between $Bi_2Se_3$ and the commercial substrates. Altogether, the $Bi_2Se_3$ films grown on BIS-BL exhibit the best crystalline quality, eventually allowing hole-doping to be feasible as will be discussed in CHAPTER 2.

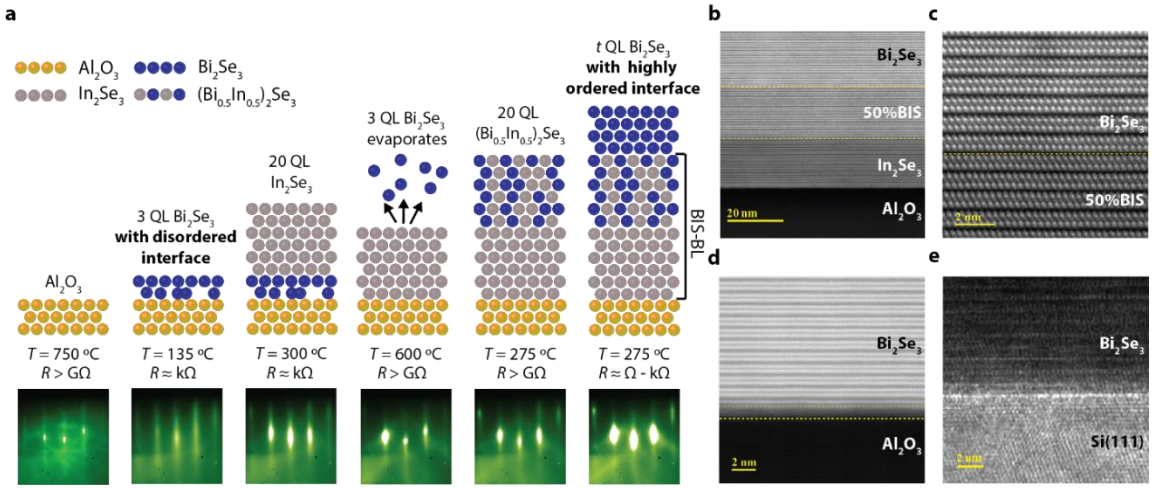


Figure 2-14. The growth process of $Bi_2Se_3$ films on the $In_2Se_3$–$(Bi_{0.5}In_{0.5})_2Se_3$ buffer layer (BIS-BL) and comparison with films grown on BIS-BL, $Al_2O_3$ (0001), and Si (111). (Taken from [68]Koirala, et al., 2015). (a) Cartoon showing each step of the growth process along with the corresponding growth temperature (*T*), sheet resistance (*R*), and RHEED images. (b, c) High-angle annular dark-field scanning transmission electron microscopy (HAADF-STEM) images of $Bi_2Se_3$ grown on BIS-BL. (c) The image with higher resolution on the interface between $Bi_2Se_3$ and BIS shows an atomically sharp interface, while (d) $Bi_2Se_3$ grown directly on $Al_2O_3$ (0001) has a clearly disordered interface, indicated by the hazy region in the yellow dotted lines. (e) A TEM image of $Bi_2Se_3$ grown on Si (111). (Taken from [55]Bansal, et al., 2011)

# CHAPTER 3. MEASUREMENT TECHNIQUES

In the previous chapter, the growth processes of high-quality TI thin films were introduced in detail utilizing MBE facilities. In this chapter, we will briefly introduce the semiclassical transport theory followed by the practice of transport measurements at Rutgers University. The electrical transport properties obtained by the measurements are sensitive indicators of the film quality as discussed, and more importantly, are used to understand novel physical states behind the surface states of topological materials.

## 3.1 Semiclassical transport theory

### 3.1.1 Ordinary Hall effect

When an external magnetic field is applied perpendicular to an electrical current, the moving charge carriers deflect to the sides due to the Lorentz force as shown in Figure 3-1. This generates a transverse electrical potential difference (Hall voltage), that is the ordinary Hall effect (OHE) ([82]Hall, 1879). In an OHE, the equation of motion based on the Drude model for a charged particle is:

$$\frac{d\vec{p}}{dt} = q\left(\vec{E} + \vec{v} \times \vec{B}\right) - \frac{\vec{p}}{\tau}, \tag{3-1}$$

where $\vec{p}$, $\vec{v}$, and $q$ are momentum, velocity, and electrical charge of the particle (for example, $q = e$ for holes, $q = -e$ for electrons), respectively. $\vec{E}$ is the electric field, consisting of internal (transverse) and external (longitudinal) fields. $\vec{B}$ is an external magnetic field, perpendicular to the electric current. $\tau$ is the relaxation time. Strictly speaking, we assume that an electron experiences a collision with a probability per unit time $1/\tau$. In a steady state, the net momentum of the carriers remains constant and thus Equation (3-1) reduces to:

$$\begin{cases} \hat{x}: \ 0 = q\left(E_x + v_y B\right) - \dfrac{p_x}{\tau} \\ \hat{y}: \ 0 = q\left(E_y - v_x B\right) - \dfrac{p_y}{\tau} \end{cases} \tag{3-2}$$

According to the standard definition of electric current density,

$$\vec{J} = nq\vec{v} = \vec{\vec{\sigma}} \cdot \vec{E} \tag{3-3}$$

Equation (3-2) can be expressed by the following matrix form.

$$\begin{aligned} \vec{E} &= \begin{pmatrix} E_x \\ E_y \end{pmatrix} = \begin{pmatrix} \dfrac{m}{nq^2\tau} & -\dfrac{B}{nq} \\ \dfrac{B}{nq} & \dfrac{m}{nq^2\tau} \end{pmatrix} \begin{pmatrix} J_x \\ J_y \end{pmatrix} \\ &= \frac{m}{nq^2\tau} \begin{pmatrix} 1 & -\dfrac{q\tau}{m} B \\ \dfrac{q\tau}{m} B & 1 \end{pmatrix} \begin{pmatrix} J_x \\ J_y \end{pmatrix} \\ &= \vec{\vec{\rho}} \cdot \vec{J} \end{aligned} \tag{3-4}$$

By the definition of Hall resistance, $R_{xy} = E_y/J_x$, the Hall resistance is proportional to the external magnetic field with a slope $1/(nq)$:

$$R_{xy} = \frac{E_y}{J_x} = \frac{B}{nq}. \tag{3-5}$$

Therefore, the Hall effect curve becomes linear as in Figure 1-4(c). The slope is known as the Hall coefficient ($R_{\text{Hall}}$) and is directly related to $n$, the sheet carrier density ($n_{2D}$), due to the 2D nature of this measurement. The $n_{2D}$ is one of the most important electrical transport properties which implies overall film quality.

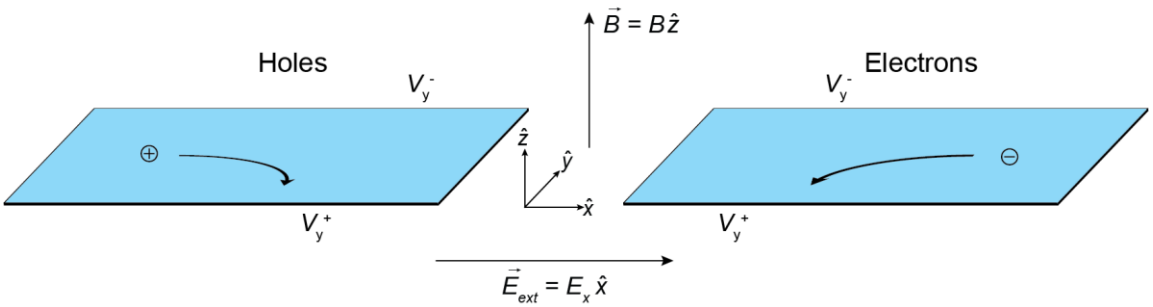


Figure 3-1. Hall effect description for holes and electrons. The electrical current flows along the direction of the external electric field, the $\hat{x}$-direction. The external magnetic field is applied in the $\hat{z}$-direction. Hall voltage is measured along the $\hat{y}$-direction, between $V_y^+$ and $V_y^-$.

### 3.1.2 Sheet resistance

Before moving on to the actual calculation of $n_{2D}$ and mobility, we need to think about the concept of sheet resistance. Sheet resistance is applicable to 2D systems in which films are thin enough to be considered 2D entities. In 3D systems, a resistance is expressed as

$$R = \rho \frac{L}{A}, \tag{3-6}$$

where $\rho$ is the resistivity, $A$ and $L$ are the area and length of the resistance body, respectively, as shown in Figure 3-2(a). The $\rho$ is considered as one of the material's properties. Likewise, in 2D systems, sheet resistances represent a similar property of thin films.

Let us express the area $A$ in 3D systems as $A = t \cdot W$, where $t$ is the thickness of the film and $W$ is the width as shown in Figure 3-2(b). Then, Equation (3-6) can be modified as

$$R = \rho \frac{L}{A} = \rho \frac{L}{t \cdot W} = \frac{\rho}{t} \cdot \frac{L}{W} = R_S \cdot \frac{L}{W}, \tag{3-7}$$

where $R_S$ is the sheet resistance. The $R_S$ can be estimated as $R_S = R \cdot W/L$ from transport experimental results. The $R$ is obtained from the measurement, and $W/L$ is related to the

measurement geometry. Comparison of Equations (3-6) and (3-7) tells us that the $R_S$ is the 2D version of 3D resistivity. Therefore, the diagonal components $\rho_{xx}$ and $\rho_{yy}$ are sheet resistances.

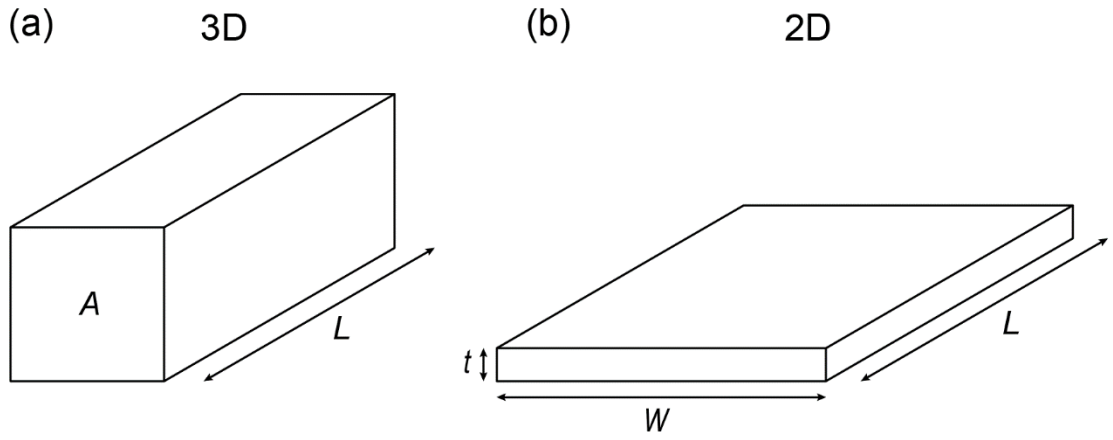


Figure 3-2. Schematic comparison of 3D and 2D resistances. (a) In a 3D case, the resistance is expressed as $R = \rho \cdot L/A$, where the $\rho$ is the resistivity.

### 3.1.3 Sheet carrier density and mobility from electrical transport measurements

The most important transport properties in thin-film studies are sheet carrier density ($n_{2D}$) and mobility ($\mu$). By the definition of mobility,

$$\mu \equiv \frac{v}{E} = \frac{J/nq}{J/\sigma_0} = \frac{\sigma_0}{nq} = \frac{nq^2\tau/m}{nq} = \frac{q\tau}{m}, \tag{3-8}$$

the sheet resistance, $R_S$ or $\rho_{xx}$ ($\rho_{yy}$), is expressed with the $\mu$ as follows.

$$R_S = \rho_{xx}(\text{or } \rho_{xx}) = \frac{m}{nq^2\tau} = \frac{1}{nq\mu} \tag{3-9}$$

Consequently, the mobility $\mu$ can be finally obtained as

$$\mu = \frac{1}{R_S \cdot n_{2D} \cdot q} \tag{3-10}$$

The $n_{2D}$ can be calculated using Equation (3-5) as follows.

$$n_{2D} = \frac{1}{e \cdot R_{Hall}\,(\text{slope})} \tag{3-11}$$

The $R_{Hall}$, the slope of the Hall effect curve, can be obtained by linear fitting of data. In reality, raw data from actual measurements could be nonlinear or asymmetric, which comes from unavoidable imperfection in the measurement setups. Therefore, a post-process is required to pick up only reasonable data sets: symmetrization and antisymmetrization (discussed in Section 3.2.3). The two quantities in Equations (3-10) and (3-11) are our main interest in the transport studies to evaluate and improve the film quality and to plan the next step of the research.

### 3.1.4 Determination of carrier density and mobility from nonlinear Hall effect via the two-carrier model

In a classical regime, Hall effect curves are linear if there is only one kind of charge carrier in the system. However, multiple types of carriers lead to deviation of the Hall effect curve due to different sheet carrier densities and mobilities. In this case, we need another way to extract the carrier densities and mobilities using a multiple carrier model instead of a simple linear fitting. In this section, we will introduce the simplest case, two carriers.

By taking the inverse of the resistance matrix tensor in Equation (3-4), the conductivity tensor becomes:

$$\ddot{\sigma} = \frac{nq^2\tau}{m}\begin{pmatrix} 1 & -\frac{q\tau}{m}B \\ \frac{q\tau}{m}B & 1 \end{pmatrix}^{-1} = \frac{nq^2\tau}{m}\cdot\frac{1}{1+\frac{q^2\tau^2}{m^2}B}\begin{pmatrix} 1 & \frac{q\tau}{m}B \\ -\frac{q\tau}{m}B & 1 \end{pmatrix}, \tag{3-12}$$

where $\sigma_0$ is the conductivity without a magnetic field, then the conductivity tensor is finally simplified to:

$$\ddot{\sigma} = \frac{qn\mu}{1+\mu^2 B^2}\begin{pmatrix} 1 & \mu B \\ -\mu B & 1 \end{pmatrix}. \tag{3-13}$$

When we have multiple types of carriers, the total conductivity should be the summation of each contribution such that:

$$\ddot{\sigma}_{tot} = \sum_i \ddot{\sigma}_i = \sum_i \frac{q_i n_i \mu_i}{1+\mu_i^2 B^2}\begin{pmatrix} 1 & \mu_i B \\ -\mu_i B & 1 \end{pmatrix} \tag{3-14}$$

For a simple case where there are only two types of carriers (types 1 and 2),

$$R_{xy}(B) = -\frac{B}{e}\cdot\frac{(n_1\mu_1^2 + n_2\mu_2^2) + (n_1+n_2)\mu_1^2\mu_2^2 B^2}{(n_1\mu_1 + n_2\mu_2)^2 + (n_1+n_2)^2\mu_1^2\mu_2^2 B^2}, \tag{3-15}$$

where $n_1$, $n_2$, $\mu_1$, and $\mu_2$ are the sheet carrier densities and mobilities of types 1 and 2, respectively. Using Equation (3-15), we can extract the four transport properties by nonlinear fitting to the Hall effect curve.

## 3.2 Transport measurement: Practice

### 3.2.1 Transport measurement systems: Electromagnet and Cryogenic

There are two systems for electrical transport measurements equipped with their own electromagnets and cryogenic systems in the MBE group at Rutgers University. One system, designed and manufactured by American Magnetic Incorporated (AMI), uses liquefied helium (LHe) and nitrogen (LN) to get down to low temperatures. In Figure 3-3, the outermost part of the blue container is a vacuum space to prevent the cryogens inside from thermal leakage from the outside walls at room temperature. The outermost chamber is for LN, which allows thermal

shielding of the LHe inside, which is located below and slightly inside the LN chamber. When a sample is mounted and inserted, the AMI system cools by injecting the LHe into the sample space, which requires opening a needle valve at a small angle. The injected LHe starts to vaporize and the system can get down below the LHe boiling point, 4.2 K, by pumping the vaporized He, which forces the He to vaporize more. In this way, the system can achieve its base temperature of about 1.5 K. The magnet is operated by supplying DC current to the magnet. The maximum field is ±9 T with a niobium–titanium alloy superconducting solenoid magnet. To keep the solenoid superconducting, the solenoid resides in the LHe space.

The other measurement system used was designed and manufactured by Advanced Research Systems (ARS) (see Figure 3-4). It does not require any cryogenic liquid to cool the system. Instead, a compressor is used for the cooling process with repetition of compressing and expanding pure helium gas enclosed (~205 psi for static, ~275 psi in operation). In this way, the temperature can be as low as 5 K as its base temperature. This system runs an electromagnet which can go up to ±0.6 T. Both the compressor and electromagnet need to be cooled by tap water flow.

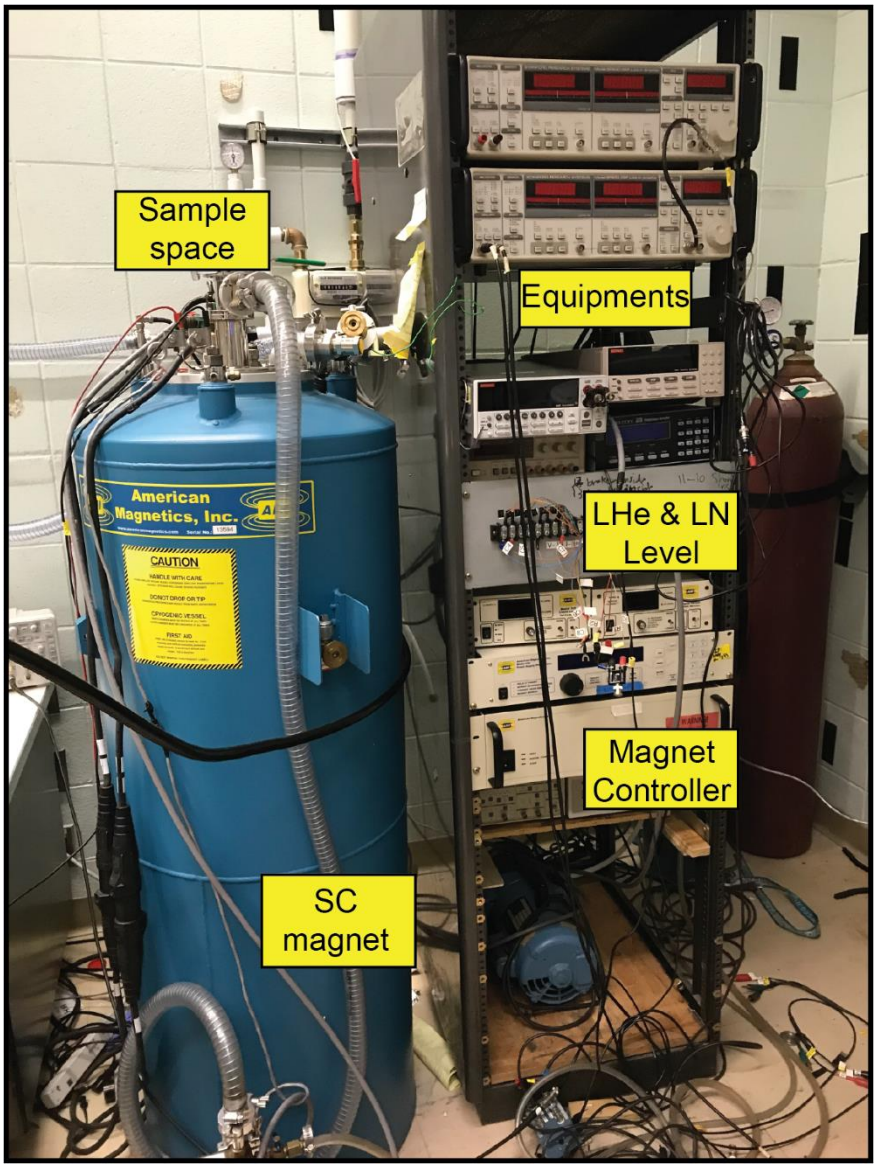


Figure 3-3. Transport measurement system using a superconducting magnet. The base temperature and maximum magnetic field are 1.5 K and 9 T, respectively.

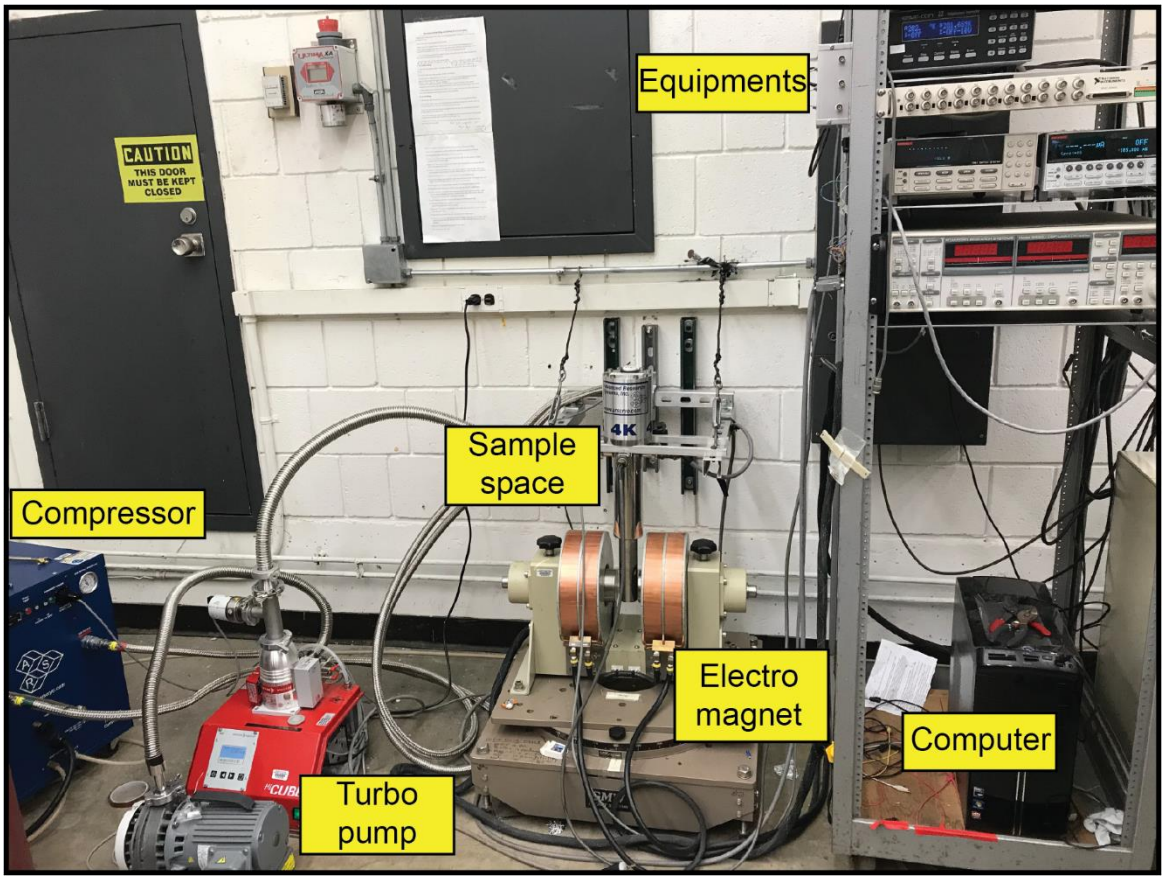


Figure 3-4. Transport measurement system using an electromagnet. The base temperature and maximum magnetic field are 5 K and 0.6 T, respectively.

### 3.2.2 Measurement geometries: van der Pauw and Hall bar

The van der Pauw method is a four-probe measurement technique, which allows obtaining the specific resistivity (sheet resistance) and measuring the Hall effect of a flat sample of arbitrary shape without knowing the current pattern. To do this, the following conditions should be fulfilled:

(a) The contacts are at the circumference of the sample.

(b) The contacts are sufficiently small.

(c) The sample is homogeneous in thickness.

(d) The surface of the sample is singly connected, i.e., the sample does not have isolated holes.

Figure 3-5(a–c) shows the typical square-shaped van der Pauw geometry which has been used in this dissertation. To calculate the sheet resistance, we need to perform an averaging procedure with the leads in various locations ([83]Van der Pauw, 1958a; [84]1958b). For our flat and homogeneous samples, the van der Pauw method simply gives us

$$R_S \approx \frac{\pi}{\ln(2)} R_{xx}, \tag{3-16}$$

where $R_{xx}$ is experimentally measured and taken to be the average of $R_{xx}$ and $R_{yy}$, and $\pi/\ln(2)$ is known as the geometric factor. To obtain the sheet resistance in the Hall bar geometry, one measures $R_{xx}$ (= $V_x/I_x$). The geometric factor is determined by $L/W$, where $L$ and $W$ are defined in Figure 3-5(d). Therefore, in Hall bar geometry, the sheet resistance is calculated as $R_S = R_{xx}(W/L)$.

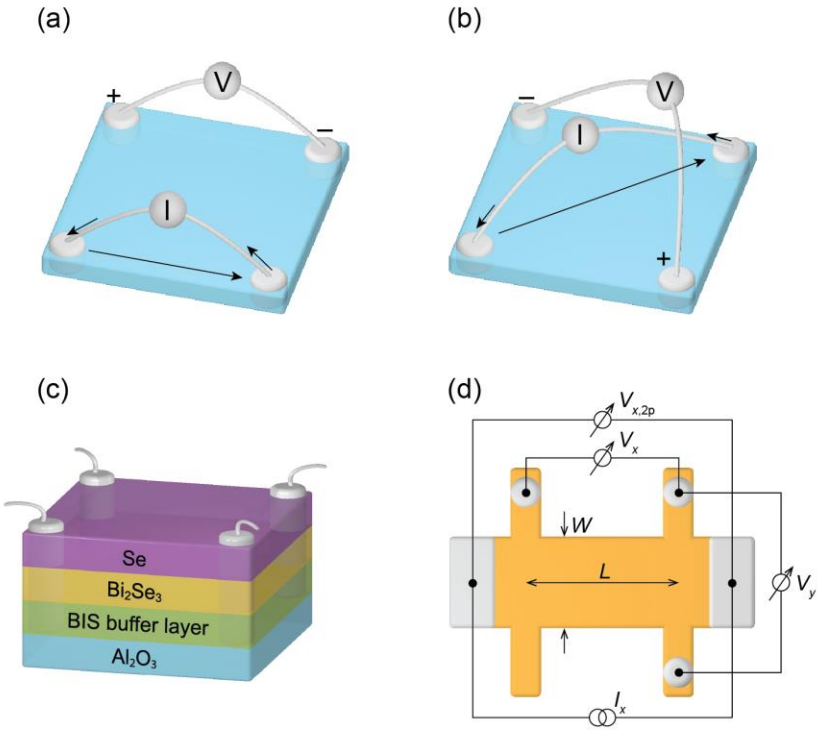


Figure 3-5. Schematic illustrations of transport measurement geometries. (a–c) Van der Pauw geometry. (a) Longitudinal (magneto, $R_{xx}$ and $R_{yy}$) resistance measurement. (b) Transverse (Hall, $R_{xy}$ and $R_{yx}$) resistance measurement. (c) A schematic of the van der Pauw geometry with a typical $Bi_2Se_3$ film. The lead contacts penetrate down to the substrate. (d) Hall bar geometry. Taken from Figure 1-5(b) for convenience.

### 3.2.3 Post data process: Symmetrization–antisymmetrization

Regardless of the van der Pauw or Hall bar geometry, there always exist unavoidable interference between the longitudinal and transverse components of the measurement. The interference in Hall bar geometry could be smaller than that in van der Pauw, but it is almost inevitable in typical hand-

patterned ones unless the patterning is extremely small and accurate, probably in the scale of micrometers. Figure 3-6 shows a typical raw data set of a transport measurement. As shown in Figure 3-6(e) and (f), the $R_{xx}(B)$ and $R_{yy}(B)$ are not symmetric, which indicates there is significant mixing from $R_{xy}$ and $R_{yx}$ components. After symmetrization, the interference is canceled out as shown in Figure 3-7(d).

For Hall effect measurements, the raw data are usually not affected by the geometry but shifted up and down along the Hall resistance axis due to $R_{xx}$ and $R_{yy}$ mixing as shown in Figure 3-6(c, d) and (g, h). By antisymmetrization, the Hall effect curve becomes an odd function as in Figure 3-7(a) and (e). From those refined data, we extract the electrical transport properties such as $n_{2D}$ and $\mu$ by fitting the Hall effect data and further calculation as discussed in Section 3.1.3.

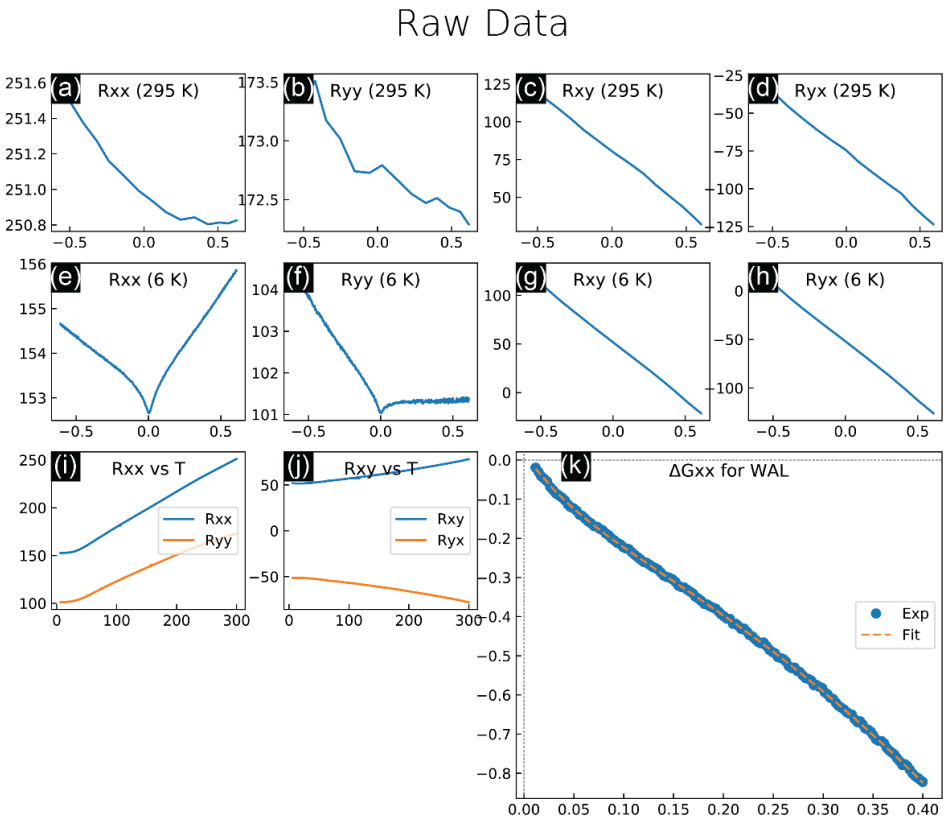


Figure 3-6. Typical raw data of a transport measurement. (a, b) Magnetoresistance and (c, d) Hall effect data measured at room temperature. (e, f) Magnetoresistance and (g, h) Hall effect data measured at 6 K. (i, j) Temperature dependence of (i) $R_{xx}$ and $R_{yy}$ and (j) $R_{xy}$ and $R_{yx}$. (k) Change in longitudinal conductance ($\Delta G_{xx}$) vs magnetic field data before WAL fitting.

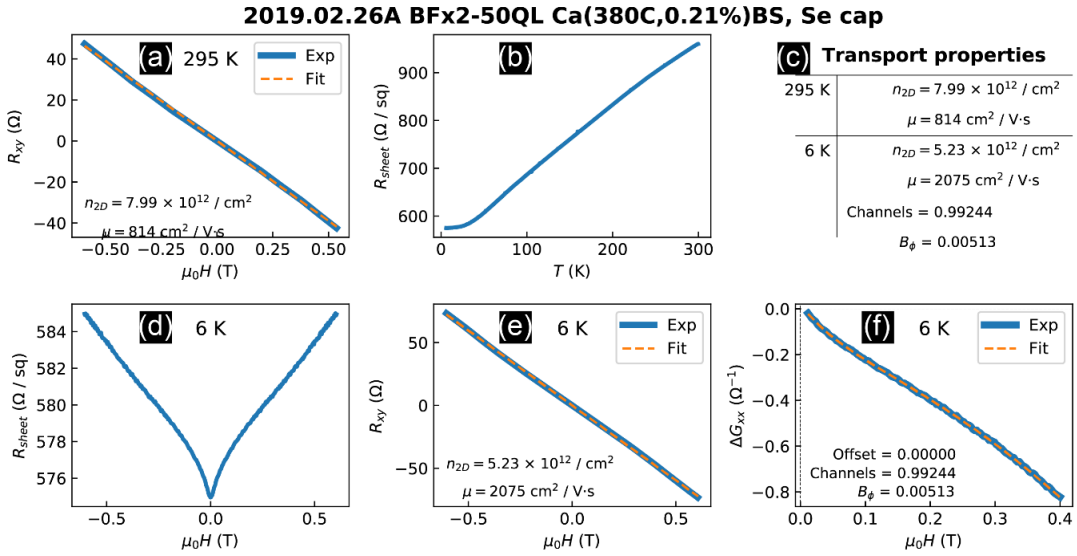


Figure 3-7. A data set of a transport measurement (50 QLs of Ca-doped $Bi_2Se_3$ grown on BIS-BL capped by Se, 2019.02.06A) after the post-processes, symmetrization and antisymmetrization. (a) Antisymmetrized Hall effect data measured at room temperature. (b) Temperature dependence of sheet resistance data. (c) Panel showing the calculated transport properties. (d) Symmetrized magnetoresistance data measured at 6 K. (e) Antisymmetrized Hall effect data measured at 6 K. (f) WAL fitted $\Delta G_{xx}(B)$ curve. The number of conducting channels of this film is approximately 1.

## 3.3 Ex situ thickness calibration: Rutherford backscattering spectroscopy

Rutherford backscattering spectrometry (RBS) is a 100-year-old technology that is still a powerful tool for determining the structure and composition of materials by measuring the backscattered beam of high-energy ions, typically alpha particles ($He^{2+}$), impinging on a sample. The Laboratory for Surface Modification at Rutgers University hosts a 1.7 megavolt Tandetron accelerator used for RBS measurements, which is shown in Figure 3-8(a). This system is a tandem accelerator, which uses the same (high) electric potential twice to accelerate charged ions, usually alpha particles. Initially, the source of alpha particles (helium gas) and the target are near ground potential. They

are separated by the positively charged high-voltage terminal. The helium gas is injected through an ionizer that negatively ionizes them by adding an electron to a helium atom. The negatively charged ions are now accelerated toward the positive high-voltage terminal. The accelerated helium ions pass through an electron stripper near the positive terminal, losing electrons. Consequently, the net charge of the ions is converted from negative ($1^-$) to positive ($1^+$ or $2^+$). This change in net charge forces them to be accelerated again as they move away from the positive terminal toward the target that is at ground potential. Then, the highly accelerated ions arrive at the sample, impinging onto the surface at normal incidence, and the backscattered ions are detected at 165° relative to the incoming beam using a silicon detector.

As mentioned above, ions scattered elastically from the nuclei of atoms in the sample are detected by a silicon particle detector. In consideration of the fact that the energy of the scattered ion depends on the mass and depth of the target atom, the composition and layering of the sample can be determined very precisely. For MBE grown thin films, the thickness and composition of the films can be precisely determined by analyzing the RBS results. Upon reaching the target, the ions bounce off the atoms in the sample by simple Coulomb interaction (repulsion), which allows assuming that the total energy and momentum are conserved. Then, we can simply apply the hard-sphere approximation to the kinetics, which yields $E_1 = kE_0$ where $E_0$ is the incoming energy prior to scattering and $E_1$ is the measured outgoing energy after scattering. $k$ is called the kinematical factor and is given by

$$k = \frac{\left(\sqrt{m_1^2 - m_2^2 \sin^2\theta} + m_1 \cos\theta\right)^2}{m_1 + m_2} \tag{3-17}$$

where $\theta$ is the angle of the backscattered ion (fixed in the lab), with mass $m_1$, relative to the incoming ion beam (see Figure 3-8(c)), and $m_2$ is the mass of the nuclei in the film. The Coulomb potential between the nuclei and the ion gives the standard Rutherford cross section

$$\sigma = \left( \frac{Z_1 Z_2 e^2}{4E_0} \right)^2 \frac{1}{\sin^4 \frac{\theta}{2}} \tag{3-18}$$

for a target atom with nuclear charge $Z_2$, and incoming ion with nuclear charge $Z_1$. The cross section and kinematical factor are sensitive to the elemental species in the films that scatter the incoming ion. This allows RBS to probe the chemical composition of films.

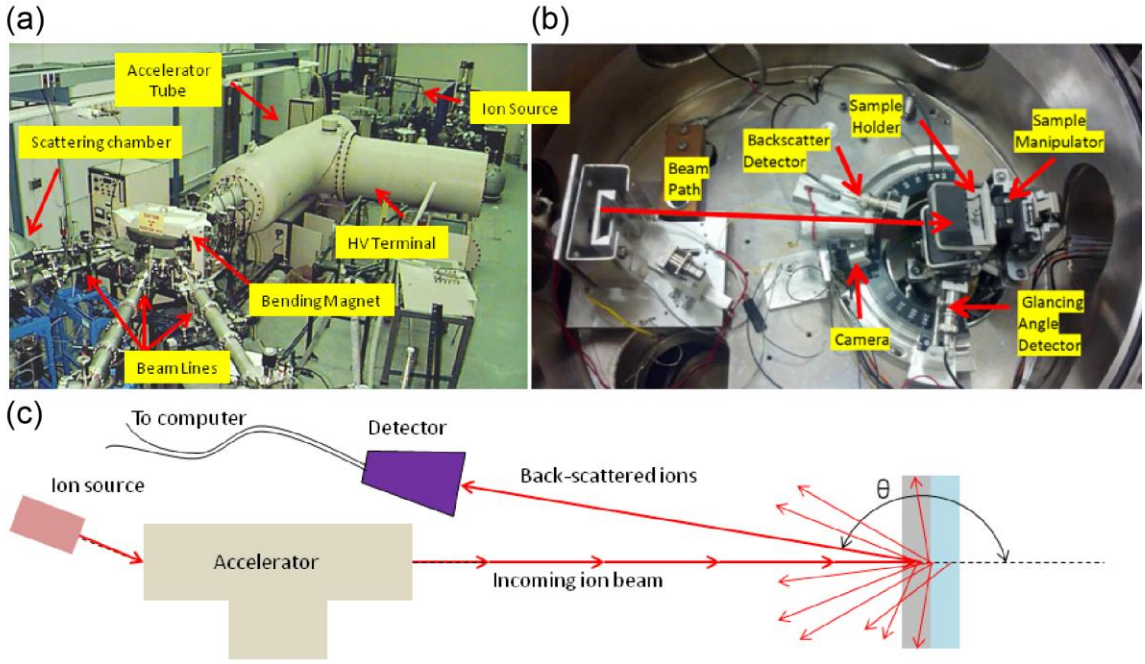


Figure 3-8. Rutherford backscattering spectroscopy experiment facility at Rutgers University and its schematic description. (a, b) The Tandetron accelerator located at the Laboratory for Surface Modification at Rutgers University. (a) A wide-angle view of the entire system. (b) The scattering chamber (a-b: Adapted from [85]Bartynski, 2013). (c) A schematic description of a typical RBS experiment. The ions are generated, doubly accelerated, then impinged on the sample. After backscattering events, they are finally detected by a silicon detector at a fixed angle $\theta$, as a function of energy. (c: Adapted from [86]Brahlek, 2014)

## 3.4 Beyond structural characterization

### 3.4.1 Scanning tunneling microscopy

STM is one of the very powerful ways for imaging surfaces with a resolution sufficient to resolve single atoms. Using the quantum mechanical tunneling effect, electrons are allowed to tunnel beyond the surface of a solid into regions of space that are forbidden to them in classical physics. The STM technique is widely used in a variety of material-related research fields including TI thin-film studies. In this section, we will introduce the STM technique, which will provide information about the quality of the TI film surfaces as in Figure 2-13(b) and Figure 4-3(c, d).

In 1981, the STM was first started by Swiss physicists Gerd Binnig and Heinrich Rohrer (IBM Zürich) setting out to build an instrument for studying the local conductivity of surfaces. They chose a surface of gold for their first image. They saw rows of precisely spaced atoms and observed terraces separated by one-atom height steps on the display. In 1982, G. Binnig and H. Rohrer reported the real-space images of atomic structures of 7 × 7 reconstruction on the Si (111) surface, which was published the following year ([70]Binnig, et al., 1983). Their discovery opened up a new generation for surface science, and their impressive accomplishment was recognized with the award of the Nobel Prize for Physics in 1986.

Figure 3-9(a) shows a schematic illustration of the STM measurements. When a conducting tip is brought very close to the surface to be examined with a bias voltage applied between the tip and the surface, electrons can tunnel through the vacuum between them. Under the assumption that the tip state is well-described by an s-wave function with spherical symmetry, the resulting tunneling current is expressed as

$$I_t \propto V_t \sum_{\nu} \left|\psi_{\nu}(\vec{r_0})\right|^2 \delta(E_{\nu} - E_F) = \rho\left(E_F, \vec{r_0}\right), \tag{3-19}$$

which shows that the tunnel current is proportional to the bias voltage and to the local density of states (LDOS), $\rho$, at the Fermi level evaluated at the center of curvature of the tip apex ( $\vec{r_0}$ ). The current decays exponentially as the tunneling barrier height increases.

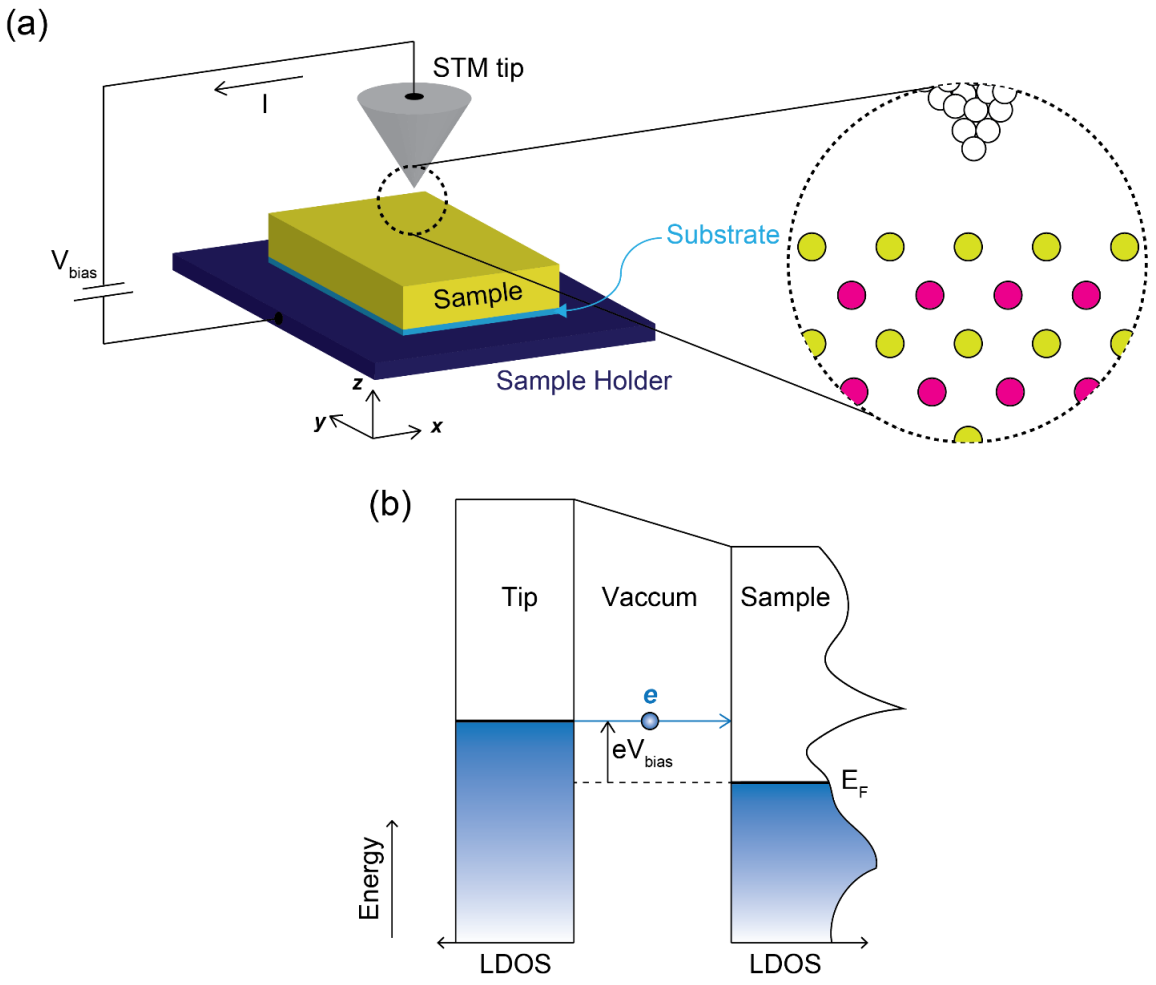


Figure 3-9. Schematic illustration of the principles of STM and energy diagram of the tip–sample tunnel junction. (a) Raster scanning is performed by the sharp tip across the surface at a distance of a few Ångströms. A feedback loop maintains the height of the tip so that the tunneling current stays constant. (b) A bias voltage $V$ is applied to the tip, then tunneling proceeds from the occupied tip states to the empty sample states.

### 3.4.2 Angle-resolved photoemission spectroscopy

Angle-resolved photoemission spectroscopy (ARPES) is a surface sensitive technique that typically uses X-rays to excite and emit electrons out of the material. As shown in

Figure 3-10, a beam of monochromatized radiation produced either by a gas-discharge lamp or by a synchrotron radiation source is incident on to a sample in UHV (typically below $5 \times 10^{-11}$ Torr). The sample has to be a properly aligned single crystal for momentum-resolved measurements. Subsequently, electrons are emitted by the photoelectric effect and escape into the vacuum in all directions. By collecting the emitted electrons with an electron energy analyzer set at a nonzero acceptance angle, one can measure the kinetic energy $E_{\text{kin}}$ of the photoelectrons for a given emission angle in parallel with the momentum of the photoelectrons. The modulus is given by $p = (2mE_{\text{kin}})^{1/2}$ and its components parallel and perpendicular to the sample surface are obtained from the polar ($\theta$) and azimuthal ($\varphi$) emission angles. For an incoming photon with energy $\hbar v$, energy and momentum conservations require

$$E_{\text{kin}} = \hbar v - \varphi - |E_{\text{B}}|, \tag{3-20}$$

$$\begin{aligned} p_{||} &= \hbar k_{||} = \sqrt{2mE_{\text{kin}}}\,\sin\theta \\ p_{\perp} &= \hbar k_{\perp} = \sqrt{2m\left(E_{\text{kin}}\,\cos^2\theta + V_0\right)} \end{aligned}, \tag{3-21}$$

where $E_{\text{kin}}$ is the kinetic energy of the electrons coming out of the material, $\varphi$ is the work function of the material, and $E_{\text{B}}$ is the binding energy. The $V_0$ is a quantity related to the work function and is found by taking the $\theta = 0$ electrons. By experimentally measuring the angle $\theta$ and their final kinetic energy, one can then trace back to get their original energies and momentum in the crystal prior to excitation, and from this information, the dispersion relation can be obtained.

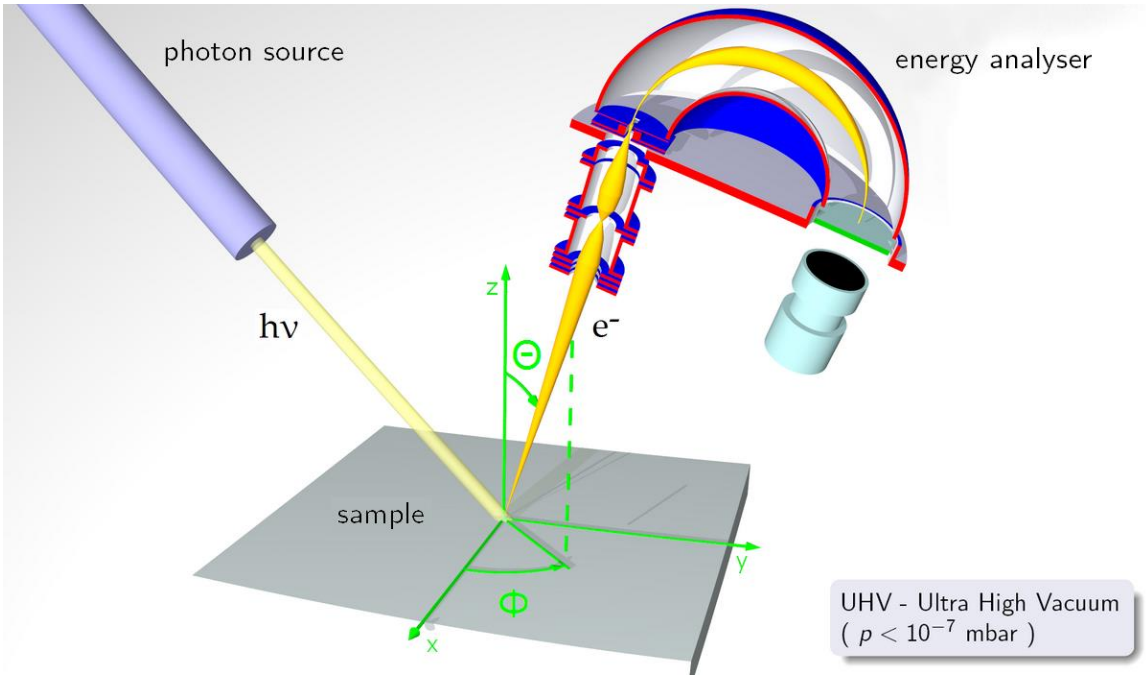


Figure 3-10. The principle of angle-resolved photoemission spectroscopy. (Adapted from [87]Wikipedia, n.d.)

# CHAPTER 4. Solution to the hole-doping in $Bi_2Se_3$ thin films

Hole (p) doping has been challenging in $Bi_2Se_3$ ([88]Mann, et al., 2013; [56]West, et al., 2012; [89]Ando, 2013), one of the most widely studied topological insulators (TIs) ([90]Brahlek, et al., 2014; [91]M.J. Brahlek, et al., 2016; [68]Koirala, et al., 2015; [92]He, et al., 2013; [93]Sharma, et al., 2014; [94]Bansal, et al., 2014; [95]Brahlek, et al., 2011). Unlike conventional semiconductor materials, the problem is complicated due to the presence of both surface and bulk states in topological insulators: we have to consider the doping problem of the surface and the bulk states separately. Both the surface and bulk states of $Bi_2Se_3$ have a strong tendency toward n-type due to its native n-type defects such as selenium vacancies ([96]Dai, et al., 2016; [97]Xue, et al., 2013; [98]Tumelero, et al., 2016; [99]Urazhdin, et al., 2002; [100]Alpichshev, et al., 2012; [101]Huang, et al., 2012; [88]Mann, et al., 2013; [56]West, et al., 2012; [89]Ando, 2013; [102]Horák, et al., 1990). In bulk crystals compensation dopants such as Ca and Mn can be used to convert the dominant carrier type from n- to p-type ([103]Li, et al., 2013; [41]Hor, et al., 2009; [104]Wang, et al., 2010; [105]Eguchi, et al., 2014; [106]Choi, et al., 2012; [107]Ka parov , et al., 2005; [108]Liu, et al., 2015; [109]Xue, et al., 2014). However, such a compensation doping scheme has not been successful in thin films of $Bi_2Se_3$. More specifically, we have tried various potential p-type dopants such as Zn, Mg, Ca, Sr, and Ba as compensation dopants, but none of them have so far led to p-type $Bi_2Se_3$ thin films; no p-type $Bi_2Se_3$ thin films have been demonstrated in the literature either. Only when they were quite thick (~200 nm), we were able to achieve p-type $Bi_2Se_3$ films through a complex process ([93]Sharma, et al., 2014). This difficulty in achieving p-type $Bi_2Se_3$ thin films has been puzzling, considering the very existence of p-type $Bi_2Se_3$ bulk crystals ([41]Hor, et al., 2009; [104]Wang, et al., 2010). It may be suspected that this discrepancy in doping efficiency between thin films and bulk crystals could be due to the different growth conditions of the two systems, such as growth temperatures, considering that films are, in general, grown at much lower temperatures than bulk crystals. However, it should be noted that even p-type $Bi_2Se_3$ bulk crystals tend to become n-type when the crystals are made into thin flakes through, say, the Scotch tape

method ([110]Checkelsky, et al., 2011). $Bi_2Se_3$ flakes can remain p-type only if they are relatively thick (> ~150 nm) ([108]Liu, et al., 2015). All these observations provide evidence that whether they are thin films or bulk crystals, thickness critically affects the doping efficiency of the $Bi_2Se_3$ system, but the origin behind this problem has been a mystery, not to mention that a solution does not exist. Finding a solution to this p-doping mystery in $Bi_2Se_3$ thin films would be a major breakthrough toward the age of topological electronics, just as the solution to the long-standing p-doping problem in GaN has led to the solid-state-lighting revolution ([111]Nakamura, 2015).

## 4.1 Hole doping problem

In order to better understand the hole-doping problem, we grew a series of $Bi_2Se_3$ thin films with different compensation doping schemes and different thicknesses and studied their carrier types and densities as shown in Figure 4-1. As for the compensation dopant, we have chosen Ca, but according to our comparison studies in 4.3.4, other alkaline earth elements such as Mg and Sr might work as well. Figure 4-1(a) shows that when $Bi_2Se_3$ thin films are directly grown on $Al_2O_3$ (0001) substrates without any capping layer or a buffer layer, the films remain n-type regardless of the compensation-doping-level for film thickness up to 50 QL.

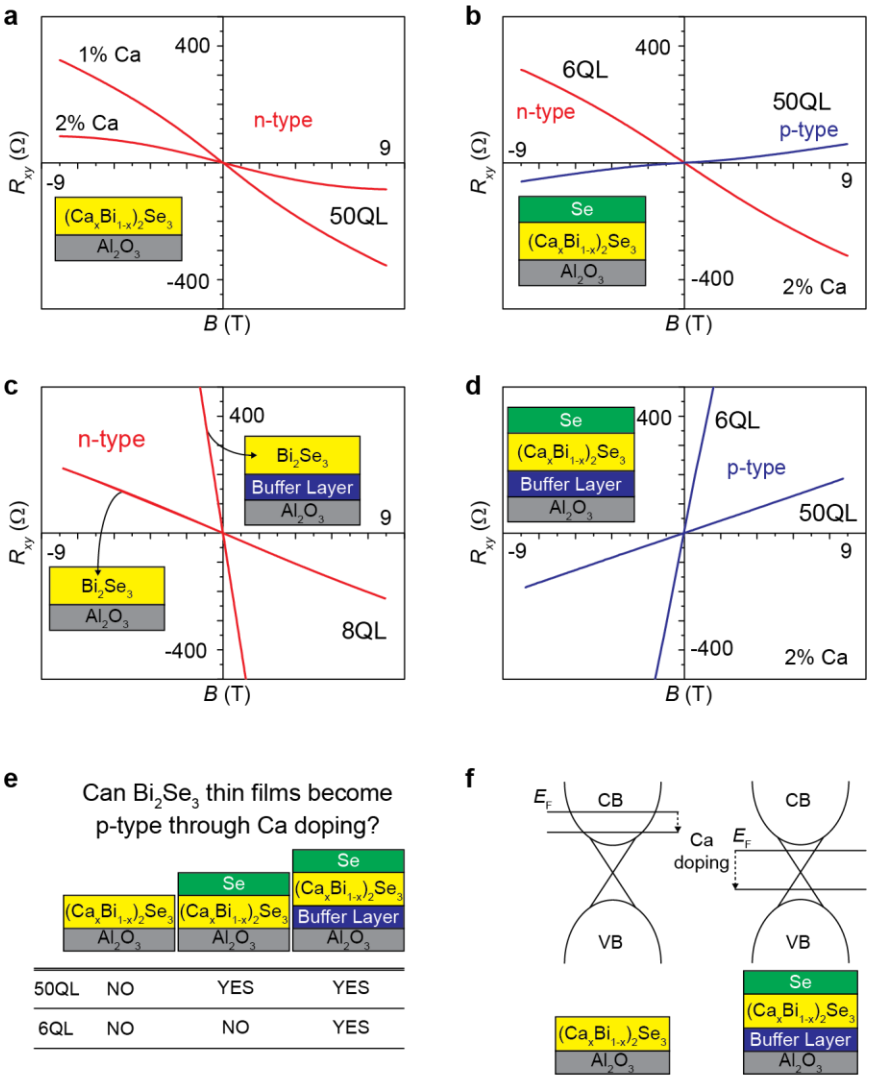


Figure 4-1. Ca doping study in $Bi_2Se_3$ thin films with different interfacial layers (at 1.5 K). (a-d) Hall resistance data, (e) summary table, and (f) schematic of energy band diagram with and without the interface layers. (a) Grown directly on $Al_2O_3$ (0001) substrates: the films remain n-type regardless of Ca-doping levels. (b) Grown on $Al_2O_3$ substrates with a Se capping layer: thick (50 QL) film can become p-type whereas thin (6 QL) film still remains n-type. (c) Effect of the BIS-BL on the interfacial defect density: the $Bi_2Se_3$ film grown on the buffer layer shows much lower carrier density than the one directly grown on $Al_2O_3$. (d) Achievement of p-type $Bi_2Se_3$ films down to 6 QL with the BIS buffer and the Se capping layers. (e) Summary table for the counter-doping effectiveness for different thicknesses and interfacial layers. (f) Schematic drawings showing the Fermi level tunability with Ca doping in $Bi_2Se_3$ films grown with and without the interfacial layers. (Adapted from [81]Moon, et al., 2018)

In order to check the effect of the air exposure, we subsequently grew another set of samples with Se capping layer, which was previously shown to be effective in protecting the surface of $Bi_2Se_3$ films from air exposure ([112]Salehi, et al., 2015). As depicted in Figure 4-1(b), the Se capping does make a difference and 50 QL $Bi_2Se_3$ film on $Al_2O_3$ is now converted to p-type. This suggests that part of the reason why counter-doping for $Bi_2Se_3$ thin films becomes ineffective is due to air exposure, which could neutralize the easily-oxidizing Ca dopant as well as add extra n-type dopant such as water vapor ([95]Brahlek, et al., 2011). However, even with the Se capping, the counter-doping still fails for much thinner (6 QL) films. This shows that air exposure is not the only reason for the failure of charge compensation doping with Ca, suggesting that the interface with the substrate is another potential source of the problem.

## 4.2 Doping control of Ca using the QCM

Before moving on to the next section, we need to take a look into how to control the doping concentration of Ca in $Bi_2Se_3$. $(Ca_xBi_{1-x})_2Se_3$ thin films are grown by codeposition of Ca, Bi, and Se. In order to control Ca doping concentration, x, we need to know the flux of Ca as well as that of Bi during growth: as for Se, its exact flux is not critical as far as it is much higher than that of Bi because extra Se does not stick. The flux of sources is measured with quartz crystal microbalance (QCM). However, unlike Bi and Se, the fluxes for Ca are too low to be reliably measured by QCM. But such low flux values can still be estimated based on QCM measurements done at higher fluxes and the source temperatures as described below.

Based on ideal gas laws, it can be easily shown that

$$\Phi_i = \Phi_j \cdot \frac{P_i}{P_j} \cdot \left( \frac{T_j}{T_i} \right)^{\frac{1}{2}} \tag{4-1}$$

, where $\Phi_i$ and $\Phi_j$ are source fluxes (/cm$^2$·s), $P_i$ and $P_j$ are vapor pressures (Torr) of the source at the source temperatures, $T_i$ and $T_j$ (K), respectively ([113]Henini, 2012). The vapor pressure of Ca as a function of temperature is available online (Table 4-1), and it turns out that it can be precisely fit by:

$$\log(P) = a_0 + a_1 \cdot T + a_2 \cdot T^2 \tag{4-2}$$

, where $a_0$, $a_1$, and $a_2$ are the fitting parameters. Then, $\Phi_i$ can be expressed as follows.

$$\Phi_i = \Phi_j \cdot \frac{e^{a_0 + a_1 \cdot T_i + a_2 \cdot T_i^2}}{e^{a_0 + a_1 \cdot T_j + a_2 \cdot T_j^2}} \cdot \left( \frac{T_j}{T_i} \right)^{\frac{1}{2}} \tag{4-3}$$

In order to use Equation (4-3) for Ca, we fit the vapor pressure and temperature data of Ca in Table S1, and find $a_0 = -40.67817$, $a_1 = 0.09757$, and $a_2 = -6.30447 \times 10^{-5}$. Then, we measure using QCM the Ca flux at a higher source temperature, 580 ℃ ($T_j$), which turns out to be $5.5 \times 10^{13}$ /cm$^2$·s ($\Phi_j$). Substituting the fitting parameters, the source temperature ($T_j$) and the flux ($\Phi_j$) at the higher temperature, Equation (4-3) becomes a function of $T_i$ only, the source temperature. With the typical flux of Bi in our growth, $2.01 \times 10^{13}$ /cm$^2$·s, we can calculate the Ca concentration in $(Ca_xBi_{1-x})_2Se_3$: $\frac{\Phi_{Ca} \cdot \alpha}{\Phi_{Bi} + \Phi_{Ca} \cdot \alpha} \times 100(\%)$, where $\Phi_{Ca}$ is the Ca flux, $\Phi_{Bi}$ is the Bi flux, and $\alpha$ is a coefficient, which turns out to be 0.36, to adjust the QCM-measured flux to match the doping concentration measured by STM, say, for a 2% Ca-doped $Bi_2Se_3$ film. Using this method, we can estimate the doping concentration at much lower temperatures than can be measured by QCM. The Ca doping levels and the corresponding source temperatures used in our study are shown in Table 4-1.

| Vapor pressure (Torr) | $10^{-7}$ | $10^{-6}$ | $10^{-5}$ | $10^{-4}$ | $10^{-3}$ |
|---|---|---|---|---|---|
| Temperature (℃) | 317 | 357 | 405 | 459 | 522 |

Table 4-1. Vapor pressures at selected source temperatures of Ca. The data are available from Veeco. (Adapted from [81]Moon, et al., 2018)

| Temperature (°C) | Flux ($\Phi_{Ca}$, $10^{10}$ /cm$^2$·s) | Doping level (%) |
|---|---|---|
| 355 | 2.5 | 0.04 |
| 365 | 4.1 | 0.07 |
| 367 | 4.5 | 0.08 |
| 368 | 4.8 | 0.09 |
| 370 | 5.3 | 0.10 |
| 373 | 6.1 | 0.11 |
| 375 | 6.8 | 0.12 |
| 376 | 7.1 | 0.13 |
| 378 | 7.9 | 0.14 |
| 382 | 9.6 | 0.17 |
| 394 | 17.0 | 0.30 |
| 412 | 38.9 | 0.69 |
| 417 | 48.6 | 0.86 |
| 422 | 60.5 | 1.07 |
| 427 | 75.1 | 1.33 |
| 437 | 114.8 | 2.02 |
| 457 | 258.2 | 4.42 |

Table 4-2. Ca doping level in $Bi_2Se_3$ films controlled by the source temperature. The flux is estimated by the expression, Equation (4-3), and the doping level is calculated by $\Phi_{Ca}\cdot\alpha$ / ($\Phi_{Bi}$ + $\Phi_{Ca}\cdot\alpha$) × 100 (%) with $\alpha$ = 0.36, $\Phi_{Bi}$ = 2.01 × $10^{13}$ /cm$^2$·s. (Adapted from [81]Moon, et al., 2018)

## 4.3 Solution to the hole doping problem: $(Bi_{0.5}In_{0.5})_2Se_3$ buffer layer

As mentioned in 2.5.5, the interfacial defects originating from chemical and structural mismatch with the commercial sapphire substrates bring about the most of the native defects responsible for the high level of n-type carrier densities in $Bi_2Se_3$ thin films. This is why high density of n-type carriers is present, preventing $Bi_2Se_3$ thin films from being hole-doped ([46]Kim, et al., 2011). Therefore, we decided to employ the $In_2Se_3$-$(Bi_{0.5}In_{0.5})_2Se_3$ buffer layer (BIS-BL). We will show how the incorporation of the BIS-BL solves this problem and makes the hole doping of $Bi_2Se_3$ thin films possible.

### 4.3.1 Achievement of p-type $Bi_2Se_3$ thin films

By employing both the BIS-BL and the Se capping layer, we were able to implement p-type $Bi_2Se_3$ thin films down to the thinnest topological regime (6 QL) as shown in Figure 4-1(d). As summarized in Figure 4-1(e), previous failures of counter-doping for thin $Bi_2Se_3$ films originate from two factors: first, neutralization of the counter-dopants due to air exposure on the top surface and second, high density of defects at the interface with the substrate. When $Bi_2Se_3$ films are grown directly on commercial substrates, there exists a high density of defects confined to the interface between the film and the substrate. These interfacial defects lead to high level of n-type carriers with the surface Fermi level located far above the bottom of the conduction band minimum ([56]West, et al., 2012; [93]Sharma, et al., 2014; [78]Bansal, et al., 2012). Our current study suggests that this interfacial defect density on the commercial substrate is higher than the solubility limit of the compensation dopant so that the film remains n-type up to the maximum counter-doping (Figure 4-1(f)). On the other hand, with the BIS-BL, the interfacial defect density drops below the solubility limit of the compensation dopant and the Fermi level can be tuned below the Dirac point, leading to p-type $Bi_2Se_3$ films.

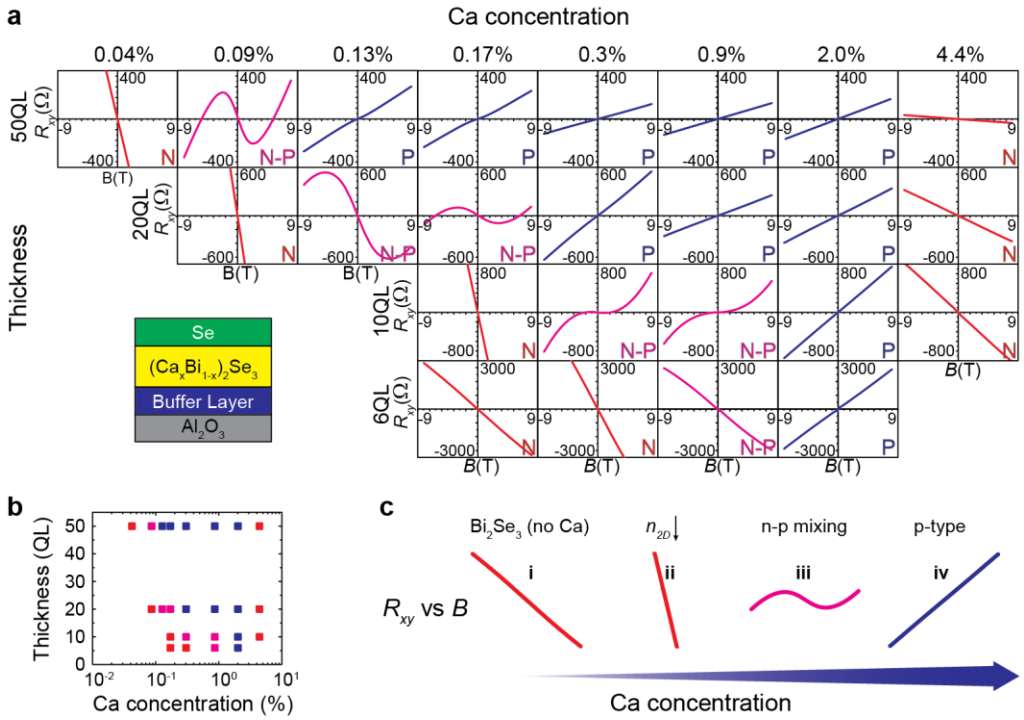


Figure 4-2. Hall resistance study for n- and p-type $Bi_2Se_3$ thin films (at 1.5 K). (a) $R_{xy}(B)$ data vs Ca concentration and thickness for Ca-doped $Bi_2Se_3$ films with the BIS buffer and the Se capping layers. n-type (negative slope) and p-type (positive slope) curves are colored as red and blue, respectively, and the nonlinear, n-p mixed curves are colored as pink. As Ca concentration increases, all the films transition from n- to p-type through n-p mixed regime, and then eventually become n-type again except for the 6 QL film, which becomes insulating, instead. (b) A phase diagram for the carrier type in the thickness and Ca concentration space: n, n-p mixed, and p regime are depicted as red, pink and blue squares, respectively. Note that the phase space for the p regime shrinks as the film gets thin. (c) A cartoon showing the common trend of $R_{xy}(B)$ depending on Ca concentration for all thicknesses. (i) $Bi_2Se_3$ is naturally n-type without Ca dopants. (ii) As Ca doping level increases, the (n-type) sheet carrier density gradually decreases, resulting in increased negative slope of the $R_{xy}(B)$ curve. (iii-iv) With more Ca doping, the slope changes from negative (n-type) to positive (p-type) passing through a nonlinear n-p mixed regime. (Adapted from [81]Moon, et al., 2018)

We now provide more detailed Hall effect data for a range of Ca-doped $Bi_2Se_3$ films grown on the BIS buffer and the Se capping layers in Figure 4-2(a). As the Ca doping level increases and compensates for the intrinsic n-type carriers, the (n-type) sheet carrier density gradually decreases, which appears as increasing negative slope of the $R_{xy}(B)$ curve as illustrated in Figure 4-2(c). i-ii. As we add more Ca to the films, the slope changes from negative (n-type) to positive (p-type), passing through a nonlinear n-p mixed regime: Figure 4-2(c). iii-iv. 50 QL films enter the n-p mixed regime at 0.09% of Ca and become fully p-type at 0.13%. However, as the films get thinner, gradually higher level of Ca doping is required to reach the n-p mixed and the p regimes. The n-p mixed regime started at 0.13% for 20 QL, 0.3% for 10 QL, and 0.9% for 6 QL, and the p regime started at 0.3% for 20 QL, 2.0% for 10 QL and 6 QL. As summarized in the phase diagram in Figure 4-2(b), these observations show that counter-doping becomes gradually more difficult, requiring a higher level of Ca doping, as $Bi_2Se_3$ films become thinner. This suggests that even in these interface-engineered $Bi_2Se_3$ films, the majority of defects still originate from the interfaces rather than from the bulk of the films.

### 4.3.2 Limit of the Ca doping concentration

Even though p-type $Bi_2Se_3$ films are achieved for all thicknesses from 50 QL down to 6 QL at 2% of Ca, the films again become n-type with further increase (above 4.4%) in Ca doping except for 6 QL, which becomes insulating probably due to a disorder-driven topological phase transition ([114]M. Brahlek, et al., 2016; [80]Salehi, et al., 2016). This is because Ca doping inevitably introduces disorder and thus degrades both electronic and structural properties of the $Bi_2Se_3$ films. This can be seen in the carrier density and mobility vs Ca doping plots of Figure 4-3(a) and (b). In Figure 4-3(a), we plot the sheet carrier density ($n_{2D}$) vs Ca doping for the 20 QL $Bi_2Se_3$ films grown on the BIS buffer with Se capping layers. For simplicity, we used the Hall resistance data at $B = 0$ T for the

carrier density, and excluded the nonlinear n-p mixed regime because of ill-defined $n_{2D}$ in nonlinear $R_{xy}(B)$ curves: more elaborate discussion of the data including the n-p mixed regime is given in Supporting Information Section III. It shows that the carrier type changes from n to p, and finally to n again at very high Ca concentration. In Figure 4-3(b), we plot the corresponding mobility calculated from $\mu = 1 / (n_{2D} \cdot e \cdot R_{xx})$, where $R_{xx}$ is the sheet resistance. The mobility shows a sharp drop as soon as the film becomes p-type, and gradually degrades with increasing Ca concentration in the p-regime: as we further discuss with Figure 4-6(d) later, the sharp drop of the mobility through the charge neutral point seems to be an intrinsic property of the $Bi_2Se_3$ band structure, whereas its gradual decrease at higher Ca concentration is more due to disorder.

This observation suggests that once Ca concentration goes beyond a certain solubility limit, Ca in $Bi_2Se_3$ stops acting as a p-type dopant and instead starts to act as n-type. This is well understood from the very fact that most defects in $Bi_2Se_3$ behave as n-type ([56]West, et al., 2012). High level of Ca doping degrades not only the mobility but also the morphology, as can be seen in the Scanning Tunneling Microscope (STM) images of Figure 4-3(c) and (d). The STM images show that the morphology of $Bi_2Se_3$ films degrades noticeably at high Ca concentration. The re-entrant n-type behavior beyond a solubility limit of Ca doping explains why $Bi_2Se_3$ thin films without the buffer layer cannot be turned into p-type via compensation doping: high density of (n-type) interfacial defects requires proportionately high density of compensation dopant to reach p-type, but beyond a certain doping density, the compensation dopant starts to act as n- instead of p-type, making it impossible to convert the film into p-type.

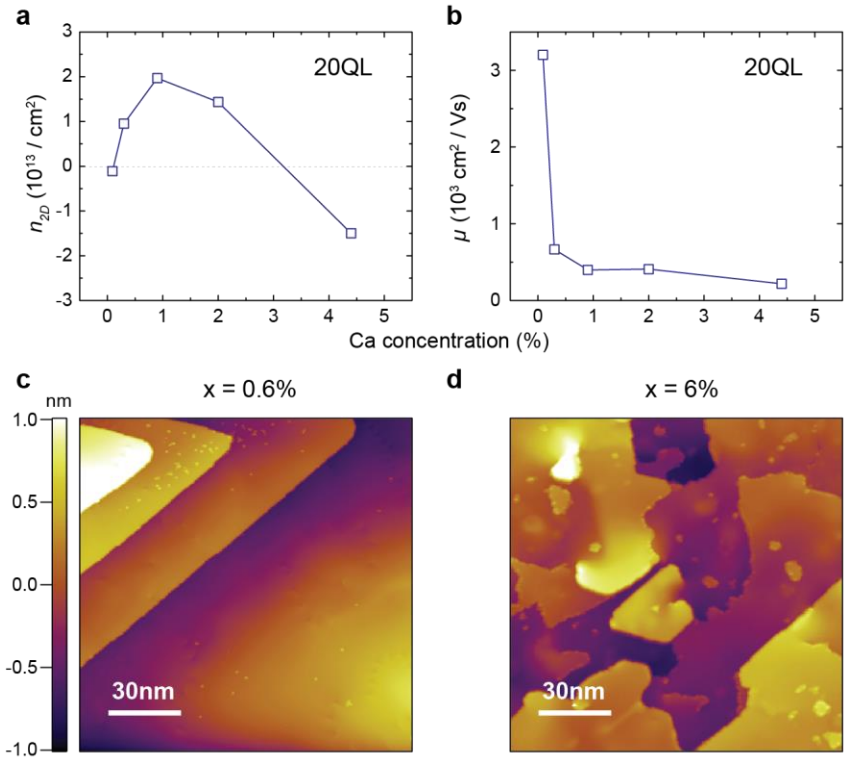


Figure 4-3. Transport properties and morphology comparison in Ca-doped $Bi_2Se_3$ films. (a) 2D sheet carrier density ($n_{2D}$) and (b) mobility ($\mu$) vs Ca concentration of the 20 QL, $Bi_2Se_3$ films on BIS-BL with Se capping. The carrier densities are taken from the 20 QL Hall effect data of Figure 4-2 at $B$ = 0 T. Data from severely nonlinear $R_{xy}(B)$ curves (0.13% and 0.17% of Ca) are excluded due to their uncertain carrier densities. The carrier type changes from n to p, and finally to n, while the mobility decreases sharply right around the n-p crossing point and gradually as the Ca concentration increases further. (c, d) STM topography images of Ca-doped $Bi_2Se_3$ films at (c) x = 0.6% and (d) x = 6%. The morphology degrades significantly at the higher Ca concentration, where the carrier type of the film reenters into the n regime from the p. (Adapted from [81]Moon, et al., 2018)

### 4.3.3 Tendency of sheet carrier density and mobility including non-linear regime from the two-carrier model

Using the two-carrier model in 3.1.4, we fit the n-p mixed curves and plot the results in Figure 4-4. Here, we use $n_1$, $n_2$, $\mu_1$, and $\mu_2$ as the fitting parameters with a constraint that the error in longitudinal resistance at $B = 0$ T be less than 3 %. In consequence, we perform "effective three parameter fitting" in $R_{xy}(B)$. As can be seen in Figure 4-4(a), which is for 20 QL $Bi_2Se_3$ film with 0.17 % of Ca, the fitting is generally quite good. Figure 4-4(b)-(i) show $n_{2D}$ and $\mu$ vs Ca concentration for four different thicknesses of $Bi_2Se_3$ films in the n-p mixed regime, as obtained from the two carrier fitting. Two features stand out from this fitting. First is that in the n-p mixed regime, the carrier density of the p-channel is always much larger than that of the n. Second, the mobility of the p-channel is always much smaller than that of the n. This observation is consistent with the conclusion in the main text, made without relying on the two carrier model: crossing the charge neutral point from n to p-type, the carrier density soars while the mobility plummets.

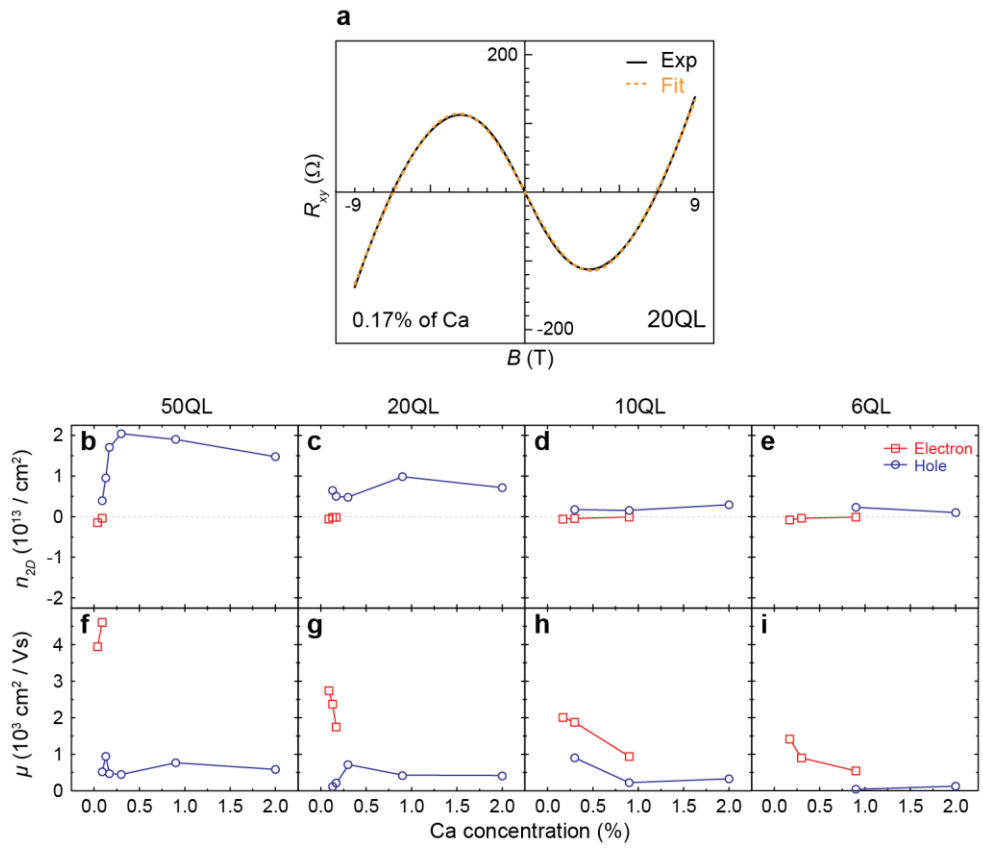


Figure 4-4. Two carrier model fitting of a 20 QL, n-p mixed, Ca-doped $Bi_2Se_3$ film grown on BIS-BL and capped by Se and complete data of sheet carrier density and mobility with n-p mix regime. (a) Black solid line shows the actual Hall measurement data, and orange dashed line shows the two carrier model fitting. (b-e) The $n_{2D}$ vs Ca concentration plots with data from the two carrier model fittings of 50 QL (b), 20 QL (c), 10 QL (d), and 6 QL (e), n-p mixed, Ca-doped $Bi_2Se_3$ films. (f-i) The $\mu$ vs Ca concentration plots with data from the two carrier model fittings of 50 QL (f), 20 QL (g), 10 QL (h), and 6 QL (i) films. (Adapted from [81]Moon, et al., 2018)

### 4.3.4 Comparison of alkaline earth elements as hole dopants: Mg, Ca, Sr, and Ba

Considering that the nominal valence of Bi in $Bi_2Se_3$ is 3+, any 2+ ions can be a candidate as a hole dopant for $Bi_2Se_3$. Therefore, we compared four alkaline earth elements, Mg, Ca, Sr, and Ba as a hole dopant for their doping efficiency up to 1 % in $Bi_2Se_3$ films: all these films are grown directly on $Al_2O_3$ (0001) substrates and capped by Se. The Hall effect measurements were carried out in an electro-magnet system with base temperature of 5 K and maximum magnetic field of ± 0.6 T.

The Hall effect data in Figure 4-5(a)-(d) show that Mg, Ca, and Sr are all similar in their hole doping efficiency, whereas Ba fails to act as a hole dopant. For Mg, Ca, and Sr, the $n_{2D}$ monotonically decreased to similar values at 1% doping: $4.8 \times 10^{12}$ /cm$^2$ for Mg, $4.1 \times 10^{12}$ /cm$^2$ for Ca, and $4.0 \times 10^{12}$ /cm$^2$ for Sr. On the other hand, the $n_{2D}$ for Ba-doped films rose to $1.3 \times 10^{14}$ /cm$^2$ at 1 % doping.

This doping efficiency difference can be partly understood from the comparison of the ionic sizes between the dopants and the Bi ion shown in Figure 4-5(e). The ionic radius of $Ca^{2+}$ (100 pm) is closest to that of $Bi^{3+}$ (103 pm), and that of $Ba^{2+}$ (135 pm) is farthest off ([115]Shannon, 1976). This ionic size comparison suggests that Ca is likely to be the least disruptive when substituted for Bi, and so in combination with the above Hall effect comparison study, we have chosen Ca as the hole dopant. However, as the above Hall effect study shows, Mg and Sr could be also as effective as Ca.

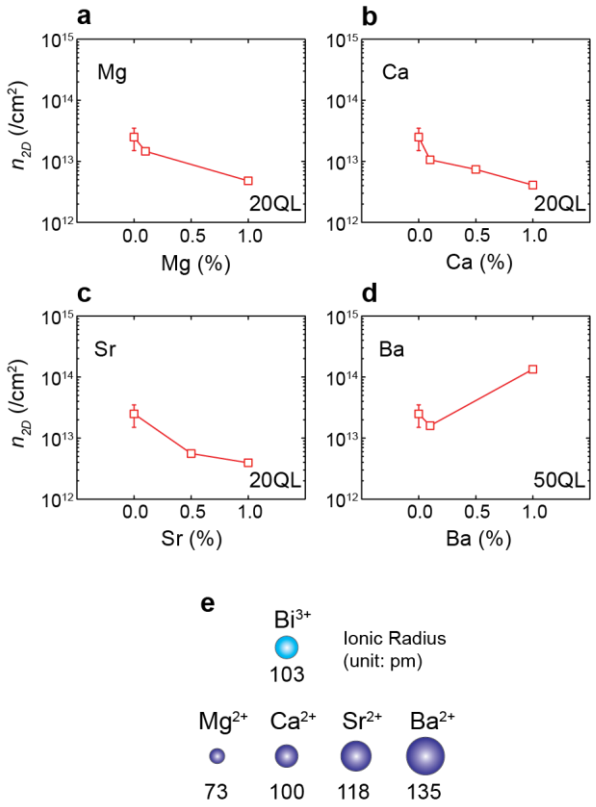


Figure 4-5. Sheet carrier density ($n_{2D}$) vs doping level (measured at 5 K) of alkali earth elements and comparison of ionic radiuses. (a-d) Mg (a), Ca (b) and Sr (c) doping in 20 QL, and Ba (d) doping in 50 QL of $Bi_2Se_3$ films grown directly on $Al_2O_3$ (0001) substrates and capped by Se. The $n_{2D}$ of pure $Bi_2Se_3$ films, $2.5 \times 10^{13}$ /cm$^2$, is included with an error bar of $\pm$ $1.0 \times 10^{13}$ /cm$^2$ in (a-d). (e) Comparison of ionic radiuses of $Bi^{3+}$ and dopants, $Mg^{2+}$, $Ca^{2+}$, $Sr^{2+}$, and $Ba^{2+}$. (Adapted from [81]Moon, et al., 2018)

## 4.4 Doping tunable quantum Hall effect

### 4.4.1 Quantum Hall effect in Ca-doped $Bi_2Se_3$ thin films

Finally, these p-type $Bi_2Se_3$ thin films have allowed us to take the first doping-dependent QHE study in TI materials. Although gate-dependent QHE have been observed in $(Bi_{1-x}Sb_x)_2Te_3$ thin films ([116]Yoshimi, et al., 2015) and in $BiSbTeSe_2$ single crystal flakes ([117]Xu, et al., 2016), and non-gated QHE in $Bi_2Se_3$ thin films ([68]Koirala, et al., 2015), doping-dependent QHE has not been available in any TI materials. Getting access to quantum regime in both n and p-doped TI films is critical for many topological quantum devices. For this study, we grew a series of 8 QL $Bi_2Se_3$ thin films with different Ca doping levels and measured their Hall effect up to a 34.5 T magnetic field with hand-patterned Hall bar geometry. In addition, we added $MoO_3$ as the main capping layer under the Se capping as shown in Figure 4-6(d), because $MoO_3$ helps reduce the Ca doping level to reach the p-type ([68]Koirala, et al., 2015). Figure 4-6(a) shows Ca-doping-dependent QHE in the $Bi_2Se_3$ films. The Hall resistance at high magnetic field is perfectly quantized at $R_{xy} = h/e^2 = 25.8$ kΩ with vanishing sheet resistance on the n-side up to 0.08% of Ca, indicating the emergence of a well-defined chiral edge channel at high magnetic fields. Here, it is notable that only the 1st Landau level (LL) plateau ($R_{xy} = h/(\nu e^2)$ with $\nu = 1$) is observable. The absence of higher level plateaus could be due to multiple factors such as the formation of non-chiral edge channels on the side surfaces ([118]Vafek, 2011), the presence of electronic puddles ([119]Beidenkopf, et al., 2011; [96]Dai, et al., 2016) and non-zero coupling between the transport channels of the top and bottom surface states ([90]Brahlek, et al., 2014).

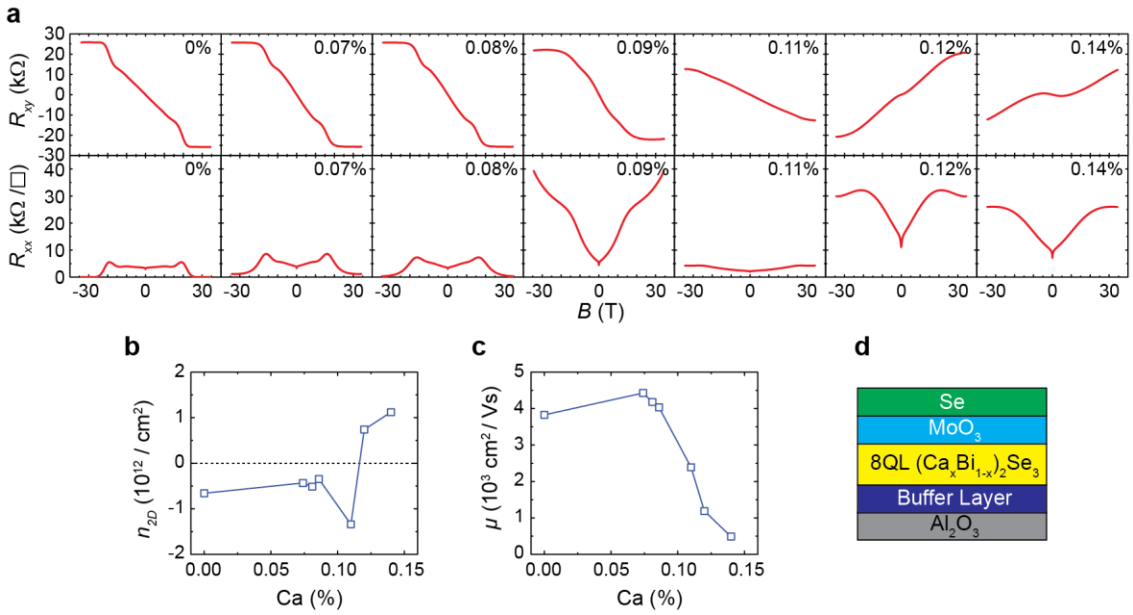


Figure 4-6. Ca doping-dependent transport properties, around the charge neutral point, of 8 QL $Bi_2Se_3$ films capped by $MoO_3$ and Se (at 300 mK). See Supporting Information Figure 4-7 and 4.4.3for a broader doping dependence of a similar set of films. (a) Magnetic field dependence of Hall ($R_{xy}$) and sheet ($R_{xx}$) resistance with different Ca doping levels. (b) 2D sheet carrier density ($n_{2D}$) and (c) mobility ($\mu$) with different Ca doping levels. We used $(dR_{xy}(B)/dB)_{B = 0T}$ for 0% ~ 0.11%, and $(dR_{xy}(B)/dB)_{B = 15, 20T}$ for 0.12% and 0.14% respectively, to extract net carrier density and mobility from the nonlinear Hall curves while avoiding the n-p mixing and the quantum Hall effects. Note that the mobility sharply decreases when the carrier type changes from n to p. (d) Schematic layer structure of the 8 QL Ca-doped $Bi_2Se_3$ films grown on the BIS-BL and capped by $MoO_3$ and Se. The pure $Bi_2Se_3$ data (0% of Ca, the leftmost data in a-c) are taken from Ref. ([68]Koirala, et al., 2015). (Adapted from [81]Moon, et al., 2018)

As Ca doping is increased toward the Dirac point (or, equivalently, zeroth LL), while the Hall resistance gradually deviates from the quantized value, the sheet magnetoresistance changes drastically even with minute change in doping. At 0.09%, the Hall resistance at high magnetic field deviates just slightly from the quantized value, but the sheet magnetoresistance soars from close-to-zero to a large insulating value (~40 kΩ) at high magnetic fields as the doping changes from 0.08 to 0.09% even if the resistance remains nearly the same at zero magnetic field. This nominally implies that the dissipationless edge state is breaking down while the rest of the sample is insulating under high magnetic field. However, as we get even closer to the zeroth LL at 0.11%, the Hall resistance starts to decrease over the entire magnetic field but the sheet magnetoresistance plummets: this nominally implies that the - otherwise insulating - sample is now becoming conducting. The overall decrease in Hall resistance at 0.11% is likely due to the n-p mixing as we discussed above in Figure 4-2. On the other hand, the presence of both insulating and conducting - in terms of sheet magnetoresistance - states right next to each other near the zeroth LL is puzzling, and it suggests that the zeroth LL harbors multiple unidentified states, which would require in-depth future studies, both experimentally and theoretically.

### 4.4.2 Absence of the quantum Hall effect in p-type $Bi_2Se_3$ thin films

With further increase of Ca doping to 0.12 and 0.14%, the majority carrier type now converts to p-type. There are a couple of features noticeable in the p-type films. First, the p-type carrier density grows quickly to ~$10^{12}$ /cm$^2$ (Figure 4-6(b)) with a noticeable signature of n-p mixing: pure p-regime can be achieved with much higher (~1%) level of Ca doping, but only with about an order of magnitude higher carrier density than the pure n-regime (next section below). Second, the signature of QHE is significantly degraded in the p-regime with the 1st LL barely observable only for 0.12%. Third, as can be seen in Figure 4-6(c), the mobility sharply decreases as soon as the majority carrier type changes from n to p-type: this is consistent with what we observed in Figure

4-3. Although Ca-doping can degrade the mobility to some extent, it cannot be the main factor at these low doping levels: note that the mobility in Figure 4-6(c) remains almost constant or even grows a little with Ca-doping in the n-regime until it reaches the charge neutral point, after which the mobility sharply decreases. This suggests that the mobility drop right on the p-side must be of intrinsic origin. Both the sharp drop in mobility and the sharp increase in carrier density on the p-side are very likely due to the band structure effect. According to the band diagram of $Bi_2Se_3$ ([40]Xia, Qian, Hsieh, Wray, et al., 2009), the Dirac point is very close to the bulk valence band and the surface band broadens noticeably on the p-side: both of these effects can account for the observed degradation of transport properties on the p-side of $Bi_2Se_3$ thin films. The near-absence of QHE and low mobility on the p-side of $Bi_2Se_3$ system is also consistent with the absence of Landau levels on the p-side as measured by a previous Scanning Tunneling Spectroscopy (STS) study ([120]Cheng, et al., 2010).

### 4.4.3 Transport properties of another set of 8 QL Ca-doped $Bi_2Se_3$ thin films capped by $MoO_3$ and Se, covering a broader doping range than Figure 4-6.

In Figure 4-6 of the main text, we showed that when the dominant carrier type in 8 QL Ca-doped $Bi_2Se_3$ thin films switches from n to p with increasing Ca doping, p-type films still had n-type minority carriers mixed together. In order to see how the transport properties evolve as we move deep into the p-regime, we grew another set of 8 QL Ca-doped $Bi_2Se_3$ thin films covering a broader doping range and present their transport properties in Figure 4-7. These samples are measured at 1.5 K and up to 9 T, instead of at 0.3 K and up to 34.5 T as in Figure 4-6. The samples that have overlapping doping levels with those in Figure 4-6 exhibit similar transport properties with slight variations: for example, while the most conducting sample at zero magnetic field in Figure 4-6 was 0.11%, the most conducting one in Figure 4-7 is 0.12%. On the p-side, there is n-p mixing at least up to 0.69%, and by the time the samples become pure p-type (0.86% or 1.1%, depending on the

view point), the p-type carrier density reaches ~3 × $10^{12}$ /$cm^2$, which is an order of magnitude larger than the n-type carrier density achieved on the pure n-type samples.

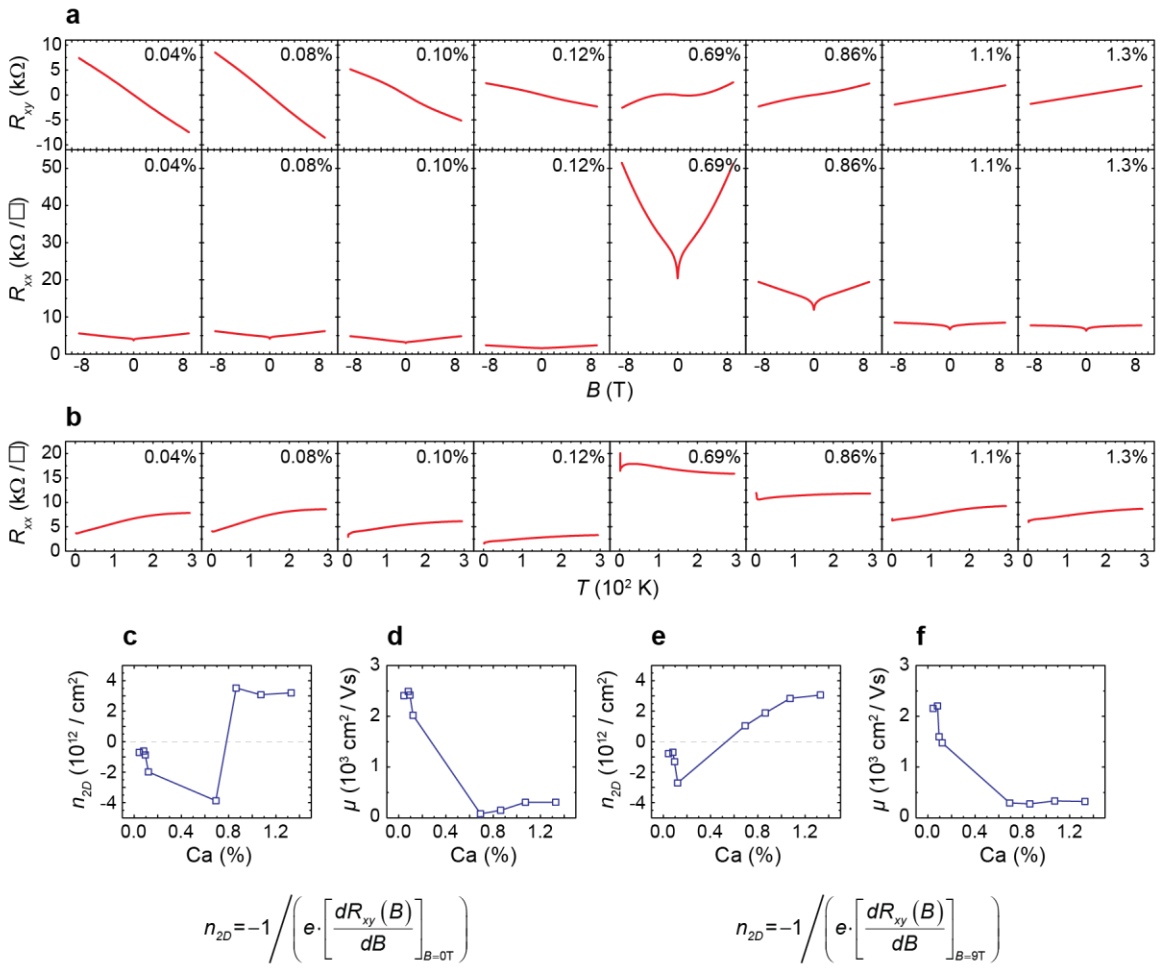


Figure 4-7. Transport properties of another set of 8 QL Ca-doped $Bi_2Se_3$ thin films, covering a broader doping range than Figure 4-6 of the main text, measured at or down to 1.5 K. (a) Ca doping dependence of $R_{xy}$ and $R_{xx}$ vs $B$. (b) Ca doping dependence of $R_{xx}$ vs $T$. (c, d) $n_{2D}$ (c) and $\mu$ (d) vs Ca concentration using $(dR_{xy}/dB)_{B=0T}$ to extract $n_{2D}$. (e, f) $n_{2D}$ (e) and $\mu$ (f) vs Ca concentration using $(dR_{xy}/dB)_{B=9T}$ to extract $n_{2D}$. (Adapted from [81]Moon, et al., 2018)

Whenever the Hall resistance is nonlinear, the carrier density cannot be trivially extracted from the Hall resistance curve. One way to get around this problem is to use a multi-carrier model as we did above in 4.3.3. However, considering that we cannot be sure about the valid number of conduction channels, such a fitting has its own limitations. In order to avoid any assumptions or biases, we plot two different sets of carrier densities and mobilities evaluated at two different magnetic fields in Figure 4-7(c)-(f). Generally, we take derivative of $R_{xy}(B)$ to extract $n_{2D}$ from $R_{xy}(B)$ as follows.

$$n_{2D} = -1 \Big/ \left( e \cdot \left[ \frac{dR_{xy}(B)}{dB} \right] \right) \tag{4-4}$$

If $R_{xy}(B)$ is linear, $n_{2D}$ is the same regardless of where the derivative is taken in $R_{xy}(B)$. However, if $R_{xy}(B)$ is nonlinear, then $n_{2D}$ value is dependent on where the derivative is taken. Here, we take two different points of the magnetic field for the derivative: 0 T and 9 T. The derivative at 0 T is dominated by $n_{2D}$ of the highest mobility channel. On the other hand, the slope at the high magnetic field limit approaches the net $n_{2D}$ (n-type + p-type): this can be seen from the two carrier model, Equation (3-15), in 3.1.4. Therefore, we take 9 T (the highest field here) as the high magnetic field limit and compare the slopes with the 0 T values. Figure 4-7(c)-(f) show that away from the n-p mixed regime, the quantities evaluated at the two magnetic fields are almost the same, whereas they are noticeably different in the n-p mixed regime. The increase in the n-type carrier density before the carrier type changes to p-type is not real and due to the fact that we have not reached high enough magnetic field to fully reveal the low mobility channel (here, p-type). Despite the uncertainty in the carrier densities of the n-p mixed regime, both Figure 4-7(d) and (f) show that the mobility drops sharply as the carrier type changes from n to p-type, which is consistent with what we observed in Figure 4-3, Figure 4-4, and Figure 4-6.

## 4.5 Conclusion

We have provided a solution to the long-standing hole doping problem and presented the first doping-dependent QHE study in $Bi_2Se_3$ thin films. We have shown that the previous failures of hole doping efforts in $Bi_2Se_3$ films are due to: first, large density of interfacial defects from the substrates, and second, neutralization of the dopant from the air. By suppressing the interfacial defects via the $(Bi_{0.5}In_{0.5})_2Se_3$ buffer layer and protecting the top surface with a capping layer, we were able to reach the hole regime of $Bi_2Se_3$ films down to the thinnest topological regime (6 QL) through compensation doping. In addition, in the doping dependent QHE study of 8 QL $Bi_2Se_3$ thin films we showed that the first (and only) Landau level is clearly observed on the electron side but quickly dissolves away on the hole side. Interestingly, at close proximity to the zeroth Landau level, we observed both the disintegration of the edge channel and the emergence of a conducting state, whose origins are unknown at the moment.

# CHAPTER 5. Ferromagnetic anomalous Hall effect in $Bi_2Se_3$ thin films

## 5.1 Introduction

The ordinary Hall effect (OHE) is the emergence of a transverse electrical potential difference due to the Lorentz force when an external magnetic field ($H$) is applied perpendicular to the direction of charge flow. The transverse electrical potential difference divided by the longitudinal current is called the Hall resistance ($R_{xy}$) as discussed in 3.1. Normally, the $R_{xy}$ grows linearly with the applied magnetic field and the slope is determined by the two-dimensional (2D) sheet carrier density ($n_{2D}$). In magnetic materials, however, the internal magnetism affects the charge motion and the Hall signal can significantly deviate from OHE, sometimes resulting in a hysteretic behavior as a function of $H$; this is called "anomalous" Hall effect (AHE) ([121]Nagaosa, et al., 2010). Although AHE is commonly observed in ferromagnetic conductors, AHE in magnetic topological insulators (TIs) is special in that it can lead to a quantum anomalous Hall effect (QAHE). Although QAHE was envisioned as early as 1988 ([3]Haldane, 1988), the first realistic material predicted to exhibit QAHE ([122]Yu, et al., 2010) was a magnetic TI, Cr-doped $Bi_2Se_3$ thin film ([38]H. Zhang, et al., 2009; [41]Hor, et al., 2009; [123]Hsieh, Xia, Wray, et al., 2009). However, QAHE has been observed only in Cr- and later V-doped $(Bi,Sb)_2Te_3$ thin films ([124]C.Z. Chang, et al., 2013; [125]Chang, et al., 2015; [126]Mogi, et al., 2015; [127]Feng, et al., 2016; [128]Ou, et al., 2017; [129]He, et al., 2014), and it has been challenging to introduce even ferromagnetism (FM) into $Bi_2Se_3$ thin films. The Hall effect measurement in Cr-doped $Bi_2Se_3$ thin films has exhibited only an amplification effect interpreted as paramagnetism without any hysteretic loops ([130]Zhang, et al., 2013). Although V-doped $Bi_2Se_3$ films show hysteretic Hall traces ([131]Zhang, et al., 2017), they were orders of magnitude smaller than the quantum value. There have been efforts to reveal the exact origin behind the weakness/absence of FM and AHE in V- and Cr-doped $Bi_2Se_3$ thin films ([132]Kim, et al., 2017;

[133]Chang, et al., 2014; [131]Zhang, et al., 2017), but a satisfactory consensus has not been achieved yet.

## 5.2 Comparison of positive and negative anomalous Hall effect

### 5.2.1 The characteristic shapes of quantum anomalous Hall effect

In order to better understand and specify the problems in the current study, we first compare the Hall traces of the QAHE with positive and negative anomalous Hall conductivity (AHC). Figure 5-1(a) shows the characteristic shape of all the observed QAHE so far, in both Cr- and V-doped $(Bi,Sb)_2Te_3$ thin films. In addition to the perfect quantization and the hysteresis, which are the two required features of the QAHE, another common notable feature is that the sign of the AHC is positive, with the slope of the hysteresis loop being positive ([124]C.Z. Chang, et al., 2013; [125]Chang, et al., 2015). Even when the hysteresis disappears above the Curie temperature, the zero-field slope still remains positive in all these cases. Moreover, the FM in V-doped $Bi_2Se_3$ exhibited also positive AHC ([131]Zhang, et al., 2017). Figure 5-1(b), on the other hand, shows the shape for a fictitious QAHE with a negative AHC. Such a shape has never been observed in QAHE so far, which has been a mystery.

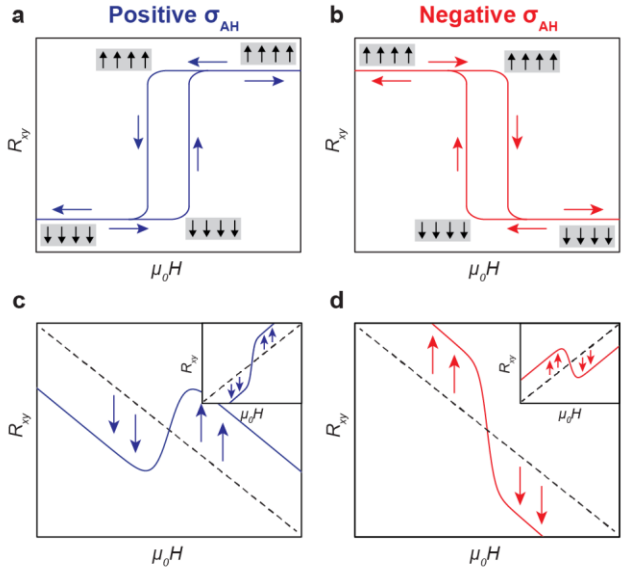


Figure 5-1. Schematic comparison of Hall effect curves for magnetically doped TIs. (a) Characteristic shape of QAHE curves of Cr- and V-doped $(Bi,Sb)_2Te_3$ films with positive AHC. The blue arrows show the direction of the field sweep. (b) The shape for a fictitious QAHE with negative AHC that would be expected for Cr-doped $Bi_2Se_3$ films. Magnetic ordering is shown by cartoons at the corresponding points of the curves, respectively. (c-d) Schematic illustrations of variations of Hall effect curves due to (c) positive and (d) negative AHC. The n-type Hall effect curves are shown by the dashed lines with a negative slope. (c) The positive AHC raises the curve on the positive side of the external magnetic field $H$, and lowers it on the opposite side as indicated by the blue arrows. (d) The negative AHC, on the contrary, lowers the curve on the positive side, and raises it on the other side. The insets show the same variations from a p-type Hall effect curve. (Adapted from [134]Moon, et al., 2019)

### 5.2.2 Anomalous Hall conductivity

When a system is close to having a FM phase transition, but is actually still on the paramagnetic side of the phase boundary, we may still expect a residual behavior in which the system shows a rapid but continuous change of the magnetization over some small region of $|H|$, with a saturating behavior for larger $|H|$. This behavior should also be reflected in the appearance of a nonlinear Hall conductivity of the kind shown in Figure 5-1(c) and (d). In this work, we continue to refer to such

a behavior as an "anomalous Hall conductivity" because of the strong nonlinearity, although we emphasize that the system does not display the AHE at zero field.

Figure 5-1(c) and (d) illustrate schematics of variations from an n-type Hall effect curve by positive and negative AHC. The negative slope of the dashed lines indicates the n-type charge carriers in the system. The positive AHC modifies the curve by raising the positive side of the magnetic field and lowering the opposite side, as shown in Figure 5-1(c). Conversely, the positive side of the magnetic field is pushed down by the negative AHC in parallel with the opposite side being pushed up as shown in Figure 5-1(d). The same effects appear in p-type curves as in the insets, respectively. Unlike the QAHE in Cr- and V-doped $(Bi,Sb)_2Te_3$ thin films, the Cr-doped $Bi_2Se_3$ thin films are so far reported to exhibit only paramagnetism with their AHC being negative without a hysteresis loop as in Figure 5-1(d) ([130]Zhang, et al., 2013). If it were to show QAHE, it should be of the negative type as depicted in Figure 5-1(b). This seemingly important feature has never been discussed before, not to mention that the origin behind this phenomenon remains unknown. This problem and its solution are the focus of the current study presented below.

## 5.3 Uniform Cr doping in $Bi_2Se_3$ and its problem

We first discuss the results for uniformly Cr-doped $Bi_2Se_3$ thin films in Figure 5-2. All the films used in the current study are grown on 20 QLs of $(Bi_{0.5}In_{0.5})_2Se_3$ (BIS in short) on 20 QLs of $In_2Se_3$ on $Al_2O_3(0001)$ substrates: this buffer layer was previously shown to work as an excellent template for $Bi_2Se_3$ thin films ([68]Koirala, et al., 2015; [80]Salehi, et al., 2016; [81]Moon, et al., 2018). The film structure is sketched in Figure 5-2(a). Figure 5-2(b) shows the Hall effect data for 5%, 7.5% and 10% of uniform Cr doping in 10 QL $Bi_2Se_3$ films. Two distinct effects of the uniform Cr doping in $Bi_2Se_3$ films can be seen in the data. First, it leads to an enhanced $R_{xy}$ with higher slopes at small magnetic fields, resulting in non-linear $R_{xy}(H)$ curves. This indicates that the Cr-doping has an amplification effect on the magnetic field being applied to the $Bi_2Se_3$ films, which is a signature of

paramagnetism. Second, it leads to a higher n-type carrier density as manifested in the reduced slope of the room-temperature $R_{xy}(H)$ data in the inset of Figure 5-2(b). The increased n-type carrier density with Cr doping is likely due to disorders, as can be seen in the degraded reflection high-energy electron diffraction (RHEED) images of heavily-Cr-doped $Bi_2Se_3$ films in Figure 5-2(e)-(h). It is well known that almost all defects in $Bi_2Se_3$ act as n-type dopants, thus increasing $n_{2D}$ of the inherent n-type carriers ([56]West, et al., 2012).

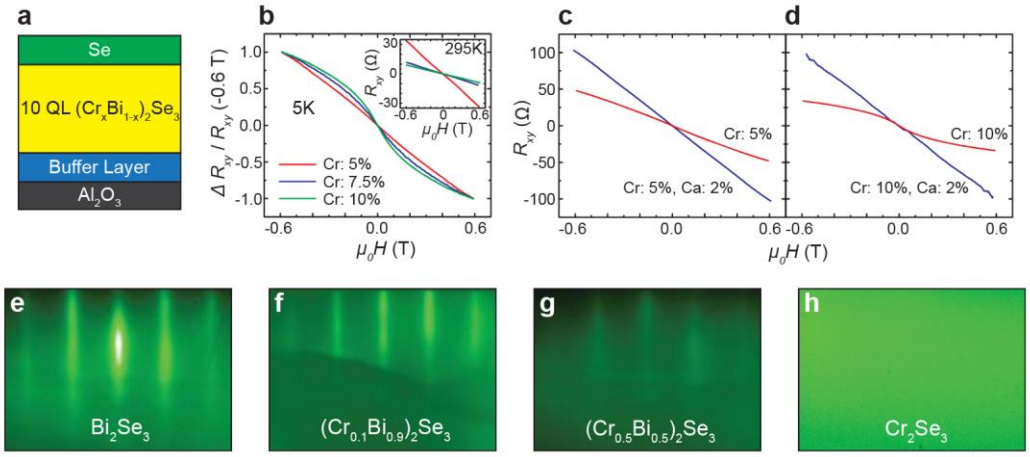


Figure 5-2. Hall effect data for uniformly Cr-doped $Bi_2Se_3$ films and related RHEED images. (a) Schematic of the layered structure of uniformly Cr-doped $Bi_2Se_3$ films (b) Hall effect data for 5%, 7.5% and 10% uniform Cr doping. $\Delta R_{xy}(H) / R_{xy}(-0.6\ \mathrm{T})$ is plotted instead of $R_{xy}(H)$ for simplicity. The inset shows the Hall effect results at room temperature. (c-d) Comparison of Hall effect data with and without Ca doping with (c) 5% and (d) 10% Cr doping. (e-h) RHEED images of (e) pure $Bi_2Se_3$; (f) 10% and (g) 50% Cr-doped $Bi_2Se_3$; and (h) $Cr_2Se_3$ films. As the Cr concentration increases, the RHEED pattern becomes faint, eventually vanishing at 100% of Cr. The dark areas in (f) and (g) are due to an artifact on the RHEED screen. (Adapted from [134]Moon, et al., 2019)

## 5.4 Solutions: magnetic modulation and charge compensation doping

### 5.4.1 Hypothesis for the lack of ferromagnetism in $Bi_2Se_3$ thin films

We hypothesize that there are two factors that give rise to the lack of FM in Cr-doped $Bi_2Se_3$ thin films. The first is the high Fermi level due to disorder from Cr doping and the second is the weakening of the topological character of $Bi_2Se_3$ by the lightness of Cr compared with Bi ([130]Zhang, et al., 2013). Regarding the first, studies of ferromagnetic Cr- or V-doped $(Sb,Bi)_2Te_3$ and V-doped $Bi_2Se_3$ films show that lowering the Fermi level generally enhances the AHE signal ([124]C.Z. Chang, et al., 2013; [131]Zhang, et al., 2017). Accordingly, it is reasonable to expect that lowering the Fermi level in Cr-doped $Bi_2Se_3$ films should also be helpful for inducing FM as the Fermi level falls into the mass gap of the surface Dirac cone. Considering that Ca-doping on the BIS-BL is known to suppress the n-type carriers ([81]Moon, et al., 2018), we grew two Cr-doped (5% and 10%) $Bi_2Se_3$ films with Ca compensation doping (2%) to see if lowering the Fermi level can induce the desired FM. Figure 5-2(c) and (d) provide the Hall effect data for these films at 5 K. Both films show increased slopes in $R_{xy}(H)$ with the Ca compensation doping, indicating that the n-type $n_{2D}$ is reduced with the Ca doping. However, FM AHE was not observed in either of these two cases. This suggests that reducing only the Fermi level may not be sufficient to induce FM in Cr-doped $Bi_2Se_3$ films.

### 5.4.2 Magnetic modulation doping

In order to overcome the second problem, the weakened topological nature of the $Bi_2Se_3$ films due to Cr-doping, we adopted the magnetic modulation doping scheme suggested by M. Mogi *et al* ([126]Mogi, et al., 2015) who succeeded in increasing the critical temperature for the QAHE through such a scheme. In a similar way, we have sandwiched an 8 QL (Cr-free) $Bi_2Se_3$ layer by two heavily (50%) Cr-doped QLs as shown in Figure 5-3(f). The intent of the surface engineering with the magnetic modulation doping is to maintain the full topological character of the bulk $Bi_2Se_3$ film

while relying on the outer two heavily-Cr-doped layers for the magnetism. The heavily Cr-doped top and bottom layers are insulating based on resistance measurements on a 50 QL $(Cr_{0.5}Bi_{0.5})_2Se_3$ film, which is non-measurably insulating even at room temperature. Consequently, we expect that the top and bottom layers provide the Cr-free $Bi_2Se_3$ layer with strong magnetism without contributing any conductance on their own. However, as shown in Figure 5-3(a), this magnetic modulation doping scheme alone does not lead to signatures of FM.

### 5.4.3 Ferromagnetic anomalous Hall effect in $Bi_2Se_3$ thin films

Lastly, we have combined the above two schemes: the Ca compensation doping, to lower the Fermi level, and the magnetic modulation doping, to protect the topological character of the film. This combined method has finally led to FM AHE with a small but clear hysteresis loop as shown in Figure 5-3(b). Interestingly, when the FM emerges in these surface-state-engineered Cr/Ca-doped $Bi_2Se_3$ thin films, the zero-field slope changes from negative to positive. In other words, the FM appears with a positive AHC while the uniformly Cr-doped $Bi_2Se_3$ thin films has shown negative AHC without FM signal. This corresponds to a transition from Figure 5-1(d) to Figure 5-1(c). We observed a similar positive AHC in both 1-8-1 QL and 1-6-1 QL films of $Ca_{0.04}(Cr_{0.5}Bi_{0.5})_{1.96}Se_3$ – $Ca_{0.04}Bi_{1.96}Se_3$ – $Ca_{0.04}(Cr_{0.5}Bi_{0.5})_{1.96}Se_3$ structure with only the outer most layers doped by 50% Cr for Bi as shown in Figure 5-4.

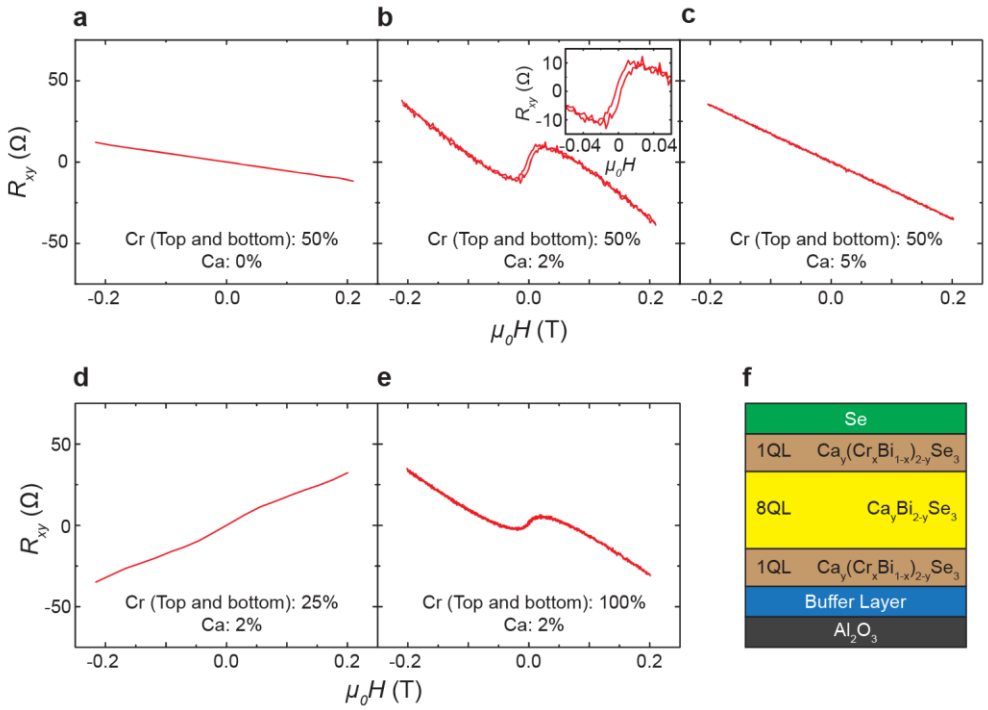


Figure 5-3. Hall effect data for surface-state-engineered Cr-doped $Bi_2Se_3$ films. (a-c) Hall effect data in the $Bi_2Se_3$ films with 50% of Cr doping only at the top and bottom layer layers, with (a) 0%, (b) 2% and (c) 5% of Ca doping. The inset of (b) presents zoomed-in data near zero magnetic field to show the hysteresis loop clearly. (d-e) Hall effect data in the $Bi_2Se_3$ films with (d) 25% and (e) 100% of Cr doping at the top and bottom layers, with 2% of Ca doping. (f) Schematic of the layered structure. (Adapted from [134]Moon, et al., 2019)

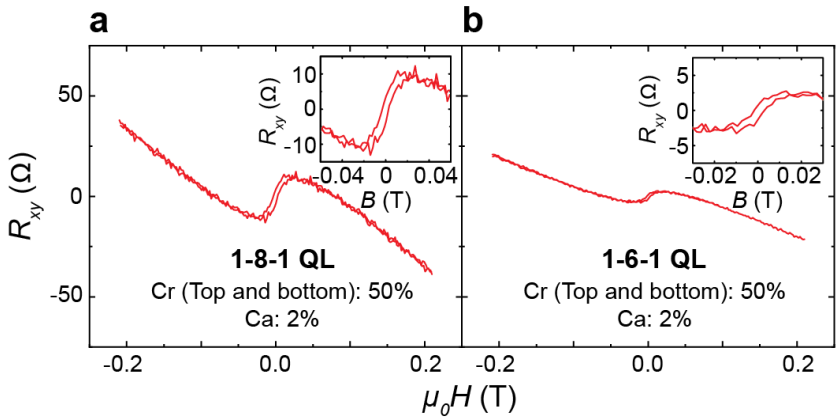


Figure 5-4. The anomalous Hall effect signals in the surface engineered films. Hysteresis loops observed in (a) 1-8-1 QL and (b) 1-6-1 QL structure of $Ca_{0.04}(Cr_{0.5}Bi_{0.5})_{1.96}Se_3$ – $Ca_{0.04}Bi_{1.96}Se_3$ – $Ca_{0.04}(Cr_{0.5}Bi_{0.5})_{1.96}Se_3$ films. (Adapted from [134]Moon, et al., 2019)

In Figure 5-3(c), we tried a higher Ca concentration to lower $n_{2D}$ further. However, the AHE signal vanished possibly due to too much disorder associated with the high Ca concentration ([81]Moon, et al., 2018). Figure 5-3(d) and (e) show Hall effect data for the surface-engineered films with identical thicknesses (1-8-1 QL) but with different Cr concentration. The film with Cr-25% and Ca-2% shows only p-type Hall effect without any hint of FM, while the other one with Cr-100% and Ca-2% shows a positive AHC, but without a clear hysteresis loop. The lack of the FM for Cr-25% and Ca-2% is probably due to too small content of Cr. The degraded AHE signal for Cr-100% and Ca-2% in Figure 5-3(e) as compared with that for Cr-50% and Ca-2% from Figure 5-3(b) is likely due to poor crystalline feature of the Cr-100% layer as can be seen in the RHEED image of Figure 5-2(e)-(h). These results suggest that FM in Cr-doped $Bi_2Se_3$ can develop only within a small window of the Cr and Ca concentrations even in this modulation scheme.

## 5.5 Theoretical explanations

These observations naturally lead to the following three critical questions concerning AHE in Cr-doped $Bi_2Se_3$. (1) Why is it particularly challenging to implement FM in $Bi_2Se_3$ compared with the telluride TIs such as $(Sb,Bi)_2Te_3$? (2) Why does the surface Cr doping help induce FM as compared with the homogeneous Cr doping? (3) Why is the sign of the AHC always positive when FM order appears? We will address each of three questions below in sequence.

### 5.5.1 Ferromagnetism in $Bi_2Se_3$

Let's first look into the first question. According to the free-energy argument of the original theoretical study ([122]Yu, et al., 2010), TI can exhibit FM order if $J_{eff}^2 - \chi_L^{-1}\chi_e^{-1} > 0$, where $J_{eff}$ is the effective exchange coupling strength between local magnetic moments and band electrons, and $\chi_L$ and $\chi_e$ are magnetic susceptibilities of the local magnetic moments and the band electrons, respectively. In order to satisfy this condition, we need large $J_{eff}$, large $\chi_L$ and large $\chi_e$. In the original theory, however, the authors focused mostly on $\chi_e$, and showed that magnetic TIs could become ferromagnetic because strong spin-orbit coupling (SOC) would substantially enhance $\chi_e$ through a so-called van Vleck mechanism ([135]Van Vleck, 1953). According to this picture, $Bi_2Te_3$ is more likely to become ferromagnetic than $Bi_2Se_3$ with the same level of magnetic doping because Te should provide stronger SOC than Se does, and this is consistent with the experimental observation ([130]Zhang, et al., 2013). However, the fact that Cr-doped $Bi_2Se_3$ is not ferromagnetic, contrary to the prediction, implies that the original theory was quantitatively insufficient.

Now the above argument comes to answer the second question. By keeping Cr only in the surface layers, two important conditions are satisfied. First, this keeps the SOC strength of the bulk of $Bi_2Se_3$ almost intact, thus maintaining reasonably high $\chi_e$. Second, it enhances $J_{eff}$ with surface states sitting right next to the magnetic ions providing stronger exchange coupling between the localized, magnetic electrons and the itinerant surface electrons via an RKKY type interaction

([136]Ruderman and Kittel, 1954). There has been debate in the literature as to whether the ferromagnetism observed in magnetic TIs is due to an RKKY ([137]Liu, et al., 2009) vs. a van Vleck mechanism ([122]Yu, et al., 2010; [138]C.-Z. Chang, et al., 2013; [130]Zhang, et al., 2013; [139]Li, et al., 2015), or both ([140]Kou, et al., 2013; [141]Wang, et al., 2018), or neither ([132]Kim, et al., 2017; [133]Chang, et al., 2014). Our current study suggests that it may not be one or the other, but both, with RKKY enhancing $J_{eff}$ and van Vleck enhancing $\chi_e$ in the $Bi_2Se_3$ thin films.

### 5.5.2 Positive anomalous Hall effect: mass-gap analysis from a tight binding study

Before moving on to a theoretical investigation to resolve the questions above, we first note that the positive or negative AHC is directly related to the Berry phase whenever the AHC is quantized, according to

$$\sigma_{\mathrm{AH}} = \frac{e^2}{h}(-C) \tag{5-1}$$

Here $C$ is the Chern number; by the relation between the AHC and the Chern number, $C = -1$ leads to a positive AHC as in Figure 5-1(a), and conversely, $C = +1$ results in a negative AHC, as in Figure 5-1(b). In this regard, $C = -1$ is the usual sign in Cr- or V-doped $(Bi,Sb)_2(Te,Se)_3$ ; the uniformly Cr-doped $Bi_2Se_3$ thin films are exceptional in that they show a negative AHC, indicating $C = +1$. We will refer to this exceptional case as displaying a 'sign anomaly' from now on.

For the numerical calculations, first-principles calculations are carried out by using VASP ([142]Kresse and Furthmüller, 1996a; [143]1996b) and wannierized by using the VASP-WANNIER90 ([144]Mostofi, et al., 2014) interface to arrive at a tight-binding description of first-principles quality. The pseudopotential is of the projector-augmented-wave type as implemented in VASP ([145]Blöchl, 1994; [146]Kresse and Joubert, 1999). The Perdew-Burke-Ernzerhof approximation for solid (PBEsol) ([147]Perdew, et al., 2008) is employed to describe the generalized gradient approximation type of exchange-correlation functional. We choose an energy cutoff of 300 eV and the Brillouin zone is sampled with k-point grids of size $10 \times 10 \times 10$ for pristine $Bi_2Se_3$ and $4 \times 4 \times 1$ for $\sqrt{3} \times \sqrt{3} \times$

1 hexagonal supercell structures in 3 QLs with Cr substitution of Bi. Atomic spin-orbit-coupling is included to Bi *p* and Se *p* orbital basis after wannier projection. Zeeman field, $H_{ZM} = \frac{1}{2}\Delta_{ZM}\sigma_{\hat{n}}$ is applied along (111) direction, normal to the layers.

In order to understand the consistent positive AHC in the Cr- or V-doped $(Bi,Sb)_2(Te,Se)_3$ system, except for the sign anomaly in the uniformly Cr-doped case, we study a tight-binding model for 8 QLs of $Bi_2Se_3$ with a spatially modulated Zeeman field introduced to represent the leading effect of the Cr doping. A preliminary signature of the transition to the QAH phase induced by the Zeeman field is a mass-gap acquisition of the surface Dirac cone.

Figure 5-5(a) shows the mass gap (displayed by colors) of 8 QLs of $Bi_2Se_3$ as a function of the Zeeman fields $\Delta_{Bi}$ and $\Delta_{Se}$ independently applied to the *p* orbitals of the Bi (*x*-axis) and Se (*y*-axis). We find our computed Dirac cone splittings $E_g$ are well described by the formula

$$E_g = \min | E_{mag} \pm E_0 | , \tag{5-2}$$

where $E_0 = 19$ μeV is the gap induced by the interaction between top and bottom surfaces, and

$$E_{mag} = \chi_{Bi}\ \Delta_{Bi} + \chi_{Se}\,\Delta_{Se} \tag{5-3}$$

with $\chi_{Bi} = 0.420$ and $\chi_{Se} = -0.034$ being the mass-gap susceptibilities defined as the ratios of the induced mass gap to the applied Zeeman field. Two topological transitions then occur when $E_g = 0$, with the film as a whole exhibiting Chern numbers of $C = -1$, 0, and +1 for $E_{mag} > E_0$, $|E_{mag}| < E_0$, and $E_{mag} < -E_0$, respectively.

We then computed appropriate values of $\Delta_{Bi}$ and $\Delta_{Se}$ by extracting the spin-dependent site energy shifts from a Wannierized model extracted from the first-principles calculations. The results are shown in Figure 5-5(c), where the Zeeman splittings are significant only inside the Cr doped QL. Assuming dilute (5.6%) and isotropic Cr doping, the values of $\Delta_{Bi} = 31$ meV and $\Delta_{Se} = -6$ meV are determined as average Zeeman splittings of each type of atom. In principle, $\chi_{Se} = 1/3(\chi_{Se1} + 2\chi_{Se2})$, where Se1 and Se2 refer to the central and the two outer Se atoms, respectively. However, the mass-gap susceptibility of Se1 is negligible ($|\chi_{Se1}| < 0.2\ |\chi_{Se2}|$), so the Zeeman splitting of Se1 is not

included. Interestingly, the estimated Zeeman splittings for Bi and Se have opposite signs, i.e., positive and negative respectively. However, both atoms act with the same sign in determining the Chern number because the sign of the two χ values are also opposite. The resulting Chern number of −1 reproduces the usual sign for magnetically doped TIs, but the sign anomaly for uniformly-doped Cr is not explained.

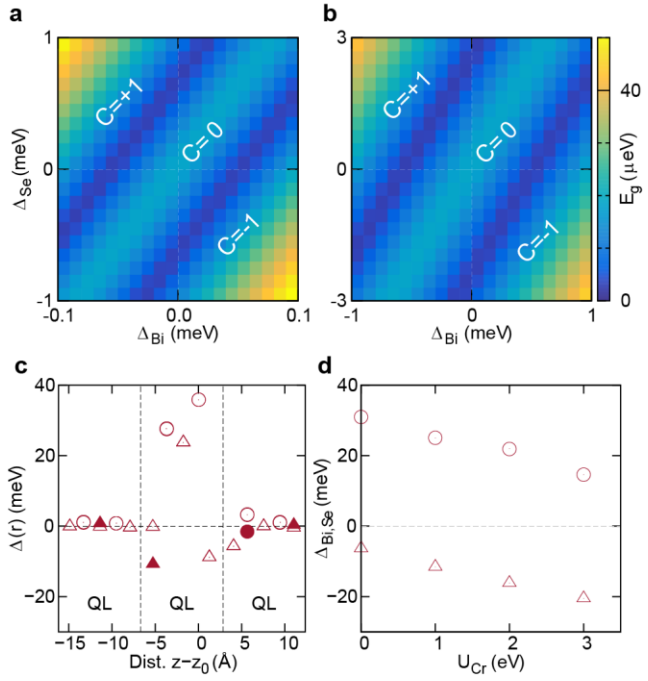


Figure 5-5. Model study of the QAH phase of Cr-doped $Bi_2Se_3$. Calculated Dirac cone mass gap for 8 QLs of $Bi_2Se_3$ under Zeeman field on Bi and Se atoms for (a) uniform field (homogeneous doping), and (b) proximity field (modulation doping). The Zeeman field on the Bi (Se) site induces a Chern number of −1 (+1) in either type of field distribution. (c) Calculated Zeeman splitting of 3 QLs of $Bi_2Se_3$ in a $\sqrt{3} \times \sqrt{3} \times 1$ hexagonal supercell structure with $z = z_0$ indicating the Cr atom location. Closed symbol denotes the atom being located at the same coordinate on *xy* plane as the Cr atom. (d) Average Zeeman splittings of Bi and Se atoms for each Hubbard *U* applied to the Cr *d* orbital basis. Circles (triangles) represent Bi (Se) atoms. (Adapted from [134]Moon, et al., 2019)

In order to simulate this exceptional case, a surface proximity Zeeman field $H = \frac{1}{2}\Delta_{Bi,Se}\sigma_z \, exp\left(-\frac{z}{d}\right)$ is considered, where $\sigma_z$ is the pauli matrix, $z$ is the depth below the surface, and $d$ = 4 Å is the decay length. Figure 5-5(b) shows the mass gap of 8 QLs under such a proximity Zeeman field, showing a similar QAH phase boundary as compared with the uniform doping case, with the right bottom corner exhibiting a Chern number of −1. Within these theoretical approximations, then, we still find no critical differences between the uniform and modulation doping cases.

### 5.5.3 Sign reversal problem of anomalous Hall conductivity

One thing to notice in Figure 5-5(a) and (b) is that the Dirac-cone mass gap is calculated to be about one order of magnitude more sensitive to a Zeeman field applied on the Bi sites than that on the Se sites. In other words, the mass gap is mostly determined by the Zeeman splitting of the Bi atoms, implying that a sign reversal in the AHC occurs via an antiferromagnetic coupling (i.e., negative Zeeman field) on the Bi atom. Figure 5-5(d), however, shows the obtained Zeeman field of Bi being positive within the considered circumstances. The other way to access the negative AHC is to tune the Zeeman-field mass-gap susceptibility on each atom, where the mass-gap susceptibility is defined as a ratio of the induced mass gap to the applied Zeeman field on that site.

For this reason, we test two factors which can affect the mass-gap susceptibility in the uniform doping case: (1) weakening the strength of the spin-orbit coupling, and (2) varying the Dirac cone position in energy. For the first factor, the effective SOC of Bi may diminish because of the substitutional doping of Cr ([148]Ghasemi, et al., 2016). However, we find that the mass-gap susceptibility to Bi is enhanced with decreasing SOC strength, weakening this effect.

The other potential origin is the energy position of the surface Dirac cone in the vicinity of the valence bands. The Bi-dominant orbital character of the valence bands can be the reason for the order-of-magnitude larger mass-gap susceptibility of Bi. When we artificially apply an additional

surface potential, lifting the energy of the top-surface Dirac cone by 100 meV while leaving the bottom-surface Dirac cone unshifted, the result is shown in Figure 5-6(a). Upon the shift of the Dirac cone, the QAH phase boundary is calculated as in Figure 5-6(b) and (c), showing the mass gap of the top and bottom surface Dirac cones, respectively. The bottom-surface Dirac cone exhibits an almost identical phase boundary as for the previous case of Figure 5-5(a). The boundary of the top-surface Dirac cone, however, is quite different. It displays a counter-clockwise rotation, and the top-right corner now has a negative Chern number. By applying a positive Zeeman field solely on the Se site, one can induce a negative (positive) AHC on the top (bottom) surface Dirac cone, implying opposite susceptibility of the two Dirac cones to the Se Zeeman field. Figure 5-6(d) shows the mass-gap susceptibility as a function of the Dirac cone shift, and a sign reversal of the Se susceptibility is found near 30 meV as marked with an arrow. The figure also shows that the susceptibility amplitudes of Bi and Se are interchanged beyond a Dirac cone shift of 200 meV. The boundary rotation demonstrates one way to flip the sign of the AHC, even with fixed Zeeman fields, that can occur via surface band bending.

We therefore speculate that the half Cr-doped $Bi_2Se_3$ QL at the top and bottom of the 8 pristine QLs in the modulation doping case could behave as a padding layer causing distinct band bending effects in the two doping cases. For $Bi_2Te_3$, the surface Dirac cone is known to be buried in the valence bands, and this may enforce a negligible mass-gap susceptibility for Te, resulting in the usual Chern number of –1. In the $Bi_2Se_3$ case, however, the more exposed Dirac cone can be more sensitive to the Zeeman splitting of the Se site.

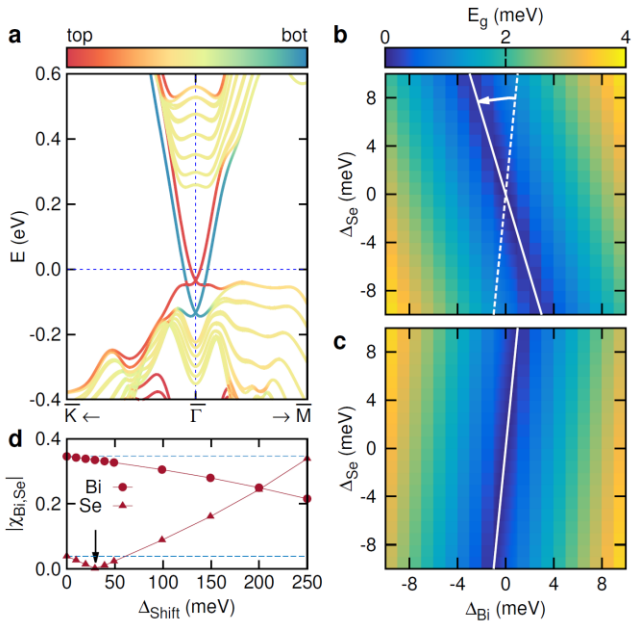


Figure 5-6. Effect of band banding on the Dirac-cone mass-gap susceptibility with respect to the Zeeman field. (a) Band structure with two surface Dirac cones, such that the top surface exhibits a band-banding effect. (b) and (c) Calculated Dirac cone mass gap for top and bottom surfaces, respectively. The shift of the Dirac cone with energy changes the mass-gap susceptibility to the Zeeman field, causing a rotation of the gap-closure phase boundary. (d) Mass-gap susceptibility of the top surface Dirac cone as a function of Dirac cone energy shift. Horizontal dashed lines denote the reference susceptibility of the bottom surface Dirac cone. (Adapted from [134]Moon, et al., 2019)

## 5.6 Conclusion

We have achieved the FM AHE in Cr-doped $Bi_2Se_3$ thin films through a combination of magnetic-modulation doping and Fermi level tuning. Interestingly, the emergent FM AHE shows a positive AHC, which is consistent with the previous studies in Cr- or V-doped $(Bi,Sb)_2Te_3$ and V-doped $Bi_2Se_3$ films. The successfully introduced FM is explained by qualitative considerations. The emergence of the positive AHC was studied with the theoretical investigation of mass-gap susceptibility and a first-principles method.

# CHAPTER 6. Epilogue

## 6.1 Review of the results

In CHAPTER 4, we succeeded in achieving p-type $Bi_2Se_3$ thin films down to the thinnest topological regime (6 QLs). This was possible because we successfully suppressed with incorporating the BIS-BL scheme as a solution to the long-standing hole doping problem. The previous failures of the hole doping efforts in $Bi_2Se_3$ films stem from two factors: first, high density of interfacial defects from the growth directly on the substrates, and second, neutralization of the dopant from the air. Suppressing the interfacial defects via the $(Bi_{0.5}In_{0.5})_2Se_3$ buffer layer and protecting the top surface with a Se capping layer, we were eventually able to enter the p regime of thin $Bi_2Se_3$ films through compensation doping with Ca. Thanks to the achievement, we were also able to perform the first doping-dependent QHE study in $Bi_2Se_3$ thin films. In the study with 8 QL $Bi_2Se_3$ thin films, we observed that the first (and only) Landau level clearly appears on the electron side but quickly vanishes away on the hole side. Interestingly, at close proximity to the zeroth Landau level, we observed both the disintegration of the edge channel and the emergence of a conducting state, whose origins are still unknown.

In CHAPTER 5, we have successfully achieved the FM AHE in Cr-doped $Bi_2Se_3$ thin films through a combination of magnetic-modulation doping and chemical Fermi level tuning. Interestingly, the emergent FM AHE exhibits a positive AHC, which is consistent with the previous studies in Cr- or V-doped $(Bi,Sb)_2Te_3$ and V-doped $Bi_2Se_3$ films. The successfully introduced FM is explained by qualitative considerations of the free energy argument reported in 2010 ([122]Yu, et al., 2010). The emergence of the positive AHC was studied with the theoretical investigation of mass-gap susceptibility. The results from the theoretical consideration are consistent with our observation as well as all the QAH effect so far. A further study implies that raising up the Dirac cone in energy in consideration of surface band bending effects could cause the observed sign reversal of the AHC in uniformly Cr-doped $Bi_2Se_3$. The rotation of the phase boundary resulting

from band bending suggests a novel transistor mechanism where gating voltage controls the sign of the Chern number via the surface Dirac cone energy, causing a sign flip in the transverse current. Our study also showcases how the combination of materials engineering and theoretical considerations can lead not only to otherwise inaccessible electronic properties but also to a deeper understanding of the underlying mechanism.

## 6.2 Future work

The research field in topological materials is vast, and have numerous unknown properties. We still need to deepen our understanding of novel physics in topological materials, which usually involves studying the role of the surface or edge states. The valuable schemes which have been dealt with in this dissertation should be used in the next stage.

The research field in topological superconductivity (TSC) has been rapidly growing, and it became one of the most interesting research areas due to the potential application to fault-tolerant quantum computation using so-called Majorana Fermions. One simple approach to TSC is to exploit the proximity effect of TI-SC structure. In 2016, Josephson interference in HgTe (2D TI) – Al and Nb SCs was reported ([149]Hart, et al., 2016), and more recently, the phase-modulated effects was observed in the same combination ([150]Ren, et al., 2018). Undoubtedly, the investigation of 3D TI-SC structures will be the next generation of this research path in TSC. Study of various materials of properly designed TI-SC would have to be performed. While the previous generation of TI thin films was known to have the parasitic bulk contribution to electrical conduction, it can now be completely removed through verified growth techniques. In addition, the carrier types (electron or hole) can also be changed via charge compensation doping with buffer layer engineering. The investigations of the various kinds of TIs in combination with SCs will provide a greater understanding of the TSC. Furthermore, utilizing magnetic TIs would also be interesting because the magnetically doped $(Bi,Sb)_2(Te,Se)_3$ thin films can even exhibit quantized anomalous Hall

(QAH) effects, and a different tendency could be expected in Josephson junctions with changing phases. For these aforementioned reasons, advanced transport studies would have to be done with various conditions and geometries in the TI-SC structures.

# REFERENCES


1. Drude, P., Zur Elektronentheorie der Metalle. *Ann. Phys. (Leipzig)*, **1**, 566, 1900.

2. Moore, J.E. and Balents, L., Topological invariants of time-reversal-invariant band structures. *Physical Review B*, **75**(12), 121306, 2007.

3. Haldane, F.D.M., Model for a quantum hall effect without landau levels: Condensed-matter realization of the 'parity anomaly'. *Physical Review Letters*, **61**(18), 2015–2018, 1988.

4. Klitzing, K. v., Dorda, G. and Pepper, M., New Method for High-Accuracy Determination of the Fine-Structure Constant Based on Quantized Hall Resistance. *Physical Review Letters*, **45**(6), 494–497, 1980.

5. Weis, J. and Klitzing, K. Von, Metrology and microscopic picture of the integer quantum Hall effect. *Philosophical Transactions of the Royal Society A: Mathematical, Physical and Engineering Sciences*, **369**(1953), 3954–3974, 2011.

6. Landau, L., Diamagnetismus der Metalle. *Zeitschrift für Physik*, **64**(9), 629–637, 1930.

7. Halperin, B.I., Quantized Hall conductance, current-carrying edge states, and the existence of extended states in a two-dimensional disordered potential. *Physical Review B*, **25**(4), 2185–2190, 1982.

8. Vanderbilt, D., *Berry Phases in Electronic Structure Theory*. Cambridge University Press. 2018.

9. Griffiths, D.J., *Introduction to Quantum Mechanics*. Pearson international edition. Pearson Prentice Hall. 2005.

10. Berry, M. V., Quantal Phase Factors Accompanying Adiabatic Changes. *Proceedings of the Royal Society A: Mathematical, Physical and Engineering Sciences*, **392**(1802), 45–57, 1984.

11. Laughlin, R.B., Quantized Hall conductivity in two dimensions. *Physical Review B*, **23**(10), 5632–5633, 1981.

12. Aharonov, Y. and Bohm, D., Significance of Electromagnetic Potentials in the Quantum Theory. *Physical Review*, **115**(3), 485–491, 1959.

13. Thouless, D.J., Kohmoto, M., Nightingale, M.P. and den Nijs, M., Quantized Hall Conductance in a Two-Dimensional Periodic Potential. *Physical Review Letters*, **49**(6), 405–408, 1982.

14. Avron, J.E., Osadchy, D. and Seiler, R., A topological look at the Quantum Hall effect. *Physics Today*, **56**(8), 38–42, 2003.

15. Kane, C.L. and Mele, E.J., Z 2 Topological Order and the Quantum Spin Hall Effect. *Physical Review Letters*, **95**(14), 146802, 2005a.

16. Hasan, M.Z. and Kane, C.L., Colloquium: Topological insulators. *Reviews of Modern Physics*, **82**(4), 3045–3067, 2010.

17. Hirsch, J.E., Spin Hall Effect. *Physical Review Letters*, **83**(9), 1834–1837, 1999.

18. Dyakonov, M.I. and Perel, V.I., Possibility of orienting electron spins with current. *Sov. Phys. JETP Lett.*, **13**, 467, 1971a.

19. Dyakonov, M.I. and Perel, V.I., Current-induced spin orientation of electrons in semiconductors. *Physics Letters A*, **35**(6), 459–460, 1971b.

20. Bakun, A.A., Zakharchenya, B.P., Rogachev, A.A., Tkachuk, M.N. and Fleisher, V.G., Detection of a surface photocurrent due to electron optical orientation in a semiconductor. *Sov. Phys. JETP Lett.*, **40**, 1293, 1984.

21. Hosten, O. and Kwiat, P., Observation of the spin hall effect of light via weak measurements. *Science*, **306**, 1910–1913, 2004.

22. Wunderlich, J., Kaestner, B., Sinova, J. and Jungwirth, T., Experimental observation of the spin-hall effect in a two-dimensional spin-orbit coupled semiconductor system. *Physical Review Letters*, **94**(4), 047204, 2005.

23. Anderson, P.W., Absence of Diffusion in Certain Random Lattices. *Physical Review*, **109**(5), 1492–1505, 1958.

24. Lee, P.A. and Ramakrishnan, T. V., Disordered electronic systems. *Reviews of Modern Physics*, **57**(2), 287–337, 1985.

25. Kane, C.L. and Mele, E.J., Quantum Spin Hall Effect in Graphene. *Physical Review Letters*, **95**(22), 226801, 2005b.

26. Büttiker, M., Absence of backscattering in the quantum Hall effect in multiprobe conductors. *Physical Review B*, **38**(14), 9375–9389, 1988.

27. Pankratov, O.A., Pakhomov, S.V. and Volkov, B.A., Supersymmetry in heterojunctions: Band-inverting contact on the basis of $Pb_{1-x}Sn_xTe$ and $Hg_{1-x}Cd_xTe$. *Solid State Communications*, **61**(2), 93–96, 1987.

28. Bernevig, B.A. and Zhang, S.-C., Rapid immunotyping of Chlamydia trachomatis with monoclonal antibodies in a solid-phase enzyme immunoassay. *Physical Review Letters*, **96**, 106802, 2006.

29. Dornhaus, R., Nimtz, G. and Schlicht, B., *Narrow-Gap Semiconductors*. Springer Tracts in Modern Physics. Berlin, Heidelberg: Springer Berlin Heidelberg. 1983.

30. Bernevig, B.A., Hughes, T.L. and Zhang, S.C., Quantum spin Hall effect and topological phase transition in HgTe quantum wells. *Science*, **314**(5806), 1757–61, 2006.

31. König, M., Wiedmann, S., Brüne, C., Roth, A., Buhmann, H., Molenkamp, L.W., Qi, X.-L. and Zhang, S.-C., Quantum spin hall insulator state in HgTe quantum wells. *Science (New York, N.Y.)*, **318**(5851), 766–70, 2007.

32. Qi, X.L. and Zhang, S.C., The quantum spin Hall effect and topological insulators. *Physics Today*, **63**(1), 33–38, 2010.

33. Fu, L. and Kane, C.L., Topological insulators with inversion symmetry. *Physical Review B*, **76**(4), 045302, 2007.

34. Roy, R., Topological phases and the quantum spin Hall effect in three dimensions. *Physical Review B*, **79**(19), 195322, 2009.

35. Hsieh, D., Qian, D., Wray, L., Xia, Y., Hor, Y.S., Cava, R.J. and Hasan, M.Z., A topological Dirac insulator in a quantum spin Hall phase. *Nature*, **452**(7190), 970–974, 2008.

36. Shuichi Murakami, Phase transition between the quantum spin Hall and insulator phases in 3D: emergence of a topological gapless phase. *New Journal of Physics*, **9**(9), 356, 2007.

37. Moore, J., The next generation. *Nature Physics*, **5**(6), 378–380, 2009.

38. Zhang, H., Liu, C.-X., Qi, X.-L., Dai, X., Fang, Z. and Zhang, S.-C., Topological insulators in $Bi_2Se_3$ $Bi_2Te_3$ and $Sb_2Te_3$ with a single Dirac cone on the surface. *Nature Physics*, **5**(6), 438–442, 2009.

39. Wyckoff, R.W.G., *Crystal structures. vol. 2*. New York, NY: Wiley. 1964.

40. Xia, Y., Qian, D., Hsieh, D., Wray, L., Pal, A., Lin, H., Bansil, A., Grauer, D., Hor, Y.S., Cava, R.J. and Hasan, M.Z., Observation of a large-gap topological-insulator class with a single Dirac cone on the surface. *Nature Physics*, **5**(6), 398–402, 2009.

41. Hor, Y.S., Richardella, A., Roushan, P., Xia, Y., Checkelsky, J.G., Yazdani, A., Hasan, M.Z., Ong, N.P. and Cava, R.J., P-type $Bi_2Se_3$ for topological insulator and low-temperature thermoelectric applications. *Physical Review B*, **79**(19), 195208, 2009.

42. Hsieh, D., Xia, Y., Qian, D., Wray, L., Dil, J.H., Meier, F., Osterwalder, J., Patthey, L., Checkelsky, J.G., Ong, N.P., Fedorov, A. V, Lin, H., Bansil, A., Grauer, D., Hor, Y.S., Cava, R.J. and Hasan, M.Z., A tunable topological insulator in the spin helical Dirac transport regime. *Nature*, **460**, 1101, 2009.

43. Chen, Y.L., Analytis, J.G., Chu, J.-H., Liu, Z.K., Mo, S.-K., Qi, X.L., Zhang, H.J., Lu, D.H., Dai, X., Fang, Z., Zhang, S.C., Fisher, I.R., Hussain, Z. and Shen, Z.-X., Experimental realization of a three-dimensional topological insulator, $Bi_2Te_3$. *Science (New York, N.Y.)*, **325**(5937), 178–181, 2009.

44. Hsieh, D., Xia, Y., Qian, D., Wray, L., Meier, F., Dil, J.H., Osterwalder, J., Patthey, L., Fedorov, A. V, Lin, H., Bansil, A., Grauer, D., Hor, Y.S., Cava, R.J. and Hasan, M.Z., Observation of time-reversal-protected single-dirac-cone topological-insulator states in $Bi_2Te_3$ and $Sb_2Te_3$. *Physical Review Letters*, **103**(14), 146401, 2009.

45. Xia, Y., Qian, D., Hsieh, D., Shankar, R., Lin, H., Bansil, A., Fedorov, A. V., Grauer, D., Hor, Y.S., Cava, R.J. and Hasan, M.Z., Topological Control: Systematic control of topological insulator Dirac fermion density on the surface of $Bi_2Te_3$. arXiv:0907.3089, 2009.

46. Kim, Y.S., Brahlek, M., Bansal, N., Edrey, E., Kapilevich, G.A., Iida, K., Tanimura, M.,

Horibe, Y., Cheong, S.W. and Oh, S., Thickness-dependent bulk properties and weak antilocalization effect in topological insulator $Bi_2Se_3$. *Physical Review B*, **84**(7), 073109, 2011.

47. Arthur, J.R., Technique for growth of epitaxial compound semiconductor films. *US Patent 3,615,931*. 1971.

48. Woodford, C., *Molecular beam epitaxy - Explain that Stuff*. 2018.

49. Wikipedia, *Molecular beam epitaxy*. n.d.

50. Anderson, R.S. and Anderson, S.P., *Geomorphology: The Mechanics and Chemistry of Landscapes*. Cambridge University Press. 2010.

51. Sauerbrey, G.Z., The use of quartz crystals for measuring thin layers and for micro-weighing. *Phys*, **155**, 206–222, 1959.

52. Nizzoli, F., Rieder, K.-H. and Willis, R.F., *Dynamical Phenomena at Surfaces, Interfaces and Superlattices : Proceedings of an International Summer School at the Ettore Majorana Centre, Erice, Italy, July 1-13, 1984*. Springer Berlin Heidelberg. 1985.

53. Ichimiya, A. and Cohen, P.I., *Reflection High-Energy Electron Diffraction*. Cambridge: Cambridge University Press. 2004.

54. Klein, J., *Epitaktische Heterostrukturen aus dotierten Manganaten*. *Universität zu Köln*. 2001.

55. Bansal, N., Kim, Y.S., Edrey, E., Brahlek, M., Horibe, Y., Iida, K., Tanimura, M., Li, G.H., Feng, T., Lee, H.D., Gustafsson, T., Andrei, E. and Oh, S., Epitaxial growth of topological insulator $Bi_2Se_3$ film on Si(111) with atomically sharp interface. *Thin Solid Films*, **520**(1), 224–229, 2011.

56. West, D., Sun, Y.Y., Wang, H., Bang, J. and Zhang, S.B., Native defects in second-generation topological insulators: Effect of spin-orbit interaction on $Bi_2Se_3$. *Physical Review B*, **86**(12), 121201(R), 2012.

57. Tarakina, N. V., Schreyeck, S., Luysberg, M., Grauer, S., Schumacher, C., Karczewski, G., Brunner, K., Gould, C., Buhmann, H., Dunin-Borkowski, R.E. and Molenkamp, L.W., Suppressing Twin Formation in $Bi_2Se_3$ Thin Films. *Advanced Materials Interfaces*, **1**(5), 1400134, 2014.

58. Kampmeier, J., Borisova, S., Plucinski, L., Luysberg, M., Mussler, G. and Grützmacher, D., Suppressing twin domains in molecular beam epitaxy grown $Bi_2Te_3$ topological insulator thin films. *Crystal Growth and Design*, **15**(1), 390–394, 2015.

59. Richardella, A., Zhang, D.M., Lee, J.S., Koser, A., Rench, D.W., Yeats, A.L., Buckley, B.B., Awschalom, D.D. and Samarth, N., Coherent heteroepitaxy of $Bi_2Se_3$ on GaAs (111)B. *Applied Physics Letters*, **97**(2), 262104, 2010.

60. Schreyeck, S., Tarakina, N. V., Karczewski, G., Schumacher, C., Borzenko, T., Brüne, C., Buhmann, H., Gould, C., Brunner, K. and Molenkamp, L.W., Molecular beam epitaxy of

high structural quality $Bi_2Se_3$ on lattice matched InP(111) substrates. *Applied Physics Letters*, **102**(4), 041914, 2013.

61. Seixas, L., Abdalla, L.B., Schmidt, T.M., Fazzio, A. and Miwa, R.H., Topological states ruled by stacking faults in $Bi_2Se_3$ and $Bi_2Te_3$. *Journal of Applied Physics*, **113**(2), 023705, 2013.

62. Wang, Z.Y., Li, H.D., Guo, X., Ho, W.K. and Xie, M.H., Growth characteristics of topological insulator $Bi_2Se_3$ films on different substrates. *Journal of Crystal Growth*, **334**(1), 96–102, 2011.

63. Tarakina, N. V, Schreyeck, S., Borzenko, T., Schumacher, C., Karczewski, G., Brunner, K., Gould, C., Buhmann, H. and Molenkamp, L.W., Comparative Study of the Microstructure of $Bi_2Se_3$ Thin Films Grown on Si(111) and InP(111) Substrates. 2012.

64. Borisova, S., Krumrain, J., Luysberg, M., Mussler, G. and Gr , D., Mode of Growth of Ultrathin Topological Insulator $Bi_2Te_3$ Films on Si (111) Substrates. **12**, 6103, 2012.

65. Guo, X., Xu, Z.J., Liu, H.C., Zhao, B., Dai, X.Q., He, H.T., Wang, J.N., Liu, H.J., Ho, W.K. and Xie, M.H., Single domain $Bi_2Se_3$ films grown on InP(111)A by molecular-beam epitaxy. *Applied Physics Letters*, **102**(15), 151604, 2013.

66. Haazen, P.P.J., Laloë, J.-B., Nummy, T.J., Swagten, H.J.M., Jarillo-Herrero, P., Heiman, D. and Moodera, J.S., Ferromagnetism in thin-film Cr-doped topological insulator $Bi_2Se_3$. *Applied Physics Letters*, **100**(8), 82404, 2012.

67. Rathi, S.J., Smith, D.J. and Drucker, J., Optimization of $In_2Se_3$/Si(111) heteroepitaxy to enable $Bi_2Se_3$/$In_2Se_3$ bilayer growth. *Crystal Growth and Design*, **14**(9), 4617–4623, 2014.

68. Koirala, N., Brahlek, M., Salehi, M., Wu, L., Dai, J., Waugh, J., Nummy, T., Han, M.G., Moon, J., Zhu, Y., Dessau, D., Wu, W., Armitage, N.P. and Oh, S., Record Surface State Mobility and Quantum Hall Effect in Topological Insulator Thin Films via Interface Engineering. *Nano Letters*, **15**(12), 8245–8249, 2015.

69. Raider, S.I., Flitsch, R. and Palmer, M.J., Oxide Growth on Etched Silicon in Air at Room Temperature. *Journal of The Electrochemical Society*, **122**(3), 413, 1975.

70. Binnig, G., Rohrer, H., Gerber, C. and Weibel, E., 7 × 7 Reconstruction on Si(111) Resolved in Real Space. *Physical Review Letters*, **50**(2), 120–123, 1983.

71. Ishizaka, A. and Shiraki, Y., Low Temperature Surface Cleaning of Silicon and Its Application to Silicon MBE. *Journal of The Electrochemical Society*, **133**(4), 666, 1986.

72. Song, C.-L., Wang, Y.-L., Jiang, Y.-P., Zhang, Y., Chang, C.-Z., Wang, L., He, K., Chen, X., Jia, J.-F., Wang, Y., Fang, Z., Dai, X., Xie, X.-C., Qi, X.-L., Zhang, S.-C., Xue, Q.-K. and Ma, X., Topological insulator $Bi_2Se_3$ thin films grown on double-layer graphene by molecular beam epitaxy. *Applied Physics Letters*, **97**(14), 143118, 2010.

73. Li, H.D., Wang, Z.Y., Kan, X., Guo, X., He, H.T., Wang, Z., Wang, J.N., Wong, T.L., Wang, N. and Xie, M.H., The van der Waals epitaxy of $Bi_2Se_3$ on the vicinal Si(111) surface: an approach for preparing high-quality thin films of a topological insulator. *New Journal of*

*Physics*, **12**(10), 103038, 2010.

74. Zhang, G., Qin, H., Teng, J., Guo, J., Guo, Q., Dai, X., Fang, Z. and Wu, K., Quintuple-layer epitaxy of thin films of topological insulator $Bi_2Se_3$. *Applied Physics Letters*, **95**(5), 053114, 2009.

75. Hirahara, T., Sakamoto, Y., Takeichi, Y., Miyazaki, H., Kimura, S., Matsuda, I., Kakizaki, A. and Hasegawa, S., Anomalous transport in an n-type topological insulator ultrathin $Bi_2Se_3$ film. *Physical Review B*, **82**(15), 155309, 2010.

76. Sakamoto, Y., Hirahara, T., Miyazaki, H., Kimura, S. and Hasegawa, S., Spectroscopic evidence of a topological quantum phase transition in ultrathin $Bi_2Se_3$ films. *Physical Review B*, **81**(16), 165432, 2010.

77. Koma, A., Van der Waals epitaxy—a new epitaxial growth method for a highly lattice-mismatched system. *Thin Solid Films*, **216**(1), 72–76, 1992.

78. Bansal, N., Kim, Y.S., Brahlek, M., Edrey, E. and Oh, S., Thickness-independent transport channels in topological insulator $Bi_2Se_3$ thin films. *Physical Review Letters*, **109**(11), 116804, 2012.

79. Wu, L., Salehi, M., Koirala, N., Moon, J., Oh, S. and Armitage, N.P., Quantized Faraday and Kerr rotation and axion electrodynamics of a 3D topological insulator. *Science*, **354**(6316), 1124–1127, 2016.

80. Salehi, M., Shapourian, H., Koirala, N., Brahlek, M.J., Moon, J. and Oh, S., Finite-Size and Composition-Driven Topological Phase Transition in $(Bi_{1-x}In_x)_2Se_3$ Thin Films. *Nano Letters*, **16**(9), 5528–5532, 2016.

81. Moon, J., Koirala, N., Salehi, M., Zhang, W., Wu, W. and Oh, S., Solution to the Hole-Doping Problem and Tunable Quantum Hall Effect in $Bi_2Se_3$ Thin Films. *Nano Letters*, **18**(2), 820–826, 2018.

82. Hall, E.H., On a New Action of the Magnet on Electric Currents. *American Journal of Mathematics*, **2**(3), 287, 1879.

83. Van der Pauw, L.J., A Method of Measuring Specific Resistivity and Hall Effect of Discs of Arbitrary Shape. *Philips Research Reports*, **13**(1), 1–9, 1958a.

84. Van der Pauw, L.J., A Method of Measuring the Resistivity and Hall Coefficient on Lamellae of Arbitrary Shape. *Philips Technical Review*, **20**(8), 220–224, 1958b.

85. Bartynski, R.A., *Surface science lecture note*. 2013.

86. Brahlek, M.J., Atomic scale engineering of topological materials. 2014.

87. Wikipedia, *Angle-resolved photoemission spectroscopy - Wikipedia*. n.d.

88. Mann, C., West, D., Miotkowski, I., Chen, Y.P., Zhang, S. and Shih, C.-K., Mapping the 3D surface potential in $Bi_2Se_3$. *Nature communications*, **4**, 2277, 2013.

89. Ando, Y., Topological insulator materials. *Journal of the Physical Society of Japan*, **82**(10),

102001, 2013.

90. Brahlek, M., Koirala, N., Salehi, M., Bansal, N. and Oh, S., Emergence of decoupled surface transport channels in bulk insulating $Bi_2Se_3$ thin films. *Physical Review Letters*, **113**(2), 26801, 2014.

91. Brahlek, M.J., Koirala, N., Liu, J., Yusufaly, T.I., Salehi, M., Han, M.G., Zhu, Y., Vanderbilt, D. and Oh, S., Tunable inverse topological heterostructure utilizing $(Bi_{1-x}In_x)_2Se_3$ and multichannel weak-antilocalization effect. *Physical Review B*, **93**(12), 125416, 2016.

92. He, L., Kou, X. and Wang, K.L., Review of 3D topological insulator thin-film growth by molecular beam epitaxy and potential applications. *Physica Status Solidi - Rapid Research Letters*, **7**(1–2), 50–63, 2013.

93. Sharma, P.A., Lima Sharma, A.L., Hekmaty, M., Hattar, K., Stavila, V., Goeke, R., Erickson, K., Medlin, D.L., Brahlek, M., Koirala, N. and Oh, S., Ion beam modification of topological insulator bismuth selenide. *Applied Physics Letters*, **105**(24), 242106, 2014.

94. Bansal, N., Cho, M.R., Brahlek, M., Koirala, N., Horibe, Y., Chen, J., Wu, W., Park, Y.D. and Oh, S., Transferring MBE-grown topological insulator films to arbitrary substrates and metal-insulator transition via dirac gap. *Nano Letters*, **14**(3), 1343–1348, 2014.

95. Brahlek, M., Kim, Y.S., Bansal, N., Edrey, E. and Oh, S., Surface versus bulk state in topological insulator $Bi_2Se_3$ under environmental disorder. *Applied Physics Letters*, **99**(1), 012109, 2011.

96. Dai, J., West, D., Wang, X., Wang, Y., Kwok, D., Cheong, S.W., Zhang, S.B. and Wu, W., Toward the Intrinsic Limit of the Topological Insulator $Bi_2Se_3$. *Physical Review Letters*, **117**(10), 106401, 2016.

97. Xue, L., Zhou, P., Zhang, C.X., He, C.Y., Hao, G.L., Sun, L.Z. and Zhong, J.X., First-principles study of native point defects in $Bi_2Se_3$. *AIP ADVANCES*, **3**, 052105, 2013.

98. Tumelero, M.A., Faccio, R. and Pasa, A.A., The role of interstitial native defects in the topological insulator $Bi_2Se_3$. *Journal of Physics: Condensed Matter*, **28**(42), 425801, 2016.

99. Urazhdin, S., Bilc, D., Tessmer, S.H., Mahanti, S.D., Kyratsi, T. and Kanatzidis, M.G., Scanning tunneling microscopy of defect states in the semiconductor $Bi_2Se_3$. *Physical Review B*, **66**(16), 161306, 2002.

100. Alpichshev, Z., Biswas, R.R., Balatsky, A. V., Analytis, J.G., Chu, J.H., Fisher, I.R. and Kapitulnik, A., STM imaging of impurity resonances on $Bi_2Se_3$. *Physical Review Letters*, **108**(20), 206402, 2012.

101. Huang, F.T., Chu, M.W., Kung, H.H., Lee, W.L., Sankar, R., Liou, S.C., Wu, K.K., Kuo, Y.K. and Chou, F.C., Nonstoichiometric doping and Bi antisite defect in single crystal Bi 2Se 3. *Physical Review B - Condensed Matter and Materials Physics*, **86**(8), 081104, 2012.

102. Hor , J., Starý, Z., ' , P. and Pancír, J., Anti-site defects in n-$Bi_2Se_3$ crystals. *Journal of Physics and Chemistry of Solids*, **51**(12), 1353–1360, 1990.

103. Li, H., Song, Y.R., Yao, M.Y., Zhu, F., Liu, C. and Al, E., Carrier density dependence of the magnetic properties in iron-doped $Bi_2Se_3$ topological insulator. *Journal of Applied Physics*, **113**, 043926, 2013.

104. Wang, Z., Lin, T., Wei, P., Liu, X., Dumas, R., Liu, K. and Shi, J., Tuning carrier type and density in $Bi_2Se_3$ by Ca-doping. *Applied Physics Letters*, **97**(4), 042112, 2010.

105. Eguchi, G., Kuroda, K., Shirai, K., Kimura, A. and Shiraishi, M., Surface Shubnikov-de Haas oscillations and nonzero Berry phases of the topological hole conduction in $Tl_{1-x}Bi_{1+x}Se_2$. *Physical Review B*, **90**(20), 201307, 2014.

106. Choi, Y.H., Jo, N.H., Lee, K.J., Lee, H.W., Jo, Y.H., Kajino, J., Takabatake, T., Ko, K.T., Park, J.H. and Jung, M.H., Simple tuning of carrier type in topological insulator $Bi_2Se_3$ by Mn doping. *Applied Physics Letters*, **101**(15), 152103, 2012.

107. Ka parov , J., Dra ar, C., Krej ov , A., Bene , L., Lo t' k, P., Chen, W., Zhou, Z. and Uher, C., n-type to p-type crossover in quaternary $Bi_xSb_yPb_zSe_3$ single crystals. *Journal of Applied Physics*, **97**(10), 103720, 2005.

108. Liu, H., Liu, S., Yi, Y., He, H. and Wang, J., Shubnikov–de Haas oscillations in n and p type $Bi_2Se_3$ flakes. *2D Materials*, **2**(4), 045002, 2015.

109. Xue, L., Sun, L., Hao, G., Zhou, P., He, C., Huang, Z. and Zhong, J., Effective Fermi level tuning of $Bi_2Se_3$ by introducing CdBi/CaBi dopant. *RSC Advances*, **4**(21), 10499–10504, 2014.

110. Checkelsky, J.G., Hor, Y.S., Cava, R.J. and Ong, N.P., Bulk band gap and surface state conduction observed in voltage-tuned crystals of the topological insulator $Bi_2Se_3$. *Physical Review Letters*, **106**(19), 196801, 2011.

111. Nakamura, S., Background story of the invention of efficient blue InGaN light emitting diodes (Nobel Lecture). *Annalen der Physik*, **527**(5–6), 335–349, 2015.

112. Salehi, M., Brahlek, M., Koirala, N., Moon, J., Wu, L., Armitage, N.P. and Oh, S., Stability of low-carrier-density topological-insulator $Bi_2Se_3$ thin films and effect of capping layers. *APL Materials*, **3**(9), 091101, 2015.

113. Henini, M., *Molecular beam epitaxy : from research to mass production*. Elsevier. 2012.

114. Brahlek, M., Koirala, N., Salehi, M., Moon, J., Zhang, W., Li, H., Zhou, X., Han, M.G., Wu, L., Emge, T., Lee, H.D., Xu, C., Rhee, S.J., Gustafsson, T., Armitage, N.P., Zhu, Y., Dessau, D.S., Wu, W. and Oh, S., Disorder-driven topological phase transition in $Bi_2Se_3$ films. *Physical Review B*, **94**(16), 165104, 2016.

115. Shannon, R.D., Revised effective ionic radii and systematic studies of interatomic distances in halides and chalcogenides. *Acta Crystallographica Section A*, **32**(5), 751–767, 1976.

116. Yoshimi, R., Tsukazaki, A., Kozuka, Y., Falson, J., Takahashi, K.S., Checkelsky, J.G., Nagaosa, N., Kawasaki, M. and Tokura, Y., Quantum Hall effect on top and bottom surface states of topological insulator $(Bi_{1-x}Sb_x)_2Te_3$ films. *Nature Communications*, **6**, 6627, 2015.

117. Xu, Y., Miotkowski, I. and Chen, Y.P., Quantum transport of two-species Dirac fermions in dual-gated three-dimensional topological insulators. *Nature Communications*, **7**(May), 11434, 2016.

118. Vafek, O., Quantum Hall effect in a singly and doubly connected three-dimensional topological insulator. *Physical Review B*, **84**(24), 245417, 2011.

119. Beidenkopf, H., Roushan, P., Seo, J., Gorman, L., Drozdov, I., Hor, Y.S., Cava, R.J. and Yazdani, A., Spatial fluctuations of helical Dirac fermions on the surface of topological insulators. *Nature Physics*, **7**(12), 939–943, 2011.

120. Cheng, P., Song, C., Zhang, T., Zhang, Y., Wang, Y., Jia, J.F., Wang, J., Wang, Y., Zhu, B.F., Chen, X., Ma, X., He, K., Wang, L., Dai, X., Fang, Z., Xie, X., Qi, X.L., Liu, C.X., Zhang, S.C. and Xue, Q.K., Landau quantization of topological surface states in $Bi_2Se_3$. *Physical Review Letters*, **105**(7), 076801, 2010.

121. Nagaosa, N., Sinova, J., Onoda, S., MacDonald, A.H. and Ong, N.P., Anomalous Hall effect. *Reviews of Modern Physics*, **82**(2), 1539–1592, 2010.

122. Yu, R., Zhang, W., Zhang, H.-J., Zhang, S.-C., Dai, X. and Fang, Z., Quantized Anomalous Hall Effect in Magnetic Topological Insulators. *Science*, **329**(5987), 61–64, 2010.

123. Hsieh, D., Xia, Y., Wray, L., Qian, D., Pal, A., Dil, J.H., Osterwalder, J., Meier, F., Bihlmayer, G., Kane, C.L., Hor, Y.S., Cava, R.J. and Hasan, M.Z., Observation of unconventional quantum spin textures in topological insulators. *Science (New York, N.Y.)*, **323**(5916), 919–22, 2009.

124. Chang, C.Z., Zhang, J.S., Feng, X., Shen, J., Zhang, Z.C., Guo, M.H., Li, K., Ou, Y.B., Wei, P., Wang, L.L., Ji, Z.Q., Feng, Y., Ji, S.H., Chen, X., Jia, J.F., Dai, X., Fang, Z., Zhang, S.C., He, K., Wang, Y.Y., Lu, L., Ma, X.C. and Xue, Q.K., Experimental Observation of the Quantum Anomalous Hall Effect in a Magnetic Topological Insulator. *Science*, **340**(6129), 167–170, 2013.

125. Chang, C.-Z., Zhao, W., Kim, D.Y., Zhang, H., Assaf, B.A., Heiman, D., Zhang, S.-C., Liu, C., Chan, M.H.W. and Moodera, J.S., High-precision realization of robust quantum anomalous Hall state in a hard ferromagnetic topological insulator. *Nature Materials*, **14**(5), 473–477, 2015.

126. Mogi, M., Yoshimi, R., Tsukazaki, A., Yasuda, K., Kozuka, Y., Takahashi, K.S., Kawasaki, M. and Tokura, Y., Magnetic modulation doping in topological insulators toward higher-temperature quantum anomalous Hall effect. *Applied Physics Letters*, **107**(18), 182401, 2015.

127. Feng, X., Feng, Y., Wang, J., Ou, Y., Hao, Z., Liu, C., Zhang, Z., Zhang, L., Lin, C., Liao, J., Li, Y., Wang, L.L., Ji, S.H., Chen, X., Ma, X., Zhang, S.C., Wang, Y., He, K. and Xue, Q.K., Thickness Dependence of the Quantum Anomalous Hall Effect in Magnetic Topological Insulator Films. *Advanced Materials*, **28**, 6386–6390, 2016.

128. Ou, Y., Liu, C., Jiang, G., Feng, Y., Zhao, D., Wu, W., Wang, X.-X., Li, W., Song, C., Wang, L.-L., Wang, W., Wu, W., Zhang, Q., Gu, L., Wang, Y., He, K., Ma, X.-C. and Xue, Q.-K., Enhancing the quantum anomalous Hall effect by magnetic codoping in a topological

insulator. *Adv Mater*, **2017**, 1703062, 2017.

129. He, K., Wang, Y. and Xue, Q.K., Quantum anomalous Hall effect. *National Science Review*, **1**(1), 38–48, 2014.

130. Zhang, J., Chang, C.-Z., Tang, P., Zhang, Z., Feng, X., Li, K., Wang, L. -l., Chen, X., Liu, C., Duan, W., He, K., Xue, Q.-K., Ma, X. and Wang, Y., Topology-Driven Magnetic Quantum Phase Transition in Topological Insulators. *Science*, **339**(6127), 1582–1586, 2013.

131. Zhang, L., Zhao, D., Zang, Y., Yuan, Y., Jiang, G., Liao, M., Zhang, D., He, K., Ma, X. and Xue, Q., Ferromagnetism in vanadium-doped $Bi_2Se_3$ topological insulator films. *APL Materials*, **5**(7), 076106, 2017.

132. Kim, J., Jhi, S.-H., MacDonald, A.H. and Wu, R., Ordering mechanism and quantum anomalous Hall effect of magnetically doped topological insulators. *Physical Review B*, **96**(14), 140410, 2017.

133. Chang, C.Z., Tang, P., Wang, Y.L., Feng, X., Li, K., Zhang, Z., Wang, Y., Wang, L.L., Chen, X., Liu, C., Duan, W., He, K., Ma, X.C. and Xue, Q.K., Chemical-potential-dependent gap opening at the dirac surface states of $Bi_2Se_3$ induced by aggregated substitutional Cr atoms. *Physical Review Letters*, **112**(5), 056801, 2014.

134. Moon, J., Kim, J., Koirala, N., Salehi, M., Vanderbilt, D. and Oh, S., Ferromagnetism in Cr-doped $Bi_2Se_3$ thin films via surface-state engineering. *Nano Letters*, (under review), 2019.

135. Van Vleck, J.H., Models of exchange coupling in ferromagnetic media. *Reviews of Modern Physics*, **25**(1), 220–227, 1953.

136. Ruderman, M.A. and Kittel, C., Indirect Exchange Coupling of Nuclear Magnetic Moments by Conduction Electrons. *Phys. Rev.*, **96**(1), 99–102, 1954.

137. Liu, Q., Liu, C.X., Xu, C., Qi, X.L. and Zhang, S.C., Magnetic impurities on the surface of a topological insulator. *Physical Review Letters*, **102**(15), 156603, 2009.

138. Chang, C.-Z., Zhang, J., Liu, M., Zhang, Z., Feng, X., Li, K., Wang, L.-L., Chen, X., Dai, X., Fang, Z., Qi, X.-L., Zhang, S.-C., Wang, Y., He, K., Ma, X.-C. and Xue, Q.-K., Thin Films of Magnetically Doped Topological Insulator with Carrier-Independent Long-Range Ferromagnetic Order. *Advanced Materials*, **25**(7), 1065–1070, 2013.

139. Li, M., Chang, C.Z., Wu, L., Tao, J., Zhao, W., Chan, M.H.W., Moodera, J.S., Li, J. and Zhu, Y., Experimental verification of the van Vleck nature of long-range ferromagnetic order in the vanadium-doped three-dimensional topological insulator $Sb_2Te_3$. *Physical Review Letters*, **114**(14), 146802, 2015.

140. Kou, X., Lang, M., Fan, Y., Jiang, Y., Nie, T., Zhang, J., Jiang, W., Wang, Y., Yao, Y., He, L. and Wang, K.L., Interplay between Different Magnetisms in Cr-Doped Topological Insulators. *ACS Nano*, **7**(10), 9205–9212, 2013.

141. Wang, W., Ou, Y., Liu, C., Wang, Y., He, K., Xue, Q.-K. and Wu, W., Direct evidence of ferromagnetism in a quantum anomalous Hall system. *Nature Physics*, **14**(8), 791–795,

2018.

142. Kresse, G. and Furthmüller, J., Efficient iterative schemes for ab initio total-energy calculations using a plane-wave basis set. *Physical Review B*, **54**(16), 11169–11186, 1996a.

143. Kresse, G. and Furthmüller, J., Efficiency of ab-initio total energy calculations for metals and semiconductors using a plane-wave basis set. *Computational Materials Science*, **6**(1), 15–50, 1996b.

144. Mostofi, A.A., Yates, J.R., Pizzi, G., Lee, Y.-S., Souza, I., Vanderbilt, D. and Marzari, N., An updated version of wannier90: A tool for obtaining maximally-localised Wannier functions. *Computer Physics Communications*, **185**(8), 2309–2310, 2014.

145. Blöchl, P.E., Projector augmented-wave method. *Physical Review B*, **50**(24), 17953–17979, 1994.

146. Kresse, G. and Joubert, D., From ultrasoft pseudopotentials to the projector augmented-wave method. *Physical Review B*, **59**(3), 1758–1775, 1999.

147. Perdew, J.P., Ruzsinszky, A., Csonka, G.I., Vydrov, O.A., Scuseria, G.E., Constantin, L.A., Zhou, X. and Burke, K., Restoring the Density-Gradient Expansion for Exchange in Solids and Surfaces. *Physical Review Letters*, **100**(13), 136406, 2008.

148. Ghasemi, A., Kepaptsoglou, D., Collins-McIntyre, L.J., Ramasse, Q., Hesjedal, T. and Lazarov, V.K., Atomic-level structural and chemical analysis of Cr-doped $Bi_2Se_3$ thin films. *Scientific Reports*, **6**(1), 26549, 2016.

149. Hart, S., Ren, H., Kosowsky, M., Ben-Shach, G., Leubner, P., Brüne, C., Buhmann, H., Molenkamp, L.W., Halperin, B.I. and Yacoby, A., Controlled finite momentum pairing and spatially varying order parameter in proximitized HgTe quantum wells. *Nature Physics*, **13**(1), 87–93, 2016.

150. Ren, H., Pientka, F., Hart, S., Pierce, A., Kosowsky, M., Lunczer, L., Schlereth, R., Scharf, B., Hankiewicz, E.M., Molenkamp, L.W., Halperin, B.I. and Yacoby, A., Topological Superconductivity in a Phase-Controlled Josephson Junction. arXiv:1809.03076, 2018.